Bioimpedance spectroscopy of breast cancer cells: A microsystems approach

Vaishnavi Srinivasaraghavan

Dissertation submitted to the faculty of the Virginia Polytechnic Institute and State University in partial fulfillment of the requirements for the degree of

Doctor of Philosophy
In
Electrical Engineering

Masoud Agah, Chair
Jeannine S. Strobl
Luke F. Lester
Yizheng Zhu
Deborah F. Kelly

September 18th, 2015
Blacksburg, VA

Keywords: Microelectromechanical systems (MEMS), Bioimpedance, Microelectrode Arrays (MEA), Electrical Cell-substrate Impedance Sensing (ECIS), Breast Cancer, Triple Negative Breast Cancer (TNBC), Nano-coatings, Single cell analysis, Microfluidics, Cell deformability.

Bioimpedance spectroscopy of breast cancer cells: A microsystems approach

Vaishnavi Srinivasaraghavan

ABSTRACT

Bioimpedance presents a versatile, label-free means of monitoring biological cells and their responses to physical, chemical and biological stimuli. Breast cancer is the second most common type of cancer among women in the United States. Although significant progress has been made in diagnosis and treatment of this disease, there is a need for robust, easy-to-use technologies that can be used for the identification and discrimination of critical subtypes of breast cancer in biopsies obtained from patients. This dissertation makes contributions in three major areas towards addressing the goal. First, we developed miniaturized bioimpedance sensors using MEMS and microfluidics technology that have the requisite traits for clinical use including reliability, ease-of-use, low-cost and disposability. Here, we designed and fabricated two types of bioimpedance sensors. One was based on electric cell-substrate impedance sensing (ECIS) to monitor cell adhesion based events and the other was a microfluidic device with integrated microelectrodes to examine the biophysical properties of single cells. Second, we examined a panel of triple negative breast cancer (TNBC) cell lines and a hormone therapy resistant model of breast cancer in order to improve our understanding of the bioimpedance spectra of breast cancer subtypes. Third, we explored strategies to improve the sensitivity of the microelectrodes to bioimpedance measurements from breast cancer cells. We investigated nano-scale coatings on the surface of the electrode and geometrical variations in a branched electrode design to accomplish this. This work demonstrates the promise of bioimpedance technologies in monitoring diseased cells and their responses to pharmaceutical agents, and motivates further research in customization of this technique for use in personalized medicine.

To everyone I have learnt from...

Acknowledgements

This PhD dissertation is the culmination of over 4 years of research and would not have been possible without the support and involvement of several people within the Virginia Tech community and my family. I am immensely thankful for the experience, knowledge and skills I have gained here and will use them throughout my life and career.

First and foremost, I am extremely grateful to Prof. Masoud Agah, the director of VT MEMS and my advisor, for giving me the opportunity to work on this challenging project in an upcoming field. He has motivated me to find creative solutions to problems and push myself to be the best researcher I can be. I am also highly indebted to Dr. Jeannine Strobl for her guidance and involvement throughout my PhD. I have learnt a lot through our discussions. I would also like to thank Prof. Luke Lester, Dr. Yizheng Zhu and Dr. Deb Kelly for agreeing to be on my committee and offering their valuable suggestions.

The current and past students of VT MEMS, especially Dr. Yahya Hosseini, Mr. Hesam Babahosseini, Ms. Sepeedah Soltanian-Zadeh, Ms. Diana Nakidde, Ms. Huaning Zhao, Dr. Phillip Zellner, Dr. Shree Narayanan, Dr. Muhammad Akbar and Dr. Hamza Shakeel, have been a great source of support in my research and made the lab an interesting workplace. I would also like to give a special mention to Dr. Dong Wang and Mrs. Virginia Riquelme for our successful collaborations.

I would like to express my gratitude for the technical guidance provided by Mr. Don Leber (Manager, Micron clean room, ECE Department), Dr. Kristi Decourcy (Lab Manager, Confocal microscope, Fralin Life Sciences), Ms. Kathy Lowe (Morphology Lab Supervisor, Virginia-Maryland College of Veterinary Medicine) and Mr. Stephen McCartney (ICTAS Nanoscale Characterization and Fabrication Lab). I am also thankful to Mr. Matt Banat and Mr. Joe Rose from Circuit Check Inc. and Mr. James Wei from Zurich Instruments for their technical support.

I am deeply grateful to my husband, Vighnesh Umapathy, for his incredible patience and for being my friend, confidant, motivator and all the other roles he has played. Without him, this dissertation would not have been possible. I am also lucky to have friends like

Kalyani Tipnis, Mrudula Karve, Nita Chandrasekhar, Rini Rajan, Swati Sudhaakar and Deepti Aggarwal who were my family in the United States and made being away from home easier.

I would like to acknowledge my father, P. Srinivasaraghavan, who has always been and will continue to be my role model and a source of motivation throughout my life and my mother Usha for her unconditional love and support for everything I do. My sister Varshini also warrants a mention for pushing me to be a person that she would look up to.

Finally, I would like to thank God for all the blessings he has showered on me and for where I am today.

Vaishnavi Srinivasaraghavan

September 2015

Table of Contents

List of Figures

List of Tables

1. Introduction

1.1. Bioimpedance

Bioimpedance refers to the opposition offered by biological samples to the flow of electric current. The biological sample in question could be sub-cellular components such as deoxyribonucleic acid (DNA), mammalian cells, bodily fluids such as blood plasma, tissue sections or the entire body. Bioimpedance is measured using either two, three or four electrode configurations. In a four electrode configuration, one pair of electrodes is used to excite the sample via an applied electric current and the other pair is used to measure the resulting potential drop. In a two electrode configuration, the same electrode pair is used to excite the sample with an electric current and measure the corresponding voltage drop or vice versa. An electrochemical reaction occurs that facilitates the transfer of electrons (charge) from the conducting metal electrode to the ions present in the biological sample [1]. The bioimpedance of the sample is calculated as the ratio of the voltage to the current as measured from the electrodes. It is characteristically measured by excitation with an alternating current (AC) source and hence, is a function of frequency. Often, the impedance response of the sample is examined over the range of frequencies. This technique is referred to as bioimpedance spectroscopy.

1.2. The Cell Structure

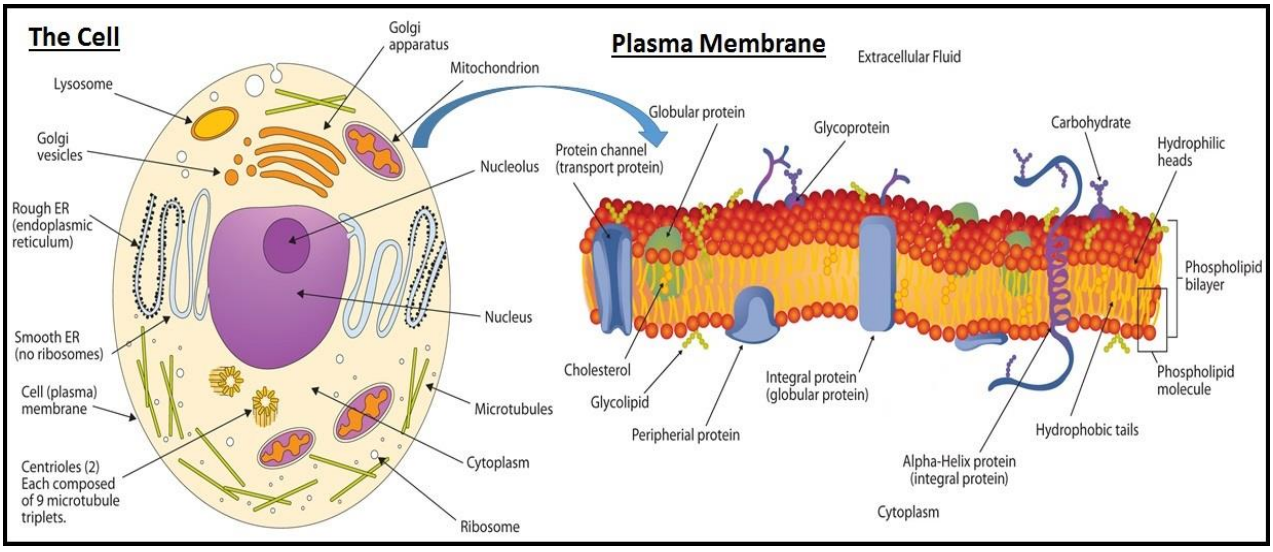

Figure 1.1 The structure of the animal cell and the plasma membrane. Images adapted from [2] under the Creative Commons by-nc-sa 3.0 license.

The cell is the fundamental structural and functional building block of the human body. It consists of the nucleus and other organelles such as the mitochondria, ribosomes, endoplasmic reticulum, lysosomes and golgi apparatus as seen in **Figure 1.1**. Each organelle performs a specific function that is essential to the proper health and functioning of the cell. The cytosol is a highly viscous water abundant fluid with dissolved macromolecules and enzymes. It is electrically highly conductive due to the presence of charged ions such as sodium (Na^+), potassium (K^+), calcium (Ca^{2+}) and chloride (Cl^-) [3]. The cytoskeleton of the cell is made up of three kinds of protein filaments, namely actin, intermediate filaments and microtubules which give the cell its shape, mechanical stiffness and motor function. Microtubules form an extensive network throughout the cell and play an active role in positioning and anchoring the organelles within the cell. The microtubule motor proteins, kinesin and dynein, enable transport of organelles and other cellular material within the cell to locations where they are needed.

The cell is surrounded by the plasma membrane which is made up of a phospholipid bilayer that maintains the integrity of the cell structure [3]. It is a good electrical insulator and embedded with various protein structures that act as gatekeepers, regulating the transport of material to and from the cell interior as seen in **Figure 1.1**. The extracellular space is also occupied by a conductive fluid abundant in ions. However, the concentration of ions in the cytosol is very different from that of the surrounding fluid. For instance, the concentration of K^+ ions is much higher than Na^+ in the cytosol while the vice versa is true in the extracellular fluid. Ion channels and pumps are responsible for moving ions in and against the direction of the established concentration gradient, respectively. This results in a potential drop (~70 mV) across the plasma membrane where the cytosolic side is more negative than the exoplasmic side [3]. It should be noted that all cells do not have the same membrane potential. Hence, the plasma membrane effectively behaves like an electrical capacitor with the accumulation of negative charges on the inside layer and positive charges on the outside layer. Since, the plasma membrane is only two molecules thick (~3.5nm), it results in very high specific membrane capacitance (~1 $\mu F/cm^2$ or 0.01 F/m^2). Some organelles present inside the cell are also surrounded by a membrane similar to the plasma membrane to increase the efficiency of biochemical reactions by creating a specific internal environment. The nuclear membrane on the other hand is made up of two lipid bilayers and has small pores that enable transport of material to and from the nucleus. Reports show that the nuclear membrane in

eukaryotic cells also maintains a potential across it with the intra-nuclear side more negative than the cytoplasmic side [4].

1.3. Bioimpedance Technologies

There are many attributes that make bioimpedance practical and desirable as a technology for use in medicine and biology such as non-invasiveness, low-cost, portability of measurement systems and ease of use [5]. In this section, we discuss existing commercial and laboratory techniques that employ bioimpedance to accomplish functional goals.

1.3.1. Bioimpedance Analysis (BIA)

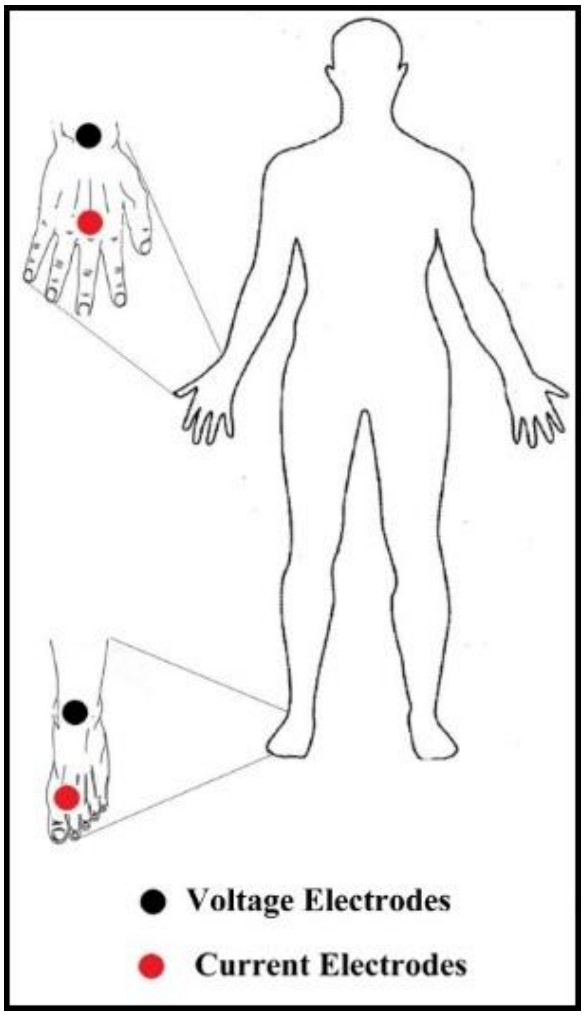

Figure 1.2 Typical position of surface electrodes on body for bioimpedance analysis. Image reproduced from [8] under the Creative Commons Attribution License .

One of the main advantages of using bioimpedance is the non-invasive or minimally invasive nature of the measurements. Bioimpedance analysis (BIA) uses surface electrodes are attached to the wrist and ankle to characterize the composition of the human body (see **Figure 1.2**). This technique was first commercialized in the 1980s and is widely used by nutritional and fitness experts today to determine total body water (TBW) and body fat mass (BFM)) in individuals [6]. BIA relies on impedance measurements made at a single frequency (50 kHz) and uses an empirical formula to determine the total body water with the height and weight of the person taken into consideration [7]. This is based on the fact that the path of the current passing through the body is predominantly through the ions present in the extracellular and intracellular fluids [8]. Since the TBW is roughly 73.2% of fat free mass (FFM) in healthy individuals, the body fat of the individual is calculated as the difference

between the body weight of the individual and his/her FFM. Bioimpedance spectroscopy (BIS) is basically the same technique but uses impedance measurements made at low and high frequencies in the 5 kHz-1 MHz spectrum. Both BIA and BIS have been shown to work well in healthy individuals. However, it should be noted that factors such as electrode position, dehydration, food consumption or exercise immediately prior to testing, body position, and ambient temperature and humidity conditions can affect the accuracy of the TBW calculated from BIA by 10% or more [9, 10]. Hence, although BIA is reproducible, it is more useful as a method to monitor fluctuations in relative body composition over time rather than one time accurate measurements of body composition in individuals.

The complex current paths in whole body BIA make it impossible to make interpretations regarding composition and structure of the tissues and muscle in the body. However, localized BIA overcomes this barrier by using the simplified geometry to develop mathematical models that can correlate the obtained impedance measurements with underlying anatomy. Localized BIA has been used to obtain measurements from the thigh, forearm, breast, prostate etc. and has been demonstrated to have clinical value in disease diagnosis and monitoring [8, 11]. For instance, Rutkove et al. showed that the effective longitudinal resistivity and spatially averaged phase angle obtained from localized BIA measurements on the thigh, were altered in patients suffering from neuromuscular disorders like amyotrophic lateral sclerosis, inflammatory myopathy and inclusion-body myositis [12]. They also reported that a reduction in the phase angle correlated with disease progression while normalization of phase angle was observed during remission [12]. Temporal BIA can also be used to estimate the mass and volume of muscles to monitor impairment during neurological disease development [13]. Zlochiver et al. reported a portable system that uses localized BIA measurements from the chest and a two dimensional thorax model to estimate the resistivity of each lung using an iterative parameter optimization scheme [14]. Such a system enables non-invasive monitoring of lung fluid content in patients having pulmonary edema and makes it readily available at clinics and homes. More generally, the phase angle obtained from BIA measurements can be considered a universal marker of health [11]. A decrease in the phase angle has been shown to correlate with the presence of late stage lung cancer in patients [15].

1.3.2. Electric Cell-substrate Impedance Sensing (ECIS)

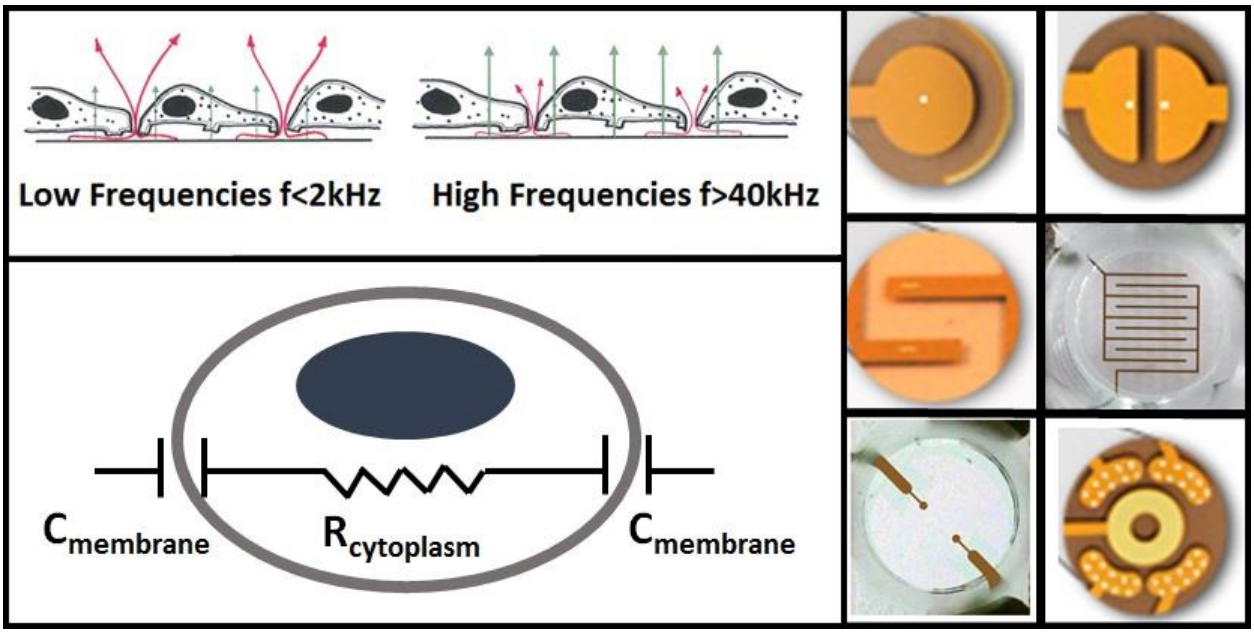

Figure 1.3 The current paths through the cell monolayer at different frequencies (top), a simplified equivalent circuit model of the cell (bottom) and standard electrodes used to make ECIS measurements (right). Some images adapted from the website of Applied Biophysics Inc.

Electrical Cell-Substrate Impedance Sensing (ECIS) is a technique that is used to monitor live biological cells in tissue culture. The term was coined by the inventors of the technique, Ivar Giaever and Charles R. Keese, and is currently the trademark of their company Applied Biophysics which sells a commercial system to make impedance measurements from live cell cultures. The electrical impedance signals are recorded from cells that are adherent on the surface of planar microelectrodes usually made of gold. These electrodes can be on the surface of regular treated polystyrene petri dishes or well plates used for tissue culture or on any other surface suitable for cell culture like glass or silicon with an appropriate chamber to hold media during measurements. The technique can be used to make measurements from any animal cell line that grows as a monolayer by attachment. Researchers have used the technique to study a wide variety of cell lines including fibroblasts, epithelial and endothelial cells. ECIS is based on the ability of cells to block the flow of electric current when attached to a conductive surface. **Figure 1.3** shows the equivalent circuit model for a single cell and the dominant current paths through the cell monolayer in different ranges of the frequency spectrum. The cell membrane is made of a phospholipid double layer which acts like a capacitor and the cytoplasm of the cell is mainly made of a conductive gel-

like substance which can be modeled as a resistor. At lower frequencies, the current passes through the cell-substrate gap and the space between adjacent cells also called the cell-cell junction region. However, at higher frequencies the current can couple through the cell and thus probe the electrical properties of the cell membrane and interior. The ECIS impedance measurements can be made continuously at a single frequency or a sweep across multiple frequency points can be done at regular time intervals.

Standard electrodes used to make ECIS measurements are also shown in **Figure 1.3**. Measurements are always made from a pair of electrodes and they come in different configurations. For instance, the electrode pair can have one very large counter electrode which is ten or more times larger in area than one very small sensing electrode. A number of different shapes including circular, square, rectangular, branch and other shapes have been used for the sensing and counter electrode design in ECIS devices. Another, commonly used configuration is the interdigitated electrode pair in which two identical comb shaped electrodes are inter-locked with each other as shown. In this configuration, both electrodes play the role of sensing and counter electrodes. Commercial systems such as xCELLigence and CellKey employ these electrodes in making impedance measurements from cell monolayers.

The impedance values recorded are directly related to the cell coverage on the electrodes. This makes it suitable for measuring the growth and proliferation of cells in culture. Using the impedance values recorded it is possible to infer the rate of growth, the doubling time and when the culture is confluent. So, one of the applications of ECIS is the remote monitoring of cell growth [16, 17]. To ensure there is good attachment between the cells and the electrodes, the electrodes are typically treated with oxygen plasma in a plasma cleaner followed by coating with extra-cellular matrix proteins like collagen or fibronectin just before the addition of cells. Alternately, cell culture medium can be added to the electrodes and the serum proteins in the medium self-adsorb on to them providing the same effect. However, for long term monitoring it is desirable to pre-coat the electrodes before adding cells to them [16]. **Figure 1.4** shows the characteristic change in the impedance profile as cells attach and grow on microelectrodes. The baseline impedance is the impedance when there are no cells on the electrode. As they grow, the impedance increases as the number of cells on the electrode increases. When the area on the electrodes is completely filled with cells, the impedance saturates to a maximum value indicating they have reached confluence.

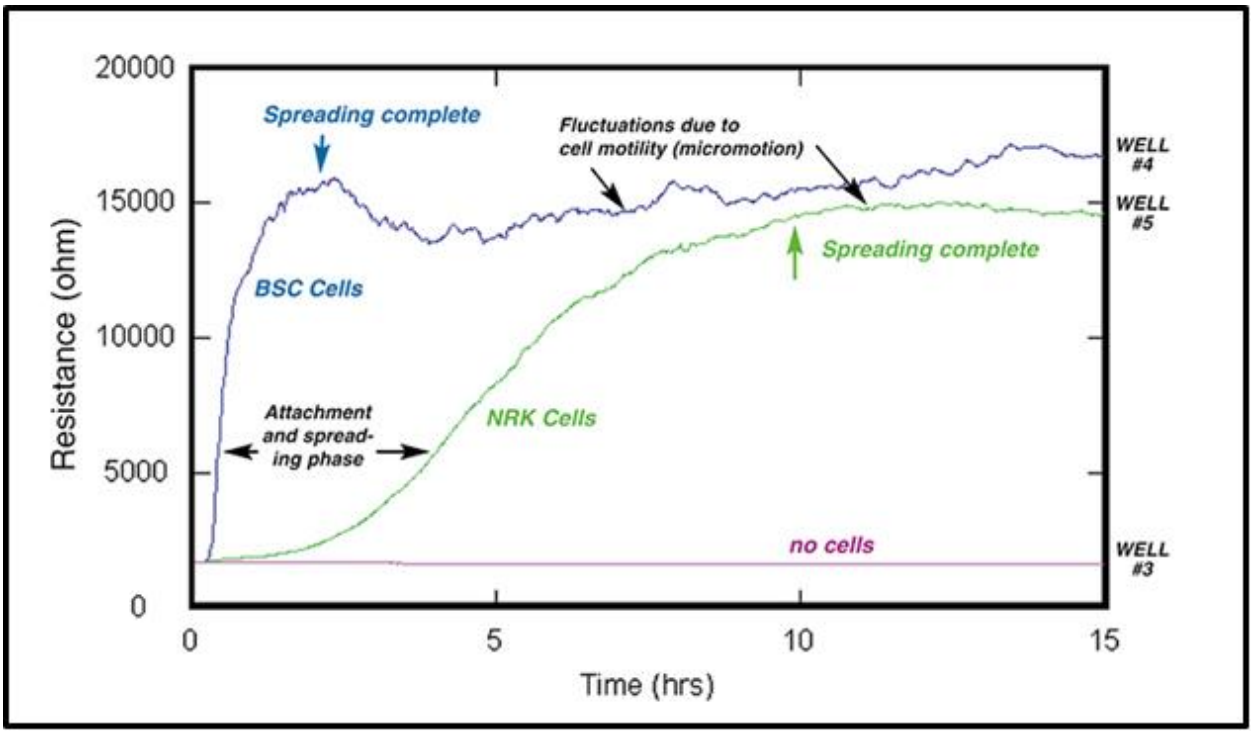

Figure 1.4 Impedance variations recorded as normal epithelial kidney cell lines NRK and BSC-1 attach and grow on microelectrodes. Image adapted from the website of Applied Biophysics Inc.

On the same note, if cells begin to die, they become rounded and their attachment to the electrodes decreases till they completely detach from them. When this happens, it results in a drop in the impedance values measured which in essence is a reversal in the rise seen due to cell attachment. This mechanism of detection is the basis for the use of ECIS to monitor events like apoptosis and can also be used to measure the cytotoxicity of drugs/compounds in culture [18-20]. It is particularly useful in screening for the optimal drug concentration or dose that should be used in treatments [21].

The technique also lends itself to a host of other applications since many cellular events are attachment-based. For example, cell motility or the movement of cells in culture can be measured using ECIS which lets us compare closely related cell lines for activity in culture [22-24]. Wound healing assays have also been developed in which the cells on top of the electrode are removed by electroporation and subsequent cell migration to the wounded site is measured [25, 26]. A short pulse of a higher voltage or current spanning a few minutes is applied which kills the cells located on the electrode causing them to detach accompanied by a fall in the impedance value measured from the electrode. When the surrounding cells migrate onto this newly available free area on the electrode, the impedance measurements pick it up by reflecting a rise in the values recorded.

Alternately, cell adhesion on the electrode area is actively prevented by applying a pulsating electric field. When the area around the electrode has a confluent cell culture, the electric field is turned off and the impedance is monitored as cells migrate into this region. Electroporation when used on smaller time-scales can result in the enlargement of pores in the cell membrane causing cells to take up molecules, particles and compounds from the surrounding medium that normally would not make their way into the cell interior. Electroporation assays have been developed in conjunction with ECIS that measure the optimal electroporation conditions that allow for the uptake of larger molecules of drugs or nanoparticles with fluorophores for imaging [27-29].

1.3.3. Single-cell Impedance Technologies

One of the first examples of a cytometer is the Coulter counter in which two chambers are connected by a small orifice with one large electrode in each chamber. The chambers are filled with a conductive liquid with particles or cells. As these particles move between the chambers through the orifice, the impedance measured increases. Also, a larger particle would block the current more when moving through the orifice resulting in a higher impedance change. Conversely, a smaller particle will not occupy as much space in the orifice and therefore block lesser current causing a lower change in impedance. A smaller orifice will have more sensitivity and can detect smaller particles as well. One of the limiting factors of the traditional Coulter counter is that the measurements are made only with a DC supply. However, it is still widely used in hospitals to provide blood counts rapidly. It also part of some commercially available flow cytometry systems.

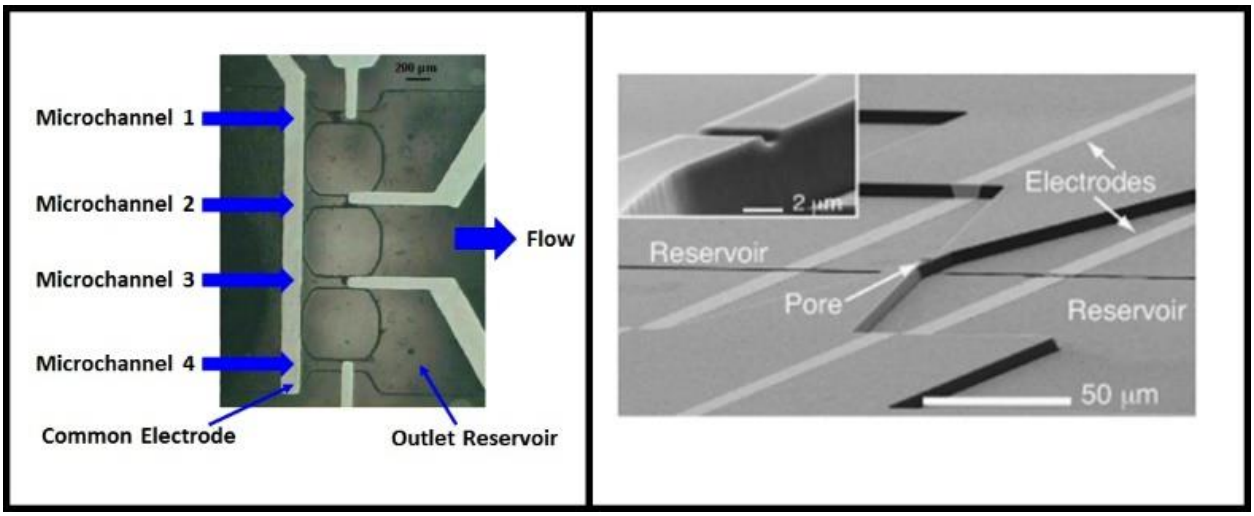

Figure 1.5 Examples of fabricated micro-scale coulter counters for bioparticle analyses. Image on right reproduced from [30] with permission from AIP Publishing LLC. Image on left reproduced from [31] with permission from IOP Publishing.

The first micro-scale Coulter counters designed work on the same principle, but on a smaller scale, and were fabricated on silicon, glass as well as PDMS. These devices had a sensing pore region instead of an orifice for detection. As these devices have evolved, although they use the same principle of detection, they no longer adhere strictly adhere to the design of the Coulter counter. A number of different designs have been used including higher throughput devices with multiple channels each with its own set of test electrodes to increase the number of particles analyzed and a channel with a flow-based programmable pore size that enables testing samples of different sizes on the same devices and tuning the sensitivity based on application [30-32]. **Figure 1.5**, shows some examples of microfluidic devices based on the concept of the Coulter counter used for single cell analyses. Using the micro-Coulter counter and its design variants, a number of different samples of interest have been analyzed. Examples include mammalian cells, red and white blood cells, nanoparticles that capture specific antibodies even single molecule analyses of DNA, RNA and others.

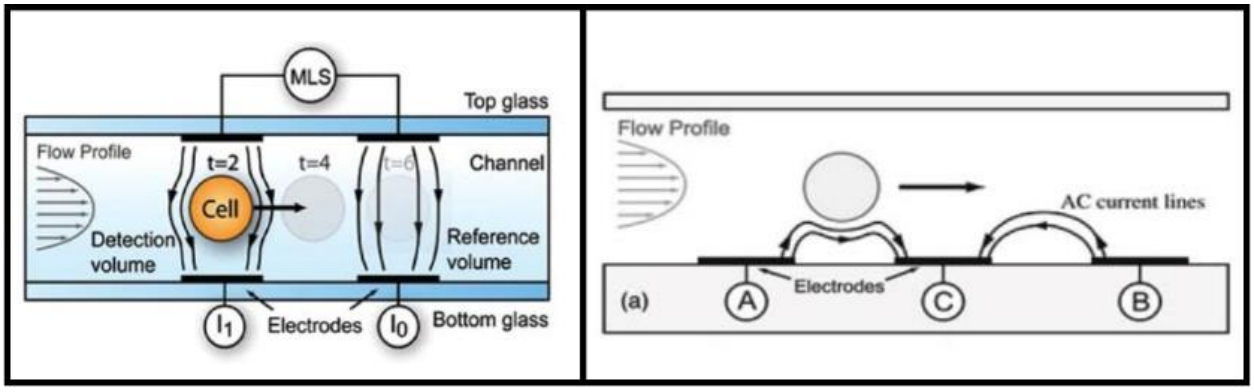

Figure 1.6 Flow cytometry to probe to the dielectric properties of single cells flowing in a microfluidic channel using impedance spectroscopy. Image on right reproduced in part from [33] with permission from The Royal Society of Chemistry. Image on left reproduced from [34] with permission from AIP Publishing LLC.

When the above concept is extended to include AC impedance measurements at multiple frequencies the devices can be used to probe the dielectric properties of the cells [35]. **Figure 1.6** shows an example of such a device where the cells are flowing through a microfluidic channel that is larger than their size and gold electrodes integrated into the channel measure the changes as single cells pass across them. The electrodes can be positioned laterally on the same surface or on opposite surfaces in the microchannel. In both cases, an impedance change is recorded due to the change in the current path as shown in the schematic in **Figure 1.6**. It also needs to be reiterated that the sensitivity of the impedance measurements is related to the frequency at which they are

made. At lower frequencies, the current path bends around the cell causing the measurements to be sensitive to size of the cell. However, at higher frequencies, the currents pass through the cells and are thus sensitive to cell membrane and cytoplasm properties. The technique has been proven to be sensitive enough to differentiate between particles of different sizes like red blood cells (6-8 μm) and polystyrene beads (4-6 μm) [36], and closely matched cells like healthy and diseased red blood cells [37] as wells as normal and cancer cell lines of the same tissue [38]. Although the flow in microfluidic channels is planar and it is possible to measure the impedance of single cells without any additional design, to decrease any clogging issues and increase the rate and confidence of single cell measurements, active focusing and trapping mechanisms are often incorporated into the design. For instance, two auxiliary channels are present on either side of the input channel and flow in established in them to focus the cells coming from the input channel as a row of single cells [39]. Another strategy is to apply a negative pressure through a tiny pore located between the electrodes to ensure that a single-cell is positioned right in the middle of the electrodes [38]. This also ensures that there are no discrepancies in the measurements due to the cell position being partial in one direction towards one of the electrodes. Dielectrophoretic trapping has also been used to position single cells between the measurement electrodes by incorporating more electrodes through which the electric fields required for dielectrophoresis can be supplied [40].

Electrodes can also be used to monitor events in a narrow microfluidic channel that is smaller than the size of the cell. Impedance measurements can be used to simultaneously measure the mechanical and the electrical properties of single cells [41-43]. A constant negative pressure is applied at one end of the channel which forces the cells to deform and travel through it. The width of the impedance profile gives the time that single cells take to traverse through the channel which in turn is a measure of the mechanical properties of these cells [44]. Additionally, the impedance measurements made in such a channel are more sensitive to the internal properties of the cell, especially at higher frequencies, because the leakage current around the cell is minimized. Hence, impedance cytometry can be integrated into the microfluidic platform to generate a wide array of microdevices that have applications over a wide spectrum ranging from particle counting, size determination, single cell and molecule analyses.

1.3.4. Strategies to Improve Specificity and Sensitivity

Use of a sensing layer on top of the electrodes to effectively couple them to specific analytes of interest is one of the most commonly used techniques to improve specificity [45]. **Figure 1.7**

shows an illustration summarizing the idea. Self-assembled monolayers is a popular method used to immobilize the biorecognition element on the electrode surface. Thiol end-groups spontaneously chemisorb and form well organized monolayers on gold electrodes. Thus, the recognition compound can be functionalized chemically to self-assemble on the surface. Polymer and polyelectrolyte films capable of binding to biomolecules have also been used successfully to capture target analytes. The field of biosensors for immunosensing, for instance, has grown largely using this detection mechanism. The selective binding between antibody and antigen is exploited and either the antibody or the antigen that complements the antigen or antibody in solution is immobilized on the surface of the electrode [46]. When the complementary molecule binds to the antibody or antigen, the impedance changes and detection is achieved. In some sensors, selected enzymes are deposited on the surface of electrodes by combining them with other materials or compounds. The catalytic action of the enzyme on the biomolecule of interest results in detection through a change in the measurement from the electrode [47]. It is also possible to analyze DNA concentration or base-pair mismatches using electrochemical sensors by comparable strategies [48]. Similarly in the detection of cancer cells which overexpress certain receptors or proteins (for example: epithelial cell adhesion molecule (EpCAM)), the ligand or antibody that binds to these receptors are immobilized on the electrodes in an effort to sensitize these electrodes to cancer cells [49, 50]. Electrochemical sensors have also been developed for the detection of glucose and urea levels in samples obtained from patients [51, 52].

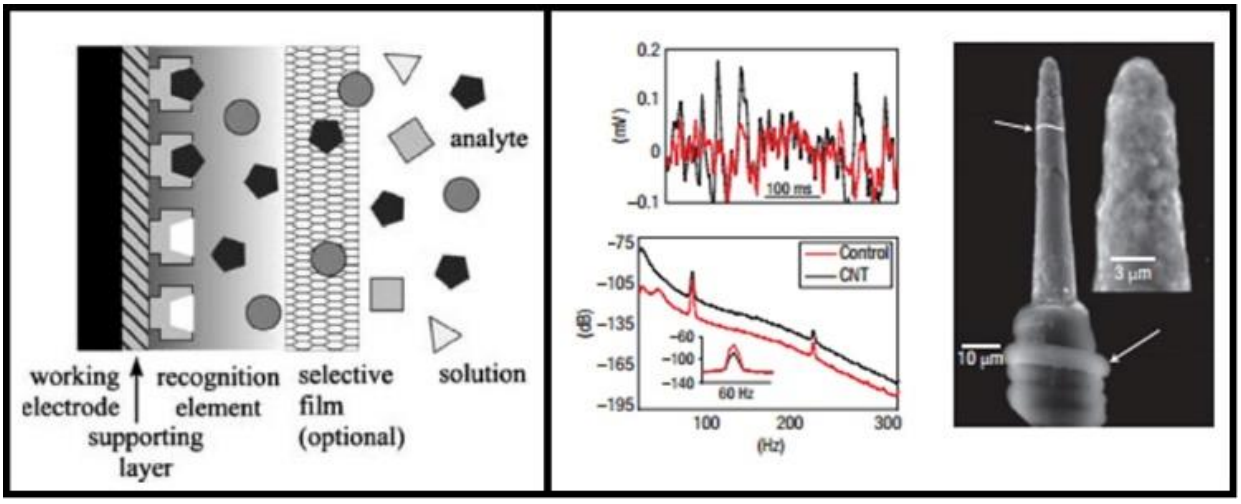

Figure 1.7 Strategies to achieve specificity (left) and improving sensitivity (right) in impedance sensing. Image on right reproduced from [45] with permission from Nature Publishing Group. Image on left reproduced from [53] with permission from Springer.

To increase the overall sensitivity of electrodes to impedance measurements, a common strategy is to increase the surface area of the electrode by depositing or growing carbon nanotubes (CNT) [54, 55], coating the surface with conductive nanoparticles or composites of them [56-58]. These coatings have shown to be effective in improving the sensitivity of measurements from neurons, electrochemical sensors for analysis of human body fluids as well as cancer cells [54-56]. **Figure 1.7** (right) shows the image of an electrode that is coated with CNTs after use for neuronal recordings from a monkey's visual cortex. The inset graphs show the increased sensitivity (top) and improved power and noise performance (bottom) compared to uncoated control electrodes [53].

1.4. Breast Cancer

One in eight women in the United States bears the risk of developing breast cancer during their lifetime [59]. In 2015, 29% of all cancers diagnosed in women will be breast cancer making it the most common type of cancer among women in the United States [60]. When a patient is diagnosed with breast cancer, a hormone receptor assay is also performed to determine whether the cancer cells have receptors for the two female hormones estrogen and progesterone. This determination enables the use of targeted hormone therapies against these breast cancers. The presence of receptors for estrogen (ER+) and progesterone (PR+) in the tumor indicates that it grows in response to signals from these hormones. Collectively, these tumors are classified as hormone receptor positive and roughly two out of three tumors diagnosed fall under this category. Women with hormone receptor positive tumors have the best overall survival rate and prognosis [61]. These patients can receive hormone therapy wherein drugs are administered, that block the hormone receptors (example: Tamoxifen) in breast cancer cells or stop hormone production (example: Aromatase inhibitors) to effectively decrease the rate of growth or even shrink these tumors. However, some patients do not respond to or acquire resistance to hormone therapy in spite of testing positive for hormone receptors. This presents a unique challenge and requires the development of new targeted therapeutic agents and approaches. The other test performed on breast cancer is for overexpression of human epidermal growth factor receptor 2 (HER2). One in five women with breast cancer test positive for HER2 and can be treated with drugs such as herceptin that intercept the pathway for cancer cell proliferation by binding to the HER2 receptor. Breast cancers that test negative for both hormone receptors and HER2 are known as triple negative breast cancer (TNBC). This subtype has the highest mortality rate for which targeted

therapies are still under development [61, 62]. In this work, we focus on triple negative and hormone resistant breast cancer cell lines as a test model with the goal of using bioimpedance of these cells as a means to detect breast cancer cells, distinguish molecular subtypes and evaluate cell response to therapeutic agents.

1.5. Bioimpedance and Cancer

In the last few decades, bioimpedance has become a useful tool to study the electrical properties of cancer cells. Although it is understood that there are differences between normal and cancer cells, the depth of our knowledge with respect to the similarities and differences in their electrical properties is quite limited. It has become increasingly clear as more reports on the electrical properties of various types of cancers are published, that the impedance of cancer and normal cells are indeed different [38, 63-66]. Cancer cell invasion through a confluent layer of endothelial cells has also been monitored using real-time ECIS measurements [67, 68]. As mentioned before, the technique can also be used to screen the efficacy and optimal dose of anti-cancer agents on different types of cancer cells. These tests, in the future, could be carried out on patient samples to provide individualized reports of drug effectiveness which can then be used to make treatment plans for the patient. **Table 1.1** below, summarizes previous research published on the bioimpedance of various cancer cells.

Table 1.1 Summary of research reports on bioimpedance analyses of cancer cells.

Cancer Type	Cell Lines	Key Contribution
Oesophageal Cancer	KYSE30	Normalized impedance at 1 kHz is an indicator of chemosensitivity to Cisplatin [20].
Breast Cancer	MCF10A, MCF-7, MDA-MB-231, MDA-MB435	Magnetophoresis microseparator to separate breast cancer cells from blood. Positioning of single cells in microcavities for EIS. Cancer cell lines displayed lower impedance magnitude [38, 69].
Oral Cancer	CAL27, Het-1A	Cell index from RT-CES system captures the inhibitory effect of nicotine on apoptosis induced by cisplatin [21]. Cell index also captures kinetics of cell spreading differentiated normal and oral cancer cells [65].
Glioblastoma	U87MG	Impedance measurements at 2 kHz captures single cell responses to the chloride ion channel inhibitor chlorotoxin [70].
Breast Cancer	MDA-MB-231	Impedance parameters captured decreased motility and migration in the presence of recombinant human MDA-7 gene [71].

Head and Neck Cancer	686LN-M4e, 686LN	Phase angle obtained from trapped single cells was shown to differentiate the poorly metastatic from the highly metastatic cells [66].
Colorectal, Lung and Breast Cancers	Patients	Phase angle obtained using BIA is a prognostic indicator in patients with advanced colorectal, lung and breast cancer [15, 72-74].
Ovarian Cancer	OVCA429	Equivalent circuit model including cell and interfacial components used to characterize resistance (152±59 Ωcm^2) and capacitance (8.5±2.4$\mu F/cm^2$) of cell layer [75].
Cervical Cancer	HeLa	Impedance of hydrodynamically trapped single cells captures gradual lysis of cell membrane using Tween and toxin activity of streptolysin-O [76].
Colon and Breast Cancer	HT29, SW48 MCF-7, MDA-MB-231	Impedance of single cells measured using vertically aligned carbon-nanotubes decreases with metastatic progression [77]. The presence of even 5% metastatic cells in a mixed culture was detected as a decrease in impedance in a silicon nanograss electrode [78].
Breast, Lung and Cervical Cancers	MCF-7, MDA-MB-231, HeLa, A549	Impedance of single cells trapped using DEP force were characterized over 20-100 kHz frequency range and different cells were shown to have varied tolerance to electric fields [79].
Kidney, Lung and Breast Cancers	786-O, CRL-5803, CCl-185, 95D, 95C, A549, H1299 EMT6, EMT6/AR1.0	Single cells were aspirated through a constriction channel and impedance measurement at 1 and 100 kHz was used to obtain cell electrical parameters. Specific membrane capacitance and cytoplasm conductivity was characterized. Capacitance was shown to be lower in metastatic cell lines in paired tests [41, 43, 80, 81]

1.6. Research Objective

The long-term vision for this work is the use of bioimpedance signatures in personalized medicine to profile cancer cells obtained from patients and predict their response to pharmaceutical agents. My dissertation lays the groundwork to achieve this grand challenge by adopting a three-pronged approach to the solution. These include

1. Development of miniaturized bioimpedance sensors using microelectromechanical systems (MEMS) technology for measurements from individual cells and cell populations.
2. Optimization of the physical design (geometry and surface properties) of microelectrodes to improve sensitivity.
3. The fundamental characterization of the bioimpedance signatures of triple negative and hormone therapy resistant breast cancer cell lines and their responses to pharmaceutical drugs.

This dissertation provides detailed account of my research efforts and is organized as follows.

Chapter 1. provides the reader with the basics of bioimpedance, its unique advantages and an overview of technologies that employ this technique. **Chapter 2.** provides a summary of the first generation bioimpedance sensor designed and its use in measuring breast cancer cell responses to a histone deacetylase inhibitor (HDI). The selective response of cancer cells to the HDI was used to detect cancer cells present in a population normal breast epithelial and fibroblast cells on the electrode, which is representative of a simulated biopsy sample. This work was conducted as part of my Master's thesis and provides the background and motivation for work presented later in this document.

Chapter 3. documents the bioimpedance profiles of a select panel of cell lines that belong to the clinically relevant triple negative subtype of breast cancer obtained using our second generation bioimpedance sensor. The unique bioimpedance signatures elicited from basal and claudin-low subtypes due to the morphological differences between them is highlighted. In **Chapter 4.** , conductive nano-scale coatings on the electrode were explored as a strategy to increase sensitivity to bioimpedance measurements. **Chapter 5.** details the development of a high-throughput bioimpedance assay system in a 6X6 array format. The flexibility and reconfigurable nature of various elements of the system are highlighted. The effect of design parameters on the sensitivity of the branched electrode was investigated using nine different electrode geometries on a single device.

It is becoming increasingly clear that cells present within the same tumor may have very different properties and the characterization of individual cell properties is crucial to understand and predict events such as cancer metastasis and therapy resistance that significantly change patient outcomes. This motivated the development of a microfluidic biosensor capable of measuring the bioimpedance response of individual cells subject to mechanical stress, which is documented in **Chapter 6.** .

Chapter 7. covers the use of both of the aforementioned devices to characterize the bioimpedance responses of a hormone therapy resistant cell model to the drug Obatoclax. Finally, the outcomes of my research efforts are summarized and future directions for this work are discussed in **Chapter 8.** .

2. Background and Motivation

This section provides a summary of the previous research work conducted as part of my Master's thesis. It is partly reproduced from [82-84] with permission from Royal Society of Chemistry and IEEE.

Srinivasaraghavan V, Strobl J, Agah M. Bioimpedance rise in response to histone deacetylase inhibitor is a marker of mammary cancer cells within a mixed culture of normal breast cells. Lab on a Chip. 2012;12:5168-79.

Srinivasaraghavan V, Strobl J, Agah M. Chemical induced impedance spectroscopy for single cancer cell detection. Solid-State Sensors, Actuators and Microsystems Conference (Transducers). Beijing, China2011. p. 2247-50.

Srinivasaraghavan V, Strobl J, Agah M. Detection of breast cancer cells in tri-culture using impedance spectroscopy. 15th International Conference on Miniaturized Systems for Chemistry and Life Sciences. Seattle, WA: Royal Society of Chemistry; 2011. p. 1713-5.

2.1. Introduction

Electrical Cell-substrate Impedance Sensing (ECIS) was introduced by Giaever and Keese as a non-invasive method to study the properties of cell attachment [85]. Cells adherent to gold electrodes integrated into a cell culture chamber are probed with AC current over a range of frequencies. The measured AC impedance of cell covered electrodes provides a highly sensitive measure of alterations in cell attachment and shape that is responsive to changes in current flow through and around the cell. Bioimpedance measurements are typically expressed as a magnitude (in Ω) and phase (in degrees) at a particular frequency or over a frequency range (kHz-MHz). ECIS has been used to monitor various properties of cells including attachment and spreading [16, 19, 86], motility [22, 87], and growth and proliferation [17]. Impedance measurements can be calibrated to monitor cell proliferation [88] and to monitor the response of cells to drug treatment in real time [70, 89]. The properties of single cells within a population of cells can be analyzed to better understand cellular activity and heterogeneity at single cell levels [40, 90-93]. Electrodes used for impedance measurements can be easily integrated into microfabricated devices [40]. Advantages of microelectromechanical systems (MEMS) such as batch fabrication, low cost, integration with electronics and microfluidic components make it a promising approach to design ECIS-based biosensor chips to gauge changes in cellular physiology.

ECIS and other impedance-based techniques have proven to be a valuable tool in cancer research. Liu et al. studied the anti-proliferative response to cisplatin of cultured human oesophageal cancer cells (KYSE 30) cultured on microelectrodes coated with fibronectin [20].

Similarly, cellular activity and drug induced apoptosis of oral squamous cell carcinoma (OSCC) using ECIS were studied by Arias et al[21]. Single cell bioimpedance analyses show promise as a means to discriminate normal and malignant cells and to assess metastatic properties. Differences between the cancerous OSCC cell line and the non-cancerous derived epithelial oesophageal cell line (Het-1A) were investigated using the impedance response measured using a commercially available RT-CES system [65]. Cho et al. reported statistically significant differences occur in the phase angle of the corresponding impedances of highly and poorly metastatic head and neck (HNC) cells[66]. Single cell analysis of non-tumorigenic MCF-10A and breast cancer cell lines MDA-7 (early stage), MDA-MB-231 and MDA-MB-435 (metastasized) was done by Han et al[38]. The magnitude and phase of measured impedance over the frequency range of 100 Hz to 3 MHz differed among these lines; also the differences in membrane capacitance and resistance at 100 kHz obtained through modelling were reported. Qiao et. al. reported differences in the impedance measured from a suspension of MDA-MB-231 and MCF10A breast cells using platinum needle electrodes [94]. Hong et al. presented a microfluidic device that captures a single cell using dielectrophoresis forces and then measures its impedance. The device is capable of differentiating between the MDA-MB-231 cell and the MCF-7 cell using the parameters obtained from modelling the impedance measurement [95].

More recent improvements in microengineering have extended the utility of ECIS in cancer research. Abdolahad et al. incorporated vertically aligned carbon nanotubes on microelectrodes to accelerate cell adhesion and demonstrated rapid detection of SW48 human colon cancer cells [54]. Researchers have also designed microelectrodes that can be used as a switch to detect to presence or absence of a single MCF-7 breast tumour cell [49]. Thus, bioimpedance technologies hold promise in cancer diagnosis and prognosis.

Detection of a few cancer cells within a complex cellular mixture is a key challenge presented by clinical human biopsy samples. We designed and tested a microfabricated bioimpedance device that can detect a few human MDA-MB-231 breast cancer cells in a mixed cell culture model of a breast tissue sample. The normal tissue components were modelled using non-cancerous MCF-10A human breast epithelial cells and normal human HS68 fibroblasts. The sensor is a silicon chip 0.5 cm in diameter that contains one counter electrode and four 40 mm-wide multi-branched sensing electrodes. The cells' bioimpedances were characterized in pure monocultures and in

mixed cell cultures following a brief cultivation on the sensor. After cell seeding, a stable bioimpedance signal was achieved indicative of cell attachment. A cancer-selective bioimpedance signal was elicited by addition of suberoylanilide hydroxamic acid (SAHA), a histone deacetylase inhibitor with selective actions on the cytoskeleton in breast cancer cells. SAHA elicited a 50% rise in peak bioimpedance in MDA-MB-231 breast cancer cells by 15 h. In mixed cultures of MDA-MB-231, MCF-10A, and HS68 cells, the contribution of cancer cells present in the mixture dominated impedance response to SAHA. A single adherent cancer cell on any one of four electrodes in a background of 100 normal cells resulted in ≥5% increase in bioimpedance. The estimated sensitivity of this device is therefore one cancer cell among a background of 400 normal cells or the equivalent of 25 cancer cells in a biopsy sample of 10 000 cells.

2.2. Sensor Design and Fabrication

Figure 2.1 shows the schematic of our bioimpedance sensor and an optical image of the fabricated device. A large counter electrode (2 mm in diameter) in the center was used to minimize the potential drop over it and to make the sensing electrode more receptive to the bioimpedance changes. Narrow branches of electrodes, 40 µm-wide and 650 µm-long separated by 130 µm, were designed to enhance bioimpedance translation of the changes in cell attachment and spreading. The electrode branches were designed so that their width was comparable to the size of the cells used in our analyses.

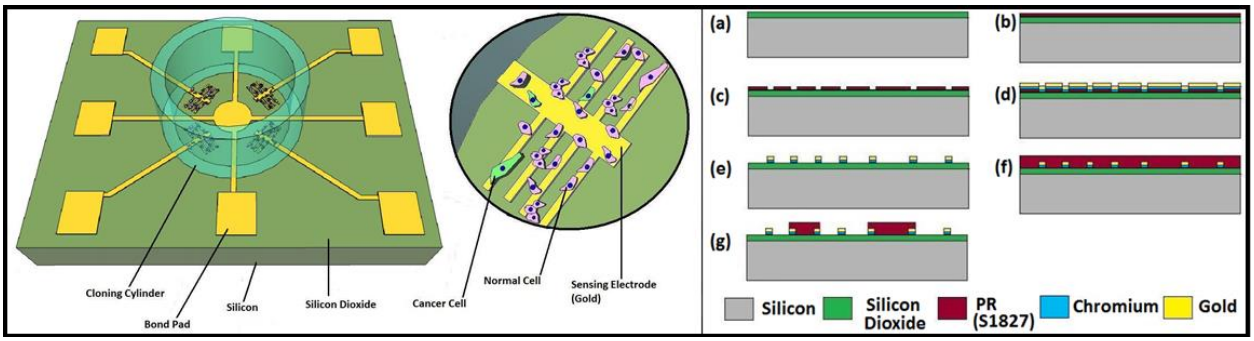

Figure 2.1 Conceptual illustration (left) and process flow for the fabrication (right) of the bioimpedance sensor.

Also multiple branches result in improved electrode coverage in the sensing area of the bioimpedance sensor which enhances the chance of detection of sparsely present cancer cells. A layer of photoresist was deposited as a passivation layer over all the electrodes to precisely define

the sensing area as a circular window. The bioimpedance sensor chips were packaged with a cloning cylinder with a capacity of 300 µl which surrounded the sensing area and held the cell culture medium and the cells during experiments.

The sensor was fabricated according to the process flow shown in **Figure 2.1** (right). A sterile silicon wafer was used as the starting material. An oxide layer approximately 5000 Å thick was grown on the silicon wafer using thermal oxidation in an oxidation chamber (**Figure 2.1-a**). The wafer was then coated with photoresist (Shipley 1827) about 2 µm thick using a binder (HMDS) by spin coating (**Figure 2.1-b**). Next, the photoresist was patterned using the first mask containing the electrode design, (**Figure 2.1-c**). A 250 Å/1500 Å Cr/Au layer was then deposited on the wafer using electron-beam evaporation technique (**Figure 2.1-d**). The wafer was left in acetone overnight and then placed in a sonic bath for 15 s to ensure complete lift off (**Figure 2.1-e**). A 2 µm-thick photoresist was once again spun coated on the wafer (**Figure 2.1-f**) and patterned using the second mask to form the passivation layer (**Figure 2.1-g**). The wafer containing multiple devices was then diced manually to yield individual bioimpedance sensor chips. These chips were packaged with a cloning cylinder (Fischer Scientific: 14-512-79) around the sensing area by affixing them with photoresist to prevent the cell culture medium from leaking. It should be mentioned that no surface treatment was done to the electrodes to promote cell adhesion in the devices used for the results obtained in this paper.

2.3. Experiments

The measurement setup used to make bioimpedance measurements has been described in a previous paper [96]. MDA-MB-231, MCF-10A and HS68 cell lines used in this study were obtained from American Type Culture Collections (ATCC). The MDA-MB-231 (Passage 10) and MCF-10A (Passage 8) cells were stably transfected with green fluorescence protein (GFP) and mCherry red fluorescent protein, respectively, to enable us to capture fluorescent images of the electrodes and sensing area after every experiment [97]. The experiments were run with transfected MDA-MB-231 and MCF-10A cells with passage numbers 1-16 and 11-24, respectively, after transfection. The HS68 cells (Passage 11-15) were stained with CellTrace™ calcein red-orange dye from Invitrogen using methods recommended by the supplier. All cells were counter stained with Hoechst 33342 dye, which stains the nucleus of the cell blue, at the end of each experiment to facilitate cell counting. The cells were counted and suspended in 200 µl of respective culture

media for the monoculture experiments before being introduced into the cloning cylinder of the bioimpedance sensor. MCF-10A cell culture medium was used for the multi-cell culture experiments. We set the cell density at 8000 cells/200 µl for the monoculture experiments and 6000 cells/200 µl for the multi-cell culture experiments. The viability of the cells exceeded 95% under our assay conditions. SAHA was obtained from LC Laboratories (Woburn, MA V-8477). Stock solution (5.5 mM) were prepared in 100% DMSO and stored at -20˚C.

2.4. Bioimpedance Measurements

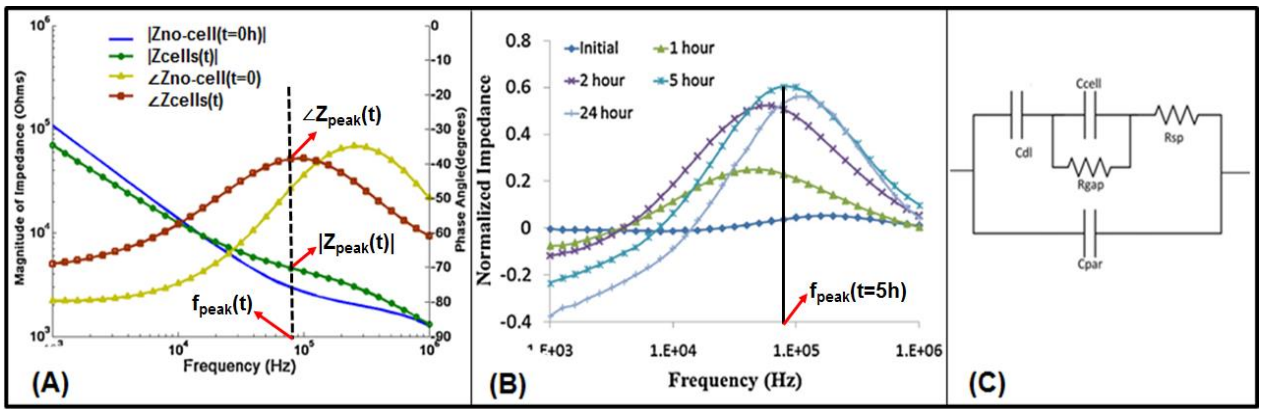

Figure 2.2 (A) Magnitude and phase of the bioimpedance spectrum, (B) normalized magnitude, and (C) equivalent electrical circuit to model bioimpedance signatures.

Figure 2.2 depicts the bioimpedance data obtained from cells as well as the equivalent electrical circuit to model the impedance signals [96]. The bioimpedance data are a set of complex numbers, each corresponding to a particular frequency in the range 1 kHz-1 MHz, in which each value has a magnitude and phase denoted collectively by the symbols |Z| and ∠Z, respectively. Zno-cell refers to when there are no cells on the electrodes, and hence, represents the culture medium only. Following cell seeding, measurements can be taken continuously over time (Zcell(t) in **Figure 2.2(A)**) to monitor cell attachment, cell growth and confluence on electrodes, and cell responses to any external stimulus such as drugs. The normalized magnitude (|Znorm(t)|) is shown in **Figure 2.2(B)** and calculated using the formula shown in Equation 1 where |Zcell(t)| denotes the impedance of the cells present on the electrode at time 't'.

$$|\text{Znorm(t)}| = \frac{|\text{Zcell(t)}| - |\text{Zno-cell}|}{|\text{Zno-cell}|} \qquad (1)$$

There is a peak associated with the normalized bioimpedance magnitude at every time point at a specific frequency which we determine as the peak frequency (fpeak(t)). The magnitude and phase of the bioimpedance corresponding to this frequency is the peak bioimpedance magnitude (|Zpeak(t)|) and peak phase (∠Zpeak(t)). The elements in the model shown in **Figure 2.2(C)** include the double layer capacitance (Cdl), spreading resistance (Rsp), parasitic capacitance in the circuit (Cpar), and impedance due to the cells represented by a capacitance (Ccell) in parallel with the resistance of the cell substrate gap (Rgap).

2.5. Summary of Results

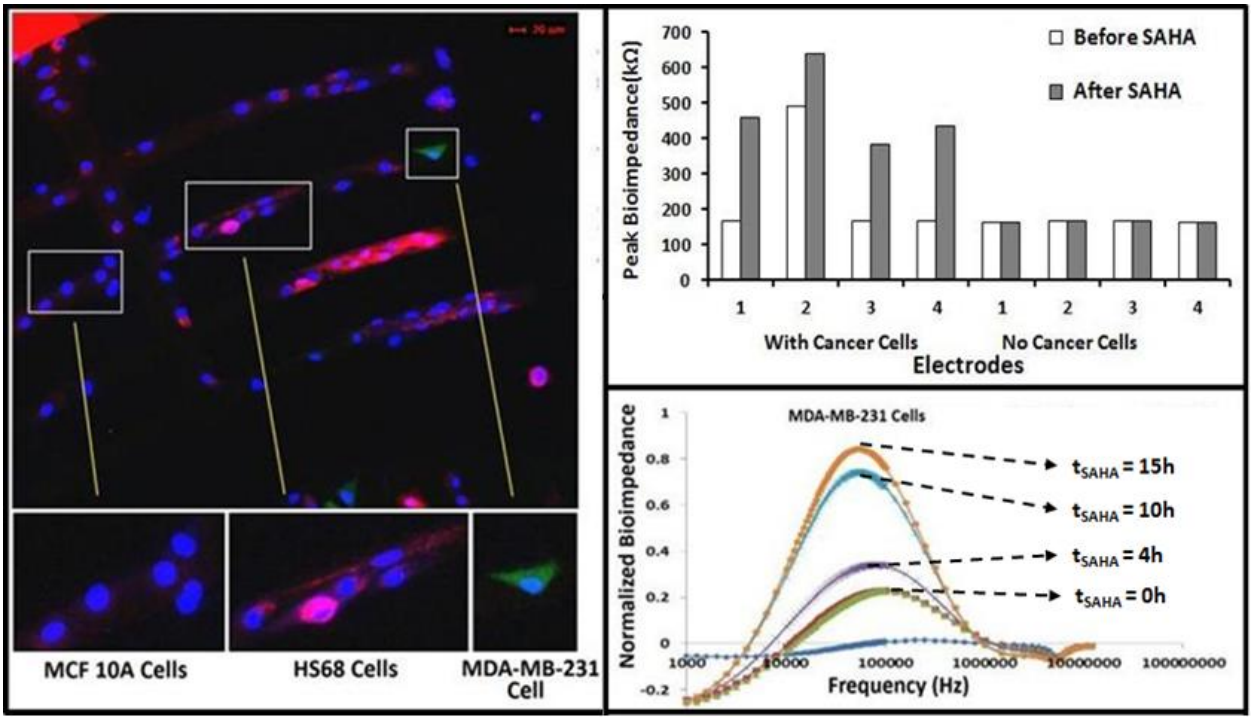

Figure 2.3 Bioimpedance data with MDA-MB-231 breast cancer, MCF10A normal breast epithelial and HS68 fibroblast cells.

Using these bioimpedance chips, we have been able to detect the presence of even a single MDA-MB-231 cell adherent on the electrodes while containing a mixture of normal cells (ratio of about 1:500) at 80% confluency. This sensitivity was achieved by two innovations in our approach: 1) fabrication of electrodes with thin branches similar in width to that of the cancer cell and 2) the use of the HDI SAHA to stimulate a rapid bioimpedance response selectively in the malignant cells. This is the basis of the future work proposed in this document. **Figure 2.3** shows the three cell types adherent to our thin-branched electrode and includes GFP-MDA-MB-231. On the right, is a typical normalized impedance spectrum ($|Z_{norm}|$) collected over a frequency range of 1 kHz–1

MHz from this electrode. Recently, we have been able to reduce the time for pre-SAHA (i.e., between initial cell seeding till cell attachment and confluence) from our published 20 h [82] to 5h by reducing the volume of the initial culture medium from 200 µl to 50 µl. Nevertheless, the series of curves displays representative data collected right before SAHA (t_{SAHA}=0), and 4, 10, and 15 h after adding 500 nM SAHA. The increase in the magnitude of the bioimpedance signal over time in the presence of SAHA can be seen here. In addition, the peak frequency shifts over time in SAHA from ~95 kHz to ~55 kHz. The bar graph (right top) depicts bioimpedance magnitude at peak frequency right before SAHA (open) and 15 h post SAHA (gray); each pair of bars represents one randomly selected electrode from 3 independent experiments. As can be seen, SAHA provoked a rise in the peak impedance when cancer cells were on the electrode. A clue to understanding why bioimpedance shifts in homogenous cultures of MDA-MB-231 cells but not the normal cells is the selective increase in MDA-MB-231 cell area in response to SAHA that resulted in nearly a doubling of the electrode coverage per cell [82].

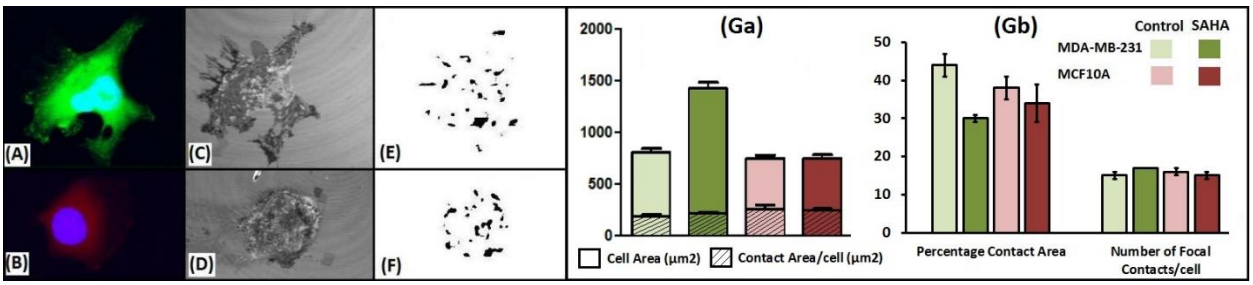

Figure 2.4 (A), (C) and (E) represent the confocal, IRM and binary image of an MDA-MB-231 cell. (B), (D) and (F) represent the corresponding images for MCF10A cell. (Ga) shows the cell area and contact area/cell and (Gb) shows percentage contact area and number of focal contacts/cell for control and SAHA treated MDA-MB-231 and MCF-10A cells.

Since, bioimpedance is a function of the adhesion of cells to the electrode which can be influenced by the cell area, the cell-electrode contacts and the gap between the cell and the electrode (substrate). Here, to understand the mechanism for the selective SAHA bioimpedance increase in cancer cells, we used interference reflection microscopy (IRM) to test our hypothesis that SAHA selectively increases the cell-substrate contact area in MDA-MB-231 cancer cells and not in MCF-10A control cells. IRM yields gray-scale images of cells in which intensity differences are due to the interference of reflected light and provide a quantitative measure of the distance between the cell and the substrate. MDA-MB-231 and MCF-10A cells were allowed to attach onto glass coverslips for 20 h, then 500nM SAHA was added for 15 h. The cells were washed, fixed in 3% paraformaldehyde, re-washed and the nuclei were stained with Hoechst 33342. Coverslips

were inverted and mounted on another coverslip using ProLong Gold anti-fade (Invitrogen), then air-dried in the dark for 24h. IRM imaging was performed using a laser scanning microscope (LSM510 META, Zeiss) and the protocol of Barr et al [98]. Z-stack confocal and IRM images were obtained and exported as tiff files. An image processing program written in Mathematica™ was used to generate binary images from the IRM tiff files in which the black areas represented areas of contact between the cell and the substrate. ImageJ was used for the cell area and contact area measurements in each field. The contact area per cell was calculated as the area of the black regions divided by the number of cells (counted using Hoechst stained nuclei) in each field **Figure 2.4(Ga)**; the percentage contact area was calculated by dividing the area of the black regions by the area of the cell (**Figure 2.4(Gb)**).

Using IRM and image processing, we identified the black patches as areas of contact between the cell and the substrate for 116-167 cells/group in control and SAHA treated MDA-MB-231 and MCF-10A cell groups in n=3 experiments. MDA-MB-231 cell area was significantly increased (*) in response to SAHA, but not in control MCF-10A cells. However, the contact area/cell did not change significantly in response to SAHA in either MDA-MB-231 or MCF10A cells (**Figure 2.4(Ga)**). The average number of focal contacts per cell ranged between 15 and 17 and was not significantly changed by SAHA treatment. The percentage of cell area in contact with the substrate was in fact, significantly lower in MDA-MB-231 cells after SAHA treatment ($P<0.0001$) (**Figure 2.4(Gb)**). Thus it is unlikely that cell-substrate contacts mediate the bioimpedance rise due to SAHA.

2.6. Conclusion

This work presents a bioimpedance sensor capable of detecting human breast cancer cells in a background of normal cells and begins to analyze the mechanism underlying changes in bioimpedance that occur in breast cancer cells in response to a histone deacetylase inhibitor. Bioimpedance sensing using this type of device has potential application to the analysis of fine needle aspirates and breast core biopsy samples for the rapid detection of cancer cells.

3. Microelectrode bioimpedance analysis distinguishes basal and claudin-low subtypes of triple negative breast cancer cells

Srinivasaraghavan V, Strobl J, Agah M. Microelectrode bioimpedance analysis distinguishes basal and claudin-low subtypes of triple negative breast cancer cells. Biomedical microdevices. 2015;17:1-11.

3.1. Introduction

The electrical properties of biological samples can be assessed through bioimpedance measurements using a pair of electrodes. Bioimpedance sensing has gained broad acceptance for cell biological applications and its usage in cancer research is expanding [49, 100-104]. Bioimpedance measurements can be made on adherent or suspended populations of cells, cell suspensions flowing through microfluidic devices [63, 105], patients with breast cancer [106-108] and various cancer cell lines [65, 66, 109]. The versatility of bioimpedance techniques and rich information content afforded by bioimpedance spectroscopy are reasons for the excellent long-term prospects for low-cost, high-throughput bioimpedance sensing techniques for cell analyses.

One common commercially available method of bioimpedance sensing uses a pair of planar electrodes on a plastic tissue culture substrate. This method known as Electric Cell-Substrate Impedance Sensing (ECIS) utilizes a large counter electrode and a small sensing electrode [16, 110]. In a previous study, we approached the idea of using bioimpedance signals obtained using our ECIS chip on a silicon wafer to diagnose breast cancer cells within a simulated breast biopsy sample [82-84, 111]. The branched structure of the electrode maximizes coverage in the sensing area; in addition, we used a branch width comparable to the cell size which in our experience, encourages cell spreading along the electrode boundary, thus improving sensitivity [83]. By introducing varying numbers of human MDA-MB-231 breast cancer cells to these cultures, we defined a cancer bioimpedance signature indicative of the presence of sparsely present cancer cells. This work provided proof-of-concept that bioimpedance sensing is a new tool for diagnosing cancer pathology.

We predict that measuring the electrical properties of breast cells can provide diagnostic information to complement that gained through more complex immunohistochemical (IHC),

fluorescent *in situ* hybridization (FISH) and genomic analyses [62, 112-115]. There are limited data available on the electrical properties of human breast cancer cells and the parameters reported in studies thus far have not been standardized making it difficult to perform direct comparisons among the work from different laboratories. However, there is a general consensus that the bioimpedance signals from MCF-10A cells, a non-malignant line derived from human fibrocystic disease, differ from that of malignant breast cells, and that the more metastatic cell line, MDA-MB-231 is more distinct than the MCF-7 cell line that metastasizes poorly in animal model systems [38, 49, 77, 94, 116].

Here, we focused on a clinically important group of patients whose tumors lack hormone receptors for estrogen (ER), progesterone (PgR), and erbB2 (HER2) [117, 118]. These TNBCs are typically highly aggressive, prevalent in younger women and women of African descent, and a diagnosis of TNBC is predictive of a worse overall survival [62, 113, 115]. Classification of TNBC patient samples using standard pathology identifies two main sub-types: approximately 55% of TNBCs are basal-like and slightly more than 25% fall into the category of claudin-low [62, 115, 119]. The MCF-10A cell line is classified as normal, basal-like [120, 121]. These TNBC subtypes have been shown to be predictive of clinically significant measures such as the organ sites of metastatic spread [122, 123], the stem cell nature of the tumor cells [62, 112, 120, 124, 125], and the responsiveness of the tumor to different chemotherapeutic drugs [126, 127]. However, disparate classification of TNBC subtypes based upon IHC/FISH alone or genomic analysis is a source of consternation [62, 119, 128]. The addition of a bioimpedance marker to distinguish basal and claudin-low subtypes of TNBC would have clinical value. Here, we used our bioimpedance sensor with a multi-branch electrode design to collect impedance measurements from three TNBC cell lines and MCF-10A cells. Our analysis suggests that claudin-low TNBC may be distinguished using the peak phase angle of impedance.

3.2. Materials and Methods

3.2.1. Sensor Design and Fabrication

The design and fabrication of the devices used in this study are shown in **Figure 3.1** and follows our previous silicon-based work [82, 96]. The device consists of a large central circular counter electrode 2mm in diameter and four identical sensing electrodes radially distributed around the counter electrode. The sensing electrodes have a branched design; each branch is 40 μm-wide

x 650 µm-long and is separated from adjacent branches by 130 µm. **Figure 3.1(A-a)** shows the microelectrodes fabricated on a pyrex/glass substrate. **Figure 3.1(A-b)** shows a magnified view of the electrode geometry and was obtained using the stitch feature of the Zygo NewView™ 7100.

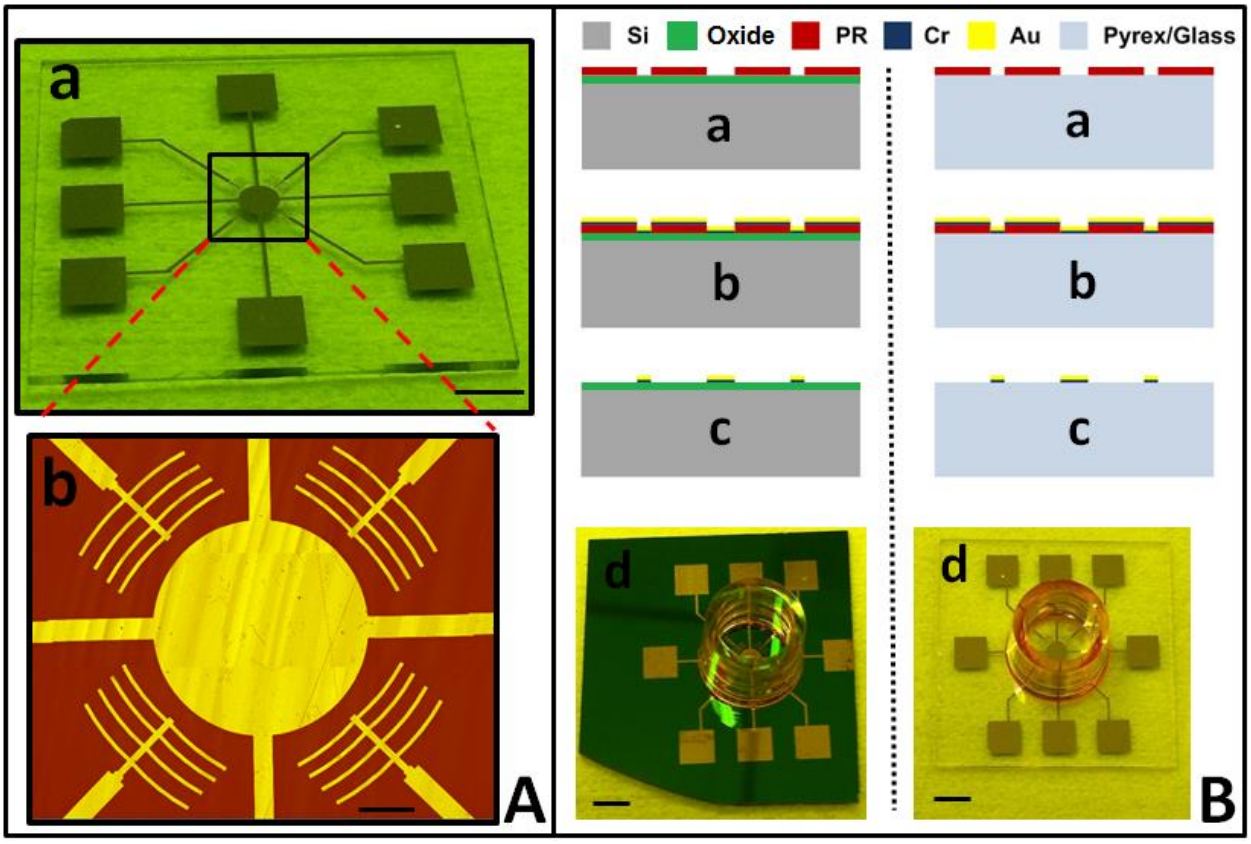

Figure 3.1(A-a) Image showing the fabricated microelectrodes on a pyrex/glass substrate. Scale bar = 3 mm (A-b) Enlarged view of the electrode design. Scale bar = 250 µm. (B) Process flow for the fabrication of the electrodes on both silicon (left) and pyrex/glass (right) substrates. (B-d) Fabricated devices packaged with cloning cylinder for experiments. Scale bar = 3 mm.

Figure 3.1(B) highlights the important steps in the process flow for the fabrication of the microelectrodes on silicon (left) and pyrex/glass (right) substrates. A thermal oxide layer (~ 500 nm) was grown on the silicon wafers prior to fabrication to electrically insulate the electrode layer from the silicon wafer. Positive photoresist (PR) such as the Shipley 1827 or AZ9260 was spun coated on the substrate. Photolithography was used to transfer the electrode pattern onto the substrate, followed by development of the photoresist in the appropriate developer (MF-319 or AZ-400K). **Figure 3.1(B-a)** shows the substrate after this step. Next, the metal layer was deposited on the substrate using e-beam evaporation in the PVD250 (Kurt J. Lesker). In this case, we deposited a thin 25 nm layer of chromium followed by a 100 nm thick gold layer as the metal layer as shown in **Figure 3.1(B-b)**. The chromium layer was used to promote the adhesion of gold on

the substrate. Finally, a lift-off process in acetone was used to remove the PR and obtain the metal electrode pattern on the substrate (**Figure 3.1(B-c)**).

Twelve devices were batch fabricated on a single wafer using the above process flow. Another layer of PR was spun-coated on the substrate to protect the devices from contamination from the lubricant during dicing. The individual devices were diced using a dicing saw (MA-1006, Micro Automation Inc.), then cleaned in acetone and Nano-Strip® to remove the PR and residual contaminants. Cloning cylinders (Scienceware™, Medium) were affixed onto the substrates using PR to provide a cell culture microwell (electrode chamber) using care to manually position them symmetrically around the electrodes. The packaged silicon and pyrex/glass devices are shown in **Figure 3.1(B-d)**.

3.2.2. Triple negative breast cancer

The cell lines used for these studies as shown in **Table 3.1** are validated models of clinically relevant TNBC [129]. All lines are negative for expression of receptors necessary for responsiveness to well-established hormonal therapies, and therefore represent tumors refractory to the more tolerable forms of treatment. MDA-MB-231 and Hs578T belong to the recently characterized basal cell subtype, claudin-low [112, 130]. These cells do not express any of the claudin proteins, produce very low levels of E-cadherin protein [113, 114], and as a result, cannot engage in cell-cell junction formation typical of normal mammary cells [62, 131, 132]. Claudin-low tumors exhibit high paracellular transport (cell leakiness) [133] and features associated with breast cancer stem cells, including chemo- and radiation-resistance [62, 112, 120, 124, 125]. This breast tumor subtype was earlier referred to as basal-B. In contrast, MDA-MB-468 cells express cytokeratins 5/6, claudins and the receptor for epidermal growth factor (EGFR); this cell line represents what is now known as the basal or basal-like subtype of TNBC, and displays a gene expression profile previously denoted as basal A that is the TNBC subtype more frequently seen in breast cancer patients [119, 121]. MCF-10A cells were derived from human mammary fibrocystic disease and are commonly used to model "normal" mammary epithelial cells. Although MCF-10A cells display morphological features of malignant cells when grown at low cell seeding densities in culture such as rapid growth, stellate cell morphology, motility, and actin stress fibers, at high density these cells display a cuboidal epithelial morphology and behave as normal basal breast epithelial cells [120, 132]. Contributing to this phenotype at high density are typical gene expression patterns including that of cytokeratins 5/6, E-cadherin, P-cadherin and claudins 1,4,

and 7 which support formation of cell-cell junctional complexes [134, 135]. All bioimpedance studies of MCF-10A cells were performed using cells under the high density condition.

Cell Name	Cell Derivation		Morphology	Molecular Subtype	Receptor Expression		
	Pathology	Site					
MDA-MB-231	Adenocarcinoma	Metastatic site: Pleural effusion	Epithelial, fibroblastoid	Claudin-low	ER-	PR-	HER2 -
Hs578T	Adenocarcinoma	Mammary gland/breast	Fibroblast	Caludin-low	ER-	PR-	HER2 -
MDA-MB-468	Adenocarcinoma	Metastatic site: Pleural effusion	Epithelial, cuboidal with cell-cell junctions	Basal	ER-	PR-	HER2 -
MCF10A	Fibrocystic disease, Non-tumorigenic	Mammary gland/breast	Epithelial, cuboidal with cell-cell junctions	Non-malignant Basal	ER-	PR-	HER2 -

Table 3.1 The triple negative breast cell lines used in experiments [112, 123].

3.2.3. Cell Preparation

The MDA-MB-231, Hs578T (a gift from Dr. Yasmine Kanaan, Howard University Cancer Center, Washington, DC), MDA-MB-468 and MCF-10A cell lines were purchased from American Type Culture Collections (ATCC) and maintained in accordance with ATCC recommendations. The cell cultures were maintained in T-25 cm^2 flasks in a humidified incubator (37 ^oC, 5% CO_2) and passaged at confluence. For experiments, cells were harvested from confluent cell cultures, counted using the hemocytometer, and suspended in (10^6 cells/ ml) growth media. The cells (50,000/50 µl) were introduced to each electrode chamber, and visually inspected to insure cell attachment onto the electrode. After 0.5 h, an additional 150 µl of cell culture medium was added to the electrode chamber to support cell viability for the duration of the bioimpedance study.

3.2.4. Viability Tests

To assess cell viability, calcein AM (5 µg/mL) (BD Biosciences, CA, USA) and propidium iodide (10 µg/mL) (Sigma Aldrich, MO, USA) were added at the completion of each experiment. Fluorescence images of the cells were taken using the Zeiss Axio Imager and the % viability of cells on the electrodes was determined after counting the number of green (live) and red (dead) cells in five fields encompassing on all four electrodes.

3.2.5. Confocal and Scanning Electron Microscope (SEM) Images

The chips used for confocal and SEM imaging were diced into segments containing one electrode each and were cleaned in acetone and Nano-Strip® before use. These chips (1 cm X 1 cm) were fixed to the bottom of wells in 12-well plates (Falcon^{TM}, Corning, NY USA) using silicone high vacuum grease (976V, DOW Corning, MI, USA). Cell suspensions (10^5 cells/0.5 ml culture medium) were introduced into each well. Cells were cultured for 20 h. Then, the chips were processed for cell imaging after removing the culture medium and washing briefly twice with Hank's Balanced Salt Solution.

For confocal imaging, cells were fixed in 3% paraformaldehyde for 10 min. The actin cytoskeleton was stained with phalloidin conjugated with green fluorescence protein (GFP) (Invitrogen) and nuclei were counterstained with Hoescht33342 (Invitrogen) using our standard immunofluorescence staining protocol [136]. For SEM imaging, cells were fixed on the chips with 3% paraformaldehyde, dehydrated and SEM images were captured using a Carl Zeiss EVO40 Scanning Electron Microscope.

3.2.6. Bioimpedance Measurements

Individual devices (**Figure 3.1(B-d)**) were fixed inside 35 mm^2 cell culture dishes using double side tape and electrically connected to the measurement setup through wires soldered onto the bond pads. The measurement setup has been described in detail elsewhere [96]. In these experiments, measurements were made on two devices simultaneously to increase the throughput of the system and to examine the variability in the bioimpedance measurements between electrodes within the same device (intra-device) and between devices (inter-device). A LabVIEW program provided the user-interface to the measurement setup and was used to perform a frequency sweep (with 130 points in the range 1 kHz – 1 MHz) on each electrode using the impedance analyzer (Agilent HP4192A) and store the measured impedance magnitude ($|\mathbf{Z}|$) and phase angle ($\angle\mathbf{Z}$) values in a spreadsheet.

Here, $\mathbf{Z(f,t)}$ refers to the collection of complex impedance values over the frequency range at time 't' while $|\mathbf{Z(f,t)}|$ and $\angle\mathbf{Z(f,t)}$ refer, respectively, to the collection of magnitude and phase angle values of the impedance over the specified frequency range. First, to obtain a baseline or control measurement, the impedance of the cell culture medium was measured ($\mathbf{Z_{no\text{-}cell}(f)}$). Then, the cells were introduced onto the electrodes and the impedance ($\mathbf{Z_{cell}(f,t)}$) was recorded continuously to yield a measurement every 0.5 h on each electrode. The data from all the spreadsheets were

analyzed using a MATLAB® program. These analyses yielded the collection of normalized bioimpedance values over the frequency range (denoted by $\mathbf{Z_{norm}(f,t)}$) and calculated using the formula in equation 1 (see Figure 2(B)).

$$Z_{norm}(f,t) = \frac{Z_{cell}(f,t) - Z_{no-cell}(f)}{Z_{no-cell}(f)} \quad (1)$$

In **Figure 2.2(A)**, the bioimpedance magnitude and phase angle values recorded in the presence of cells were higher in the middle frequency range. Hence, 10-100 kHz is a useful frequency range for cellular analyses. We also noted that the normalized bioimpedance attributable to the presence of cells over the frequency range at any time 't', exhibited a maximum value or peak value at a specific frequency, and we assigned the name "*peak frequency"* ($\mathbf{f_{peak}(t)}$) (**Figure 2.2(B)**) to this value. The values of magnitude and phase angle of the impedance corresponding to this peak frequency are denoted by $\mathbf{|Z_{peak}(t)|}$ and $\mathbf{\angle Z_{peak}(t)}$, respectively (**Figure 2.2(A)**).

3.2.7. Statistical Tests

All statistical tests were performed using GraphPad Prism version 5.00 for Windows (GraphPad Software, CA, USA). The specific statistical tests performed for each experiment are indicated in results. One-way ANOVA with a Bonferroni's multiple comparison post hoc test was used to test for significant differences in the bioimpedance parameters among TNBC cell lines.

3.3. Results

3.3.1. Cell Behavior on Silicon and Pyrex/Glass Substrates

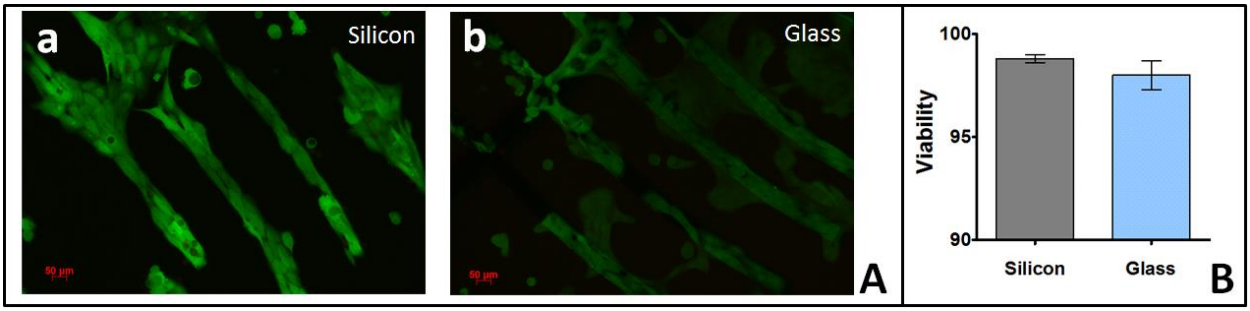

Figure 3.2 (A) Fluorescence images showing the green stain of adherent viable MCF-10A cells on the electrodes on silicon (A-a) and pyrex/glass (A-b). (B) The viability of cells (±SD) on silicon and glass/pyrex substrates.

Figure 3.2(A) compares images of calcein AM/propidium iodide (Live/Dead Cell Assay) stained MCF-10A cells adherent on a microelectrode affixed to a silicon substrate (a) and pyrex/glass substrate (b) after t=24 h. The electrode coverage is similar in both cases. The viability of the cells on both silicon and pyrex/glass substrates was very high, 98.8±0.2% and 98.0±0.7%,

respectively (**Figure 3.2(B)**). These results suggested that both substrates are suitable platforms for our electrodes.

We next compared the electrical performance of the silicon and the glass devices by collecting the bioimpedance spectra of the non-malignant MCF-10A breast cell line and the Hs578T metastatic breast cell line grown on each substrate for 8.5 h. The mean peak frequency (f_{peak}(t=8.5 h)) for both MCF-10A (64.6±5.9 from 27.0±1.5 kHz) and Hs578T (56.1±9.8 from 36.5±2.9 kHz) cells shifts to a higher value on the pyrex/glass device than the silicon device ($P<0.0001$). Based upon images shown in **Figure 3.2(A)**, this shift in peak frequency could be due to morphological differences in the cells on the two substrates, or reflect changes in cell-substrate attachments.

The inter-electrode variation (among electrodes in the same device) in the peak frequency values was less in the silicon devices (9.0%) in comparison to the pyrex/glass devices (14.6%). We also noted that the average inter-device variation in the peak frequency values was less in the silicon devices (16.5%) than in the pyrex/glass devices (35%) indicating that the silicon devices provide more reliable and reproducible bioimpedance information. Our results also indicated there was no significant difference in the mean peak frequency between MCF-10A and Hs578T cells on the pyrex/glass substrate ($P=0.47$). However, there were significant differences in the peak frequency values obtained from the electrodes on silicon ($P<0.05$). On the silicon substrate, the peak frequency for the non-tumorigenic MCF-10A cells was 27±1 kHz that was shifted to a significantly higher peak frequency of 36.5±5.3 kHz for the tumorigenic Hs578T cell line. Because this shift to a higher peak frequency in the tumorigenic line did not occur when electrodes were present on glass/pyrex substrates, there may be biological advantages to the use of silicon wafer substrates.

3.3.2. Bioimpedance parameters in triple negative breast cancer

Bioimpedance parameters exhibit time dependent patterns that are reflective of cell adhesion and spreading on the electrodes. The bioimpedance changes were compared among the TNBC cells during a 24 h time course (**Figure 3.3(A-C)**). The cells were counted, suspended in 50 µl of cell culture medium and introduced into the chamber housing the electrodes. After 0.5 h (see ⬆ in **Figure 3.3(A-C)**), there were sharp transitions in the parameters due only from the addition of 150 µl of cell culture medium to sustain growth and viability of cells in the chamber. The changes in the peak frequency, peak impedance magnitude and peak phase angle are shown **Figure 3.3(A-C)**. The fluctuations seen in the first 5 h of impedance measurements can be attributed to the initial

cell contact and attachment to the electrodes. Subsequently, the cells spread and adhere on the electrodes and the impedance measurements recorded can provide valuable insight into the nature of cell-electrode interactions and cell-cell junctions as shown here. From the time course changes of the bioimpedance parameters in **Figure 3.3(A-C)**, it is clear that after about t=10 h, the cell cultures are stable and there exist differences between cells types in our TNBC model. Each cell line was analyzed in four independent devices with four electrodes per device. For time points t>10 h, a peak frequency f>100 kHz was indicative of poor cell attachment and five such electrodes were excluded from analyses. This determination was verified by visual inspection of the fluorescence images obtained from the cells stained with calcein AM/propidium iodide (live/dead) assay to quantify cell viability at the end of each experiment.

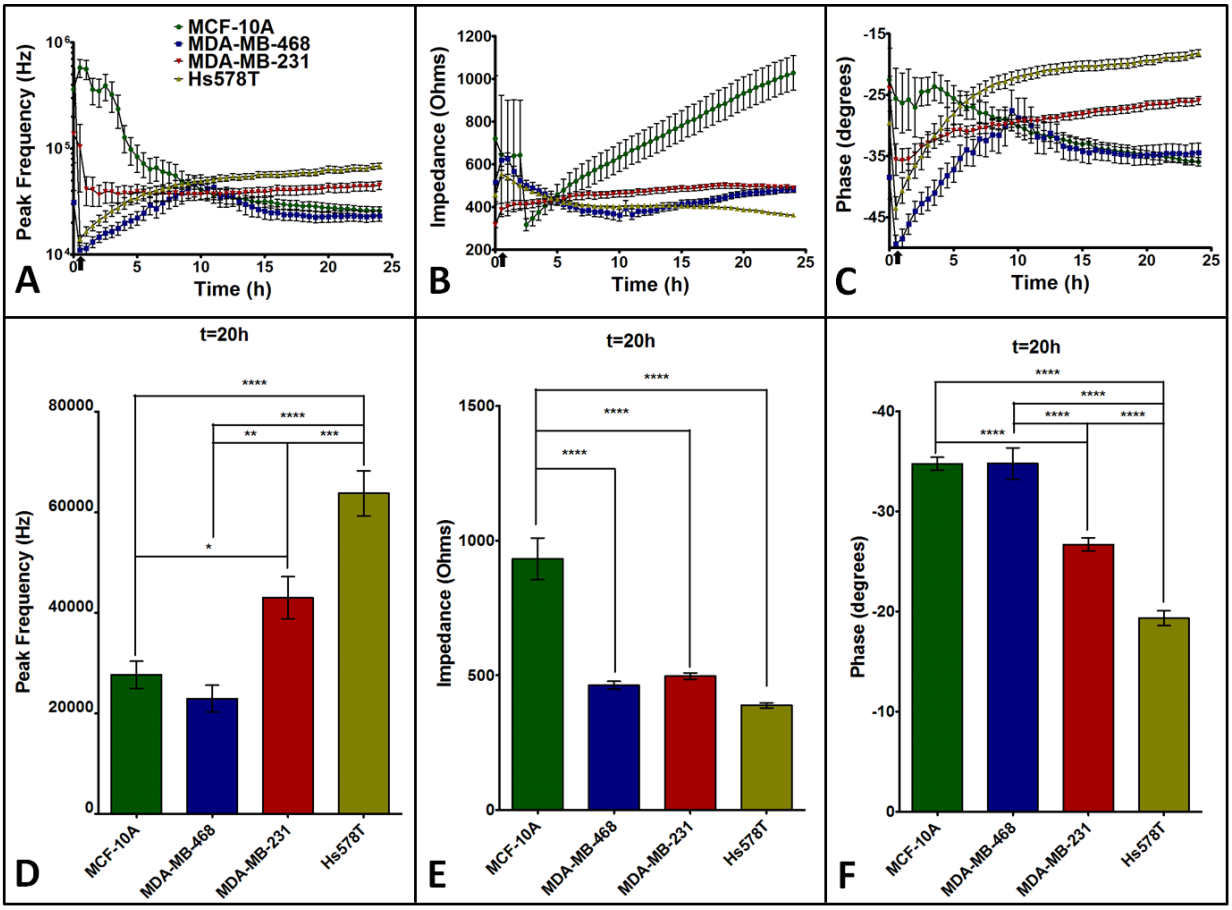

Figure 3.3 Time course of changes in (A) peak frequency (fpeak), (B) peak impedance magnitude (|Zpeak|) and (C) peak phase angle (∠Zpeak) during the initial 24 h after cell seeding. (D) Peak frequency (fpeak(t=20 h)), (E) Peak impedance magnitude (|Zpeak(t=20 h)|) and (F) Peak phase angle($\angle Z_{peak}$(t=20 h)) of the cell lines at the t=20 h time point. Data shown are mean values obtained from N=4 devices and error bars indicate SEM. *P<0.05, **P<0.01, *** P<0.001 and **** P<0.0001

Figure 3.3(A) shows the time course of the peak frequency for the four cell types where the steady-state values are visibly higher for the claudin-low cell types (MDA-MB-231 and Hs578T) than the basal cells (MDA-MB-468 and MCF-10A). We chose the time point t=20 h to analyze statistically significant differences in peak frequency values between the different cells as it is representative of cells well attached to the electrodes. The average peak frequency (f_{peak}(t=20 h)) in the basal lines were significantly lower than that of the claudin-low cells (see **Figure 3.3(D)**). Since lower values of peak frequency are associated with better cell attachment to the substrate and lower cell-substrate gaps [137], we infer that the basal cell monolayers interact and contact with the substrate more than the claudin-low cells.

The data in **Figure 3.3(B)** indicated the non-tumorigenic MCF-10A cells were readily distinguished from the TNBC lines by a markedly higher peak impedance magnitude for time points beginning at t=10 h. Statistical analysis revealed that the peak magnitude ($|Z_{peak}$(t=20 h)|) is significantly higher in the MCF-10A cells than in the metastatic TNBC cell lines ($P<0.0001$) (see **Figure 3.3(E)**). The non-tumorigenic MCF-10A cells exhibited a striking, continuously increased rate (positive slope) in their peak impedance magnitude over time as seen in **Figure 3.3(B)**; in contrast, the magnitude of the peak impedance in the TNBC cell models showed very little variation. Thus, the slope of the peak impedance magnitude provides one potential marker to distinguish normal breast epithelial cells from TNBC.

In **Figure 3.3(C)**, it is evident that the values of peak phase angle for the two basal cell lines, MCF-10A and MDA-MB-468 were very close (around -35 degrees) beginning from the t=15 h time point through the remainder of the 24 h time course. In contrast, the phase angle in the two claudin-low cell types shifted consistently towards lesser values of -20 to -30 degrees over the same time span. This distinctive pattern of phase angle changes was evident in these two sub-groups as early as t=15 h at a statistically significant level ($P <0.05$). The peak phase angle ($\angle Z_{peak}$(t=20 h)) values for all the cell lines significantly differed from each other except the MCF-10A and the MDA-MB-468 cells ($P=0.937$). Importantly, the basal subtypes (MCF-10A, MDA-MB-468) are distinguished from the claudin-low subtypes by a significantly smaller peak phase angle value (see **Figure 3.3(F)**). Claudin-low cells characteristically have a fibroblastoid shape and form loose cell-cell junctions [62, 131, 132]. We observed that the peak frequencies in claudin-low cell lines were higher than those for the basal cells. Correspondingly, the peak phase angle

observed for the claudin-low cells was also larger. This impedance profile might be useful as an indicator of the claudin-low subtype of TNBC. In contrast, we observed lower peak frequency and peak phase angle values in the basal cell lines which are characterized by their cuboidal shape and the presence of cell-cell junctions [119, 135].

3.3.3. Circuit Model of Bioimpedance

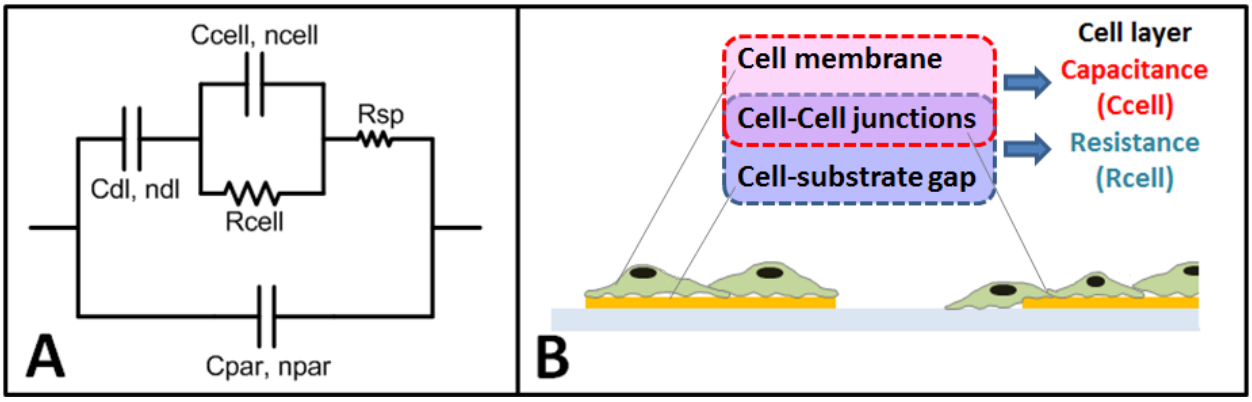

Figure 3.4 (A) Electrical circuit to model bioimpedance of a cell layer. (B) Illustration showing the physical variables that correlate with the circuit components in (A).

Circuit Element	Significance
Cdl	Double layer capacitance at the interface of electrode and culture medium
Rsp	Spreading resistance
Cpar	Parasitic capacitance
Ccell	Capacitance of cell monolayer adherent on electrode
Rcell	Resistance of cell monolayer arising from cell-substrate gap and cell-cell junctions

Table 3.2 Table of circuit parameters.

The electrical circuit (**Figure 3.4(A)**) used to model bioimpedance signals obtained from adherent cells on planar microelectrodes is well known and has been reported by researchers extensively including us [19, 82, 96, 137, 138]. **Figure 3.4(B)** is an illustration that highlights the physical attributes giving rise to the electrical parameters shown in the circuit. The circuit model for measurements from the medium is the Randle's circuit which consists of the double layer capacitance (Qdl, ndl) in series with the spreading resistance (Rsp) which are both in parallel with the parasitic capacitance (Qpar, npar). The impedance of the cells is presented in the model as an

R||C block which is in series with Qdl and Rsp and represents the capacitance (Qell, ncell) and the resistance (Rcell) of the cell layer. These parameters are summarized in **Table 3.2**. All capacitances in the circuit are modeled as constant phase elements. First, the impedance measured from the cell culture medium is fit using the parameters Qdl, ndl, Rsp, Qpar and npar. The cell parameters (Qcell, ncell and Rcell) were then obtained by keeping the corresponding parameters obtained from the medium on each electrode constant. The true value of capacitance was calculated as $Ccell=(Qcell*Rcell)^{-n}/Rcell$.

Cell Type	**Ccell (nF)**		**Rcell (Ω)**	
	Mean	SEM	Mean	SEM
MDA-MB-231	22.4	0.08	75.47	21.37
Hs578T	16.32	1.207	68.31	16.63
MDA-MB-468	5.69	0.68	289.58	21.65
MCF-10A	7.50	2.31	803.92	115.36

Table 3.3 Cell parameters obtained from electrical circuit model.

The average values obtained from n=8 electrodes in N=2 devices for each cell type are summarized in **Table 3.3**. The MCF-10A cells have highest values of peak impedance magnitude among the four cell lines which is attributed to Rcell in the model. Resistance of the MCF-10A cells obtained from the model was almost 3 times that of the MDA-MB-468 cells and more than 10 times that of the claudin-low cell lines. It can be noted that the claudin-low cell types (MDA-MB-231 and Hs578T) cells have higher values of capacitance and lower resistance values when compared to the basal cell lines. The peak frequency corresponds to the highest value of normalized impedance and hence, the maximum impedance of the R||C block (when $R=1/(\omega C)$) due to the cells. The product (R×C) of resistance and capacitance obtained from the model is lower in the claudin-low cell lines. This is consistent with the observation that claudin-low cell lines exhibit higher values of peak frequency and hence, higher phase angle. In contrast, the basal MDA-MB-468 and MCF-10A cells are morphologically characterized by tight cell-cell junctions as seen in the confocal images (**Figure 3.5(A)**) [139]. These cell lines show higher values of resistance from the model, and these observations are consistent with their characteristic low peak frequency and lower values of peak phase. These results suggest that the inability to form cell-cell junctions

in the claudin-low subtype might play a role in the higher measured peak frequency and peak phase angle values, and provide a rationale for further investigation and development of bioimpedance phase angle as a biomarker of claudin-low TNBC.

3.3.4. Morphometry of TNBC cells on electrodes

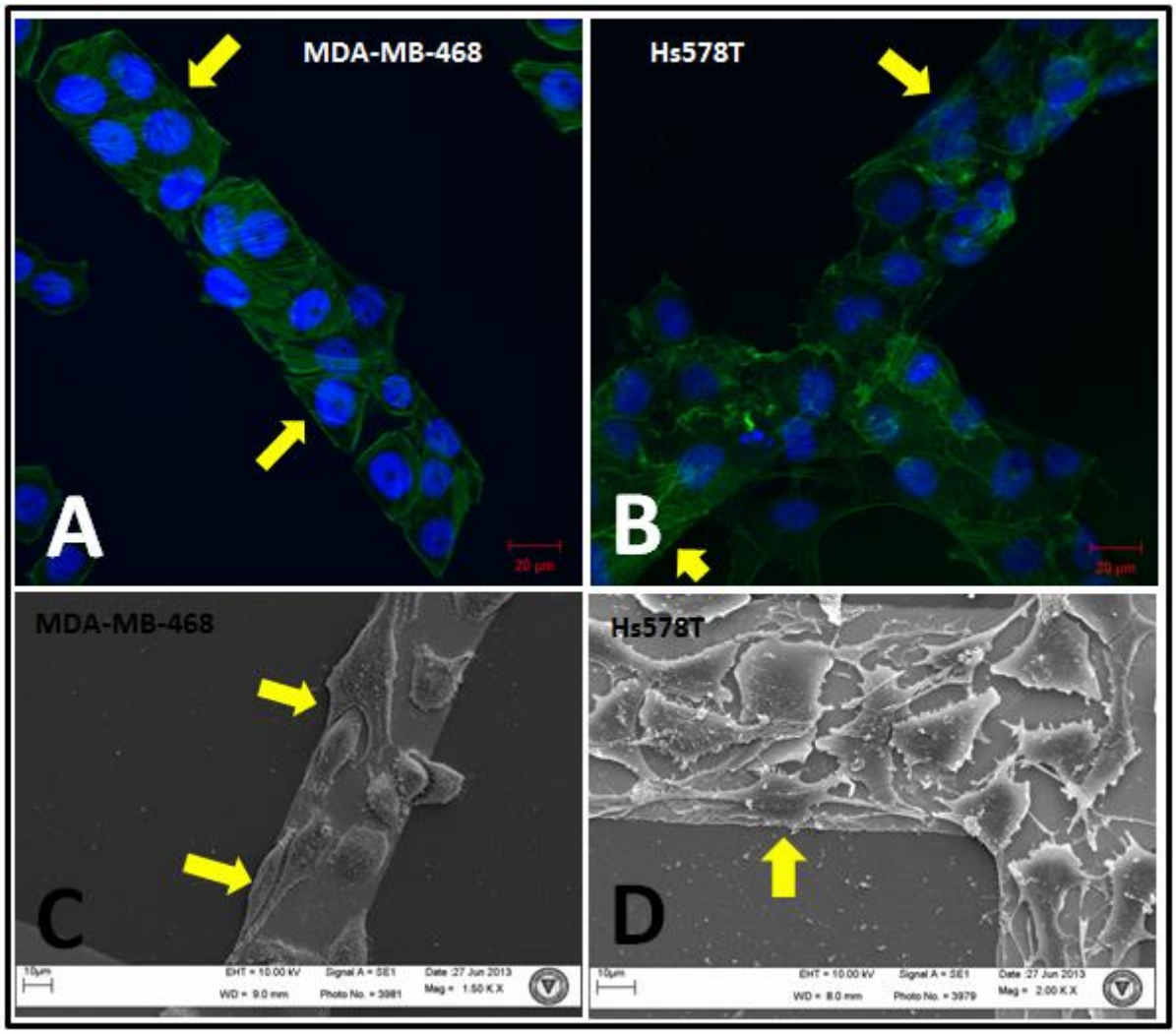

Figure 3.5 (A, B) Confocal images showing MDA-MB-468 and Hs578T cells on the electrode where the actin cytoskeleton and nuclei have been stained green and blue respectively. (C, D) SEM images of the MDA-MB-468 and Hs578T cells attached to the electrode.

To quantitatively determine the electrode coverage, cells were plated onto electrode areas delineated by cloning cylinders. After 20 h, cells were stained with Propidium iodide, Calcein AM and Hoechst 33342 and fluorescence images were obtained. Cell numbers attached to the electrode were counted using the blue Hoechst-nuclei. The electrode area and mean cell area (n=10) were obtained from each field using ImageJ. The electrode coverage was calculated as the ratio of mean

cell area multiplied by number of cells on the electrode and the area of the electrode. The mean±SEM values for percent electrode coverage were 90±3% for MCF-10A, 89±3% for MDA-MB-468, 92±3% for MDA-MB-231 and 91±4% for Hs578T cells. Hence, the cell coverage of the electrodes was equivalent for all the cell lines tested and differences in the bioimpedance parameters are likely attributable to intrinsic differences in cells' properties.

The morphology of cells on the electrodes supports the idea that there are differences in cell-cell junction formation in MDA-MB-468 (low bioimpedance phase angle value) and Hs578T (high bioimpedance phase angle value). In **Figure 3.5(A)** the confocal image illustrates the cuboidal shape of the MDA-MB-468 cells; the cell-cell junctions between neighboring cells are highlighted by the presence of cortical actin. The Hs578T cells adhere to the electrodes in a less organized pattern (**Figure *3.5***(B) and **Figure 3.5(D)**).

Interestingly, the actin fibers are well organized and brighter along the boundary of the electrodes, as shown by the yellow arrows in **Figure 3.5(A and B)**, which indicates that there is a higher concentration of actin in these regions. The presence of highly ordered actin fibers in larger numbers along the edges of the electrodes suggests that cell attachment and spreading can be controlled and directed using electrode geometry. This is also verified in the SEM image of the MDA-MB-468 cells on the electrode, as shown in **Figure 3.5(C)**, where the yellow arrows highlight cell spreading along the electrode boundary.

3.4. Discussion

Breast cancer is a leading cause of cancer death in women worldwide [140]. Population-based screening and early treatment have reduced, but not eliminated the impact of this disease. A major focus in breast cancer research today is the use of personalized medicine to improve patient outcomes. Personalized medicine relies on sophisticated genetic and biochemical screens to match a patient's tumor subtype with prognostic indicators that will allow optimization of treatment regimens [141, 142]. As an example of personalized medicine, approximately 15-20% of all patients are diagnosed with TNBC (as compared with hormone receptor positive tumors), and these TNBC patients experience shorter overall survival times, shorter disease free survival times, and more rapid appearance of visceral metastases than patients with other receptor positive types of breast cancer [117, 118, 142].

Although TNBC are identified by a lack of hormone receptors, a failing in current management of TNBC is the absence of biomarkers indicative of TNBC subtypes [129]. The claudin-low subtype addressed in this study, is now known to possess cancer stem cell properties, preferentially metastasize to the lung and brain, and respond better to chemotherapy with doxorubicin than docetaxel [62, 112, 120, 122-125]. The work presented here suggests that sensors measuring the bioimpedance phase angle is a potential new avenue for identifying this important subtype of TNBC.

The biological properties of claudin-low breast cells are consistent with the use of bioimpedance parameters as biomarkers. First, normal mammary epithelial cells function in cell layers joined by tight junctions, and formation of tight junctions are known to result in a rise in transepithelial electrical resistance [131, 132, 135, 143]. Claudin proteins play a critical role in this process by aligning cells and recruiting a third protein, occludin to the junctional complex [119, 144, 145]. Second, the claudin-low breast cells also lack robust expression of cell-cell adhesion proteins E-cadherin and P-cadherin [121, 132, 143], and as a result, there is a large paracellular contribution to the impedance signal. In contrast, the basal subtype of TNBC expresses claudins. The MDA-MB-468 basal cell type example used for this work, adopt cuboidal morphology that is associated with cell-cell adhesion similar to that seen in normal MCF-10A (**Figure 3.5(A)**). Confocal and SEM images of the cells on the electrodes exhibit their preferential spreading along the electrode boundary which suggests that the electrode geometry could be crucial to the sensitivity of the bioimpedance sensor to biologically relevant changes in the cell.

While most bioimpedance studies examine the parameters at a fixed frequency, we looked at the peak frequency which is the characteristic frequency at which the maximum in the normalized bioimpedance magnitude occurs. This value of peak frequency varies as a function of time and thus carries significance in the variations of bioimpedance due to biologically significant alterations in the cell cultures such as a decrease in the cell substrate gap which would result in a simultaneous rise in the value of the peak normalized impedance magnitude as well as a decrease in the peak frequency [137]. The peak bioimpedance magnitude of the non-tumorigenic MCF-10A cells was significantly higher than the metastatic cell lines tested. The peak frequency and peak phase angle were significantly higher in the claudin-low molecular subtype (MDA-MB-231, HS578T) of TNBC and associated with their cell morphology marked by the general absence of cell-cell junctions.

We also compared the sensing properties of the electrodes on silicon and pyrex/glass substrates. The viability of the cells on both silicon and pyrex/glass substrates was >98% making both substrates suitable for cell culture. The variations in the peak frequency values obtained within each device and between devices were lower in silicon devices. The electrodes are deposited on a silicon dioxide passivation layer which is chemically equivalent to pyrex/glass. However, since the oxide layer is thermally grown from silicon by an oxidation method, it is a higher quality oxide than the pyrex/glass substrate which has considerable amounts of boric oxide, sodium oxide and potassium oxide which are introduced during productions of the wafers. Possibly, the use of a higher quality glass substrate such as quartz would reduce the variations in the impedance measurements, enabling use of the sensor electrodes on the more optically preferred substrate. In addition, future work will address the role of electrode geometry in improving sensitivity of bioimpedance measurements and extend bioimpedance testing to a larger panel of TNBC lines to investigate phase angle as a biomarker of the claudin-low subtype.

3.5. Conclusion

Impedance spectroscopy in a test panel of TNBC cells was studied to identify potential electrical markers of the claudin-low subtype of TNBC. Basal and claudin-low molecular subtypes of TNBC were distinguishable through the bioimpedance parameters peak frequency and peak phase angle. Basal cells exhibited significantly lower values of peak frequency and peak phase angle than claudin-low cells. Since ECIS-based bioimpedance measurements are highly sensitive to cell-substrate and cell-cell junctions, the distinctions in peak frequency and peak phase angle identified in basal cells might be attributed to their typical cuboidal cell morphology and cell-cell junctions, which are uncharacteristic of claudin-low cells. This study provides the first exploration of bioimpedance sensing for recognition and classification of the clinically important claudin-low subtype of TNBC. In addition, peak impedance measures distinguished normal breast cells from TNBC. Peak impedance magnitudes and their rate of change over time were significantly lower in all three TNBC cell lines compared to the normal basal MCF-10A cells.

4. A comparative study of nano-scale coatings on gold electrodes for bioimpedance studies of breast cancer cells

This chapter was reproduced from [111] with permission from Springer.

Srinivasaraghavan V, Strobl J, Wang D, Heflin JR, Agah M. A comparative study of nano-scale coatings on gold electrodes for bioimpedance studies of breast cancer cells. Biomedical microdevices. 2014:1-8.

4.1. Introduction

Bioimpedance is the complex electrical resistance of a biologically important substance. Bioimpedance measurements are increasingly being used in biomedical applications and cell research [32, 35, 146, 147]. The ease of bioimpedance measurements is a significant advantage. The technique is very rapid and requires no sample preparation, reagent costs are low, and is readily adaptable for use in high throughput devices. Bioimpedance measurements enable samples to be monitored continuously in real-time in a label-free and non-destructive fashion. Furthermore, the information content of bioimpedance is high due to the nature of the measurable electrical properties. Impedance spectroscopy is sufficiently sensitive to monitor DNA hybridization reactions; gold electrodes functionalized with a specific oligonucleotide were used to sense interactions with target DNA [47]. Another important application of electrochemical sensing is in the measurement of medically important metabolites. Glucose monitoring has been widely studied [51]. Similarly, serum urea and creatinine concentrations are measured using electrochemical sensors that respond to pH changes in the solution [52]. Miniaturization of bioimpedance sensing platforms is simple because the presence of only two or more electrodes is needed and these are easily integrated with emerging microelectromechanical systems (MEMS) and microfluidic devices [38, 148, 149].

Electric cell-substrate impedance sensing (ECIS) is the term given to a specific type of bioimpedance measurement that is specifically applicable to measuring the impedance of adherent living cells on planar microelectrodes [110]. ECIS has all the inherent advantages of bioimpedance measurements and a broad range of applications. In the last decade, ECIS has gained momentum as a valuable tool in cancer related studies [21, 75, 150]. Researchers have demonstrated its use in monitoring cell adhesion, proliferation, motility and cytotoxicity [16, 17]. In our laboratory, uniquely designed ECIS electrodes were used to detect rare metastatic breast cancer cells in a

background of normal breast and fibroblast cells by monitoring the bioimpedance response to the histone deacetylase inhibitor suberoylanilide hydroxamic acid [82]. The present work is motivated by the desire to improve the sensitivity of these electrodes to detect breast cancer cells.

Here the use of nano-scale coatings as a strategy to further sensitize ECIS electrodes to bioimpedance measurements from breast cancer cells is explored. This strategy is based on two major findings. First, surface topography can be used to specifically guide the adhesion and spreading of biological cells [151, 152]. These topographies can also be tuned to control differentiation of stem cells into different lineages [153, 154]. We predict that introducing nano-scale roughness on the surface of electrodes will help guide the cells onto the electrodes. Second, the sensitivity of neuronal recordings from implantable microelectrodes was improved using gold nanoparticle and carbon nanotube coatings [53, 55, 57]. In another study, glassy carbon electrodes were coated with polyaniline nanotube membranes and gold nanoparticles and the resulting electrode showed enhanced sensitivity for DNA detection [155]. Coatings consisting of nanocomposites of carbon nanotubes have also been shown to improve sensitivity of electrochemical sensors [58, 156, 157]. The improved sensitivity of the electrodes in these studies was attributed to increased surface roughness and interaction or an enhanced selectivity to the target analyte. These examples provide the rationale for investigation of coatings to modulate the sensitivity of ECIS electrodes to impedance of breast cancer cells. In this work, we use coatings of gold nanoparticles (AuNP), carbon nanotubes (CNT) and electroplated gold (EPDC) to introduce nano-scale roughness on the surface of the gold electrodes and show that the sensitivity of planar gold microelectrodes can be modulated through the use of electrode coatings. To demonstrate this, first, the fabrication of these electrodes and their coating using the layer-by-layer (LbL) method and electroplating is presented. Next, the three different nano-scale coatings along with a control (no coating), were tested with various solutions to identify the coating most sensitive to changes in conductivity. Finally, we introduced MDA-MB-231 metastatic breast cells on the same electrodes and performed a similar analysis to find the coating most sensitive to bioimpedance measurements obtained from adherent human breast cancer cells. Thus, a comparison between the control, AuNP, CNT and EPDC coatings, on the same electrode design and fabricated on the same platform is presented here and their sensitivity is investigated with respect to two specific applications, namely solution conductivity and ECIS, The results presented in this paper show promise for the use of nano-scale coated electrodes for various applications

including the detection of metabolites in human fluid samples such as urine, plasma and blood and cellular drug responses.

4.2. Materials and Methods

4.2.1. Fabrication

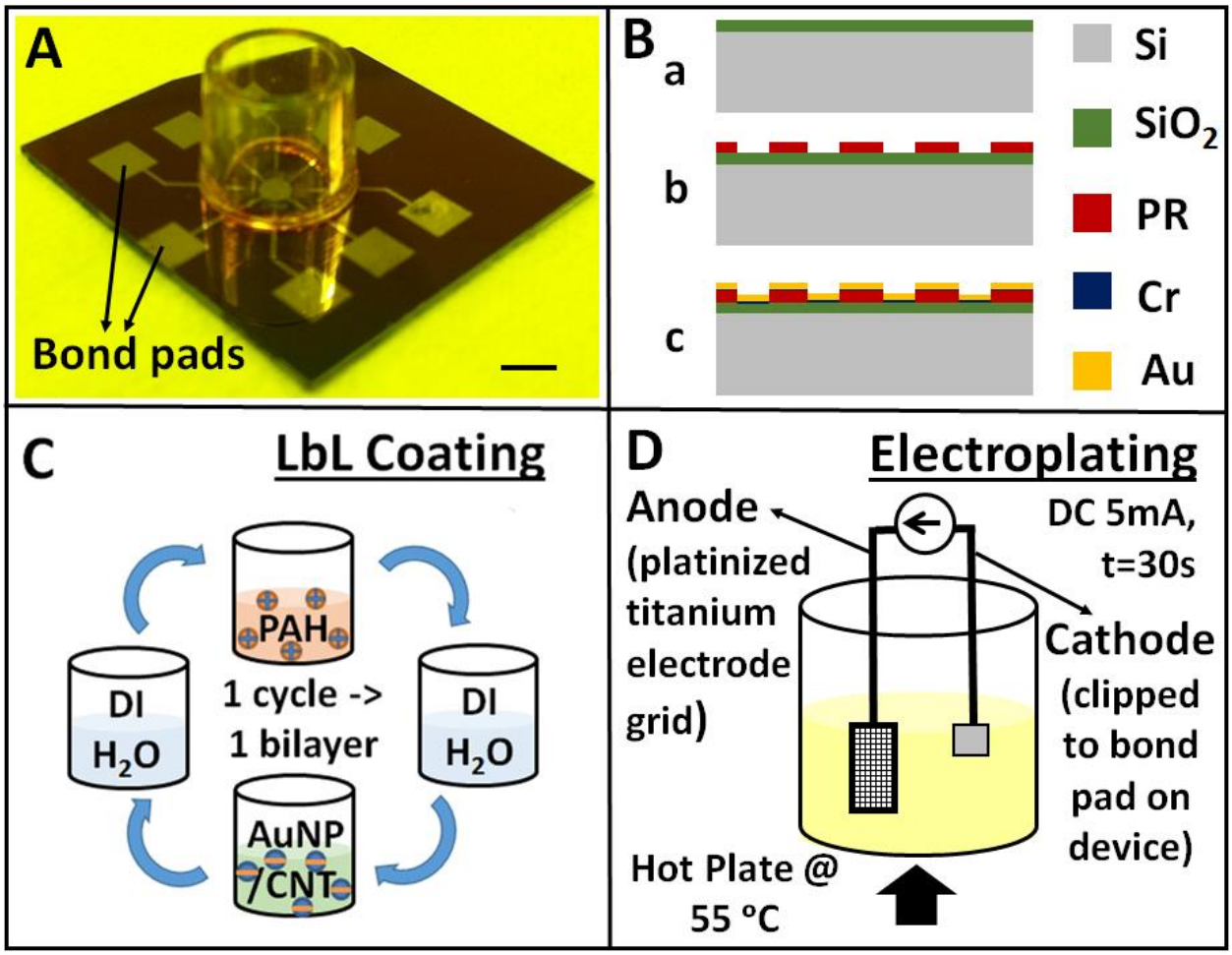

Figure 4.1 (A) Photograph of the packaged bioimpedance sensor (Scale bar=3 mm), (B) Process flow for the fabrication of the devices, (C) Process showing layer-by-layer (LbL) coating of the devices with AuNP and CNT and (D) Setup for electroplating the devices.

The electrode design and fabrication follow our previously published methods [82, 96] and is shown in **Figure 4.1(A,B)**. Briefly, the silicon wafers were passivated with a layer of thermal oxide (~500 µm) for electrical insulation (**Figure 4.1(B-a)**). A positive photoresist was spun on the wafer and the electrode pattern was transferred on to it using photolithography (**Figure 4.1(B-b)**). A thin layer of chromium/ gold (Cr/Au) which is 25 nm/ 100 nm was deposited on the patterned wafer using e-beam evaporation (**Figure 4.1(B-c)**). The devices were then diced and a lift-off process in

acetone was used to obtain the patterned gold electrodes. For the electroplated (EPDC) electrodes, each of the patterned gold electrodes after lift-off was electroplated separately in gold electroplating solution (TG-25 RTU, Technic, Inc.) heated to 55 °C, using 5 mA of direct current for 30 s. The setup for electroplating is shown in **Figure 4.1(D)**. The devices were dipped in methanol for 2 min prior to electroplating to wet the surface. The gold electroplating solution was stirred using a magnetic stir bar at 300r/min to distribute the gold ions uniformly in solution. After electroplating, the devices were washed in methanol and deionized (DI) water and then washed again in acetone and DI water before being used for experiments.

For the gold nanoparticle (AuNP) and carbon nanotube (CNT) coatings, the devices were diced and the coatings were deposited using a layer-by-layer (LbL) method as described below. The LbL self-assembly technique was developed to fabricate dense and homogeneous thin layer coatings consisting of two materials with opposite electric charge through utilization of Coulombic attraction [158]. The surface charge of a nano-scale layer of one material on the substrate will attract the second material with opposite charge. The adsorption of the second material results in reversal of the surface charge, and the steps are repeated by alternately dipping the substrate into the solutions/suspensions of these two materials. Thus, layer-by-layer coatings consisting of these two materials (two adjacent layers are called a bilayer) can be fabricated conveniently with good coating homogeneity and thickness control. The thin film coatings fabricated by the LbL technique have been applied in the electromechanical actuators [159], chemical and biological sensors [160], optical [161] and electrochromic devices [162]. Recently, our group used the LbL technique to selectively coat nanoparticle layers inside the micro fabricated structures of silicon for micro gas chromatography applications [163].

In this study, we used a similar approach to selectively coat gold nanoparticles (AuNP, average diameter 3.2 nm, concentration 20 ppm, Purest Colloids Inc.) and water soluble single walled carbon nano-tubes (CNT), functionalized with m-polyaminobenzene sulfonic acid (PABS, Carbon Solutions Inc.) on the gold electrode via the LbL technique where the AuNP and CNT are both negatively charged. The polycation used was poly(allylamine hydrochloride) (PAH, Sigma-Aldrich), which is a long chain inert polymer and serves as an "adhesive" between every two AuNP or CNT layers holding them together. The AuNP colloid was used as received and the CNT was dissolved in de-ionized (DI) water to a concentration of 0.1 mg/ml and then was sonicated for 2 h to produce a dispersion. The pH of the CNT solution was adjusted to 8.0 (±0.1). The PAH was

made into 10 mM solution and its pH was adjusted to 4.0 (±0.1). The process of LbL coating is summarized in **Figure 4.1(C)**. Briefly, the devices were immersed alternatively in PAH and AuNP/CNT solutions for 2.5 min each. They were also washed thrice in DI water for 30s each time in between each coating layer. Overall, it took approximately 1 h to coat a device with 5 bilayers of AuNP or CNT.

The devices (before lift-off) were coated with AuNP (30 bilayers) or CNT (50 bilayers) using the LbL method. Then, the photoresist was removed using lift-off in acetone along with the coatings on top of it, leaving the coating only on the electrode, as shown in **Figure 4.2 (B, C, F and G)**.

4.2.2. Experiments

The bioimpedance measurement setup has been described in detail in our previously published work [96]. A frequency log sweep (comprising 30 points in the range 1 kHz – 1 MHz) was done individually on each electrode using the impedance analyzer (Agilent HP4192A). The measured impedance magnitude (|Z|) and phase (∠Z) values for each electrode was stored in a separate spreadsheet for each sweep.

Electrode sensitivity was measured in biological solutions of varying conductivities using DI water as the control. A phosphate buffered saline (PBS) series of concentrations 0.1X, 1X and 10X, dielectrophoresis buffer (DEP buffer) and cell culture medium were compared. DEP buffer consists of 8.5 g of sucrose and 0.725 ml of RPMI in 100 ml DI water. The cell culture medium consists of 88 ml Dulbecco's Modified Eagle Medium (DMEM): Ham's F-12 (1:1) (Lonza) with 10 ml fetal bovine serum (10%), 1 ml penicillin-streptomycin (100 U/ml) and 1 ml L-glutamine (30 mg/ml). The conductivities of the solutions were measured using a hand-held conductivity meter. DI water had the lowest conductivity at 3.09 µS/cm. The conductivities of 0.1X, 1X and 10X PBS were 3.3 mS/cm, 29.4 mS/cm and 209 mS/cm, respectively. DEP buffer and cell culture medium had measured conductivities of 210 µS/cm and 24.7 mS/cm, respectively. Impedance measurements were made by introducing 200 µl of solution into the electrode chamber and performing a frequency sweep across all electrodes every 8 minutes. Impedance data were continuously recorded for 48 min to collect 6 sequential measurements on every electrode for each solution. The electrodes were washed twice using DI water between runs. The impedance of DI water was measured again after the salt solutions and between the DEP buffer and cell culture

medium runs to test the reproducibility of the data and ensure that the DI water washes between measurements removed any traces of previous solutions.

Next, the MDA-MB-231 human breast cancer line (ATCC) was introduced onto the same electrodes. MDA-MB-231 cells were harvested from confluent cell cultures, suspended in growth medium (10^6 cells/ mL), and 50 µl of the cell suspension (50,000 cells) were introduced into each electrode chamber; after 0.5 h to facilitate cell attachment onto the electrodes, an additional 150 µL of cell culture medium was added to maintain cell viability during experiments. Impedance data were recorded continuously for 24 h and yielded 180 measurements. The magnitude and phase of impedance obtained from the MDA-MB-231 cell culture at any time point 't' and frequency 'f' is denoted by $|Z_{cell}(f,t)|$ and $\angle Z_{cell}(f,t)$, respectively. The impedance obtained from the cell culture medium at each frequency point 'f' was set as $Z_{no\text{-}cell}(f)$. The normalized impedance magnitude and phase at any time point 't' and frequency 'f' are denoted by $|Z_{norm}(f,t)|$ and $\angle Z_{norm}(f,t)$ respectively and are calculated using the formulae shown in equations (1) and (2).

$$|Z_{norm}(f,t)| = \frac{|Z_{cell}(f,t)| - |Z_{no-cell}(f)|}{|Z_{no-cell}(f)|} \qquad (1)$$

$$\angle Z_{norm}(f,t) = \frac{\angle Z_{cell}(f,t) - \angle Z_{no-cell}(f)}{\angle Z_{no-cell}(f)} \qquad (2)$$

The normalized impedance magnitude of cells over the frequency range at any time 't' has a maximum value or peak value that we call the **normalized peak impedance** and occurs at a specific frequency to which we assign the name **peak frequency** ($f_{peak}(t)$). The value of normalized impedance phase corresponding to the $f_{peak}(t)$ was called the **normalized peak phase**.

4.2.3. Statistical Tests

The statistical tests reported were performed using GraphPad Prism version 5.00 for Windows (GraphPad Software, CA, USA). Results were considered statistically significant when $P<0.001$

4.3. Results and Discussion

Figure 4.2 shows optical images of the electrodes (A-D) and scanning electron microscope (SEM) images of the surface of the nano-scale coatings on the electrodes (E-H). The control electrodes (**Figure 4.2(A)**) are uncoated and consist only of the evaporated Cr/Au layer. The SEM image (**Figure 4.2(E)**) shows that the surface of the control electrode is highly uniform and smooth. The AuNP, CNT and EPDC nano-scale coatings introduce varying degrees of roughness on the surface of the electrode as can be seen in **Figure 4.2(F, G and H)**. The AuNP coating (**Figure 4.2 (F)**) is relatively uniform due to the size of the gold nanoparticles used for the coating

(~3.2 nm) but is not as smooth as the evaporated gold surface. The optical image of the CNT coating on the electrode shown in **Figure 4.2(C)** shows that the coverage is non-uniform and some regions on the electrode have a thicker coating than others. This is also seen in the SEM image (**Figure 4.2(G)**) where accumulations of CNTs are seen near the edges of the image. The SEM image shows the CNT fibers range in width between 19-25 nm and produce a web-like surface structure interspersed with pores whose diameters range from a few nanometers to as large as 80 nm. The EPDC coating consists of particles with jagged edges and has the largest sized particles (100-400 nm) of all the coatings that were tested in this study as is seen in the SEM image in **Figure 4.2(H)**. It is to be noted that the size of the breast cancer cells used in our experiments was about 30 µm when spread on the electrode [82].

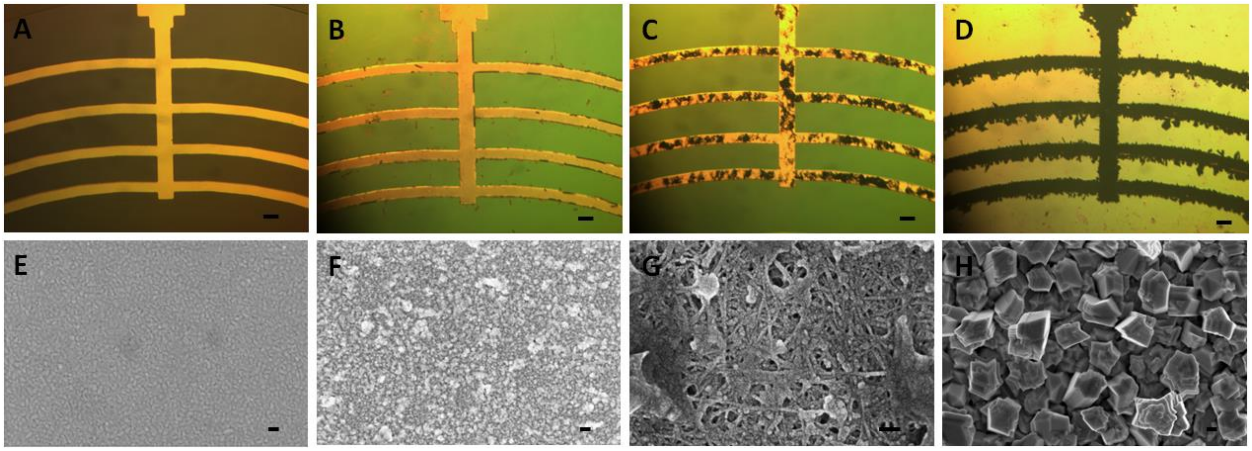

Figure 4.2 Optical (A-D) and scanning electron microscope (E-H) images of the uncoated (Control - A, E), gold nanoparticle coated (AuNP - B, F), carbon nanotube coated (CNT - C, G) and DC electroplated (EPDC - D, H) electrode. Scale bar in optical images and SEM images are 50 µm and 100 nm respectively.

Figure 4.3 summarizes the impedance data obtained from cell culture medium (A), DEP buffer (B), DI water (C), PBS 0.1X (D), PBS 1X (E) and PBS 10X (F) on the control, AuNP, CNT and EPDC electrodes from 8 electrodes in 2 devices. The impedance measured in the low conductivity solutions, namely DI water and DEP buffer, was essentially identical on the control, AuNP, CNT and EPDC electrodes (**Figure 4.3(B, C)**). This observation reflects the very low concentration of solutes. At these conductivities, the ionic reaction at the electrode-solution interface is not limited by the available surface area of the electrode, but rather, the rare interaction between solute and electrode. The frequency spectra of the impedance magnitude were distinguishable for each nano-scale electrode coating in the biological solutions with higher, more physiologically relevant conductivities. In particular, between frequencies of 1-50 kHz, the

impedance magnitude tended to be greater when measured with the smoother electrode surfaces, namely, the control gold electrode and the AuNP coated electrode than with the rougher surfaced electrodes (CNT, EPDC). This trend was observed in all the solutions with conductivities in the mS/cm range. As expected, the frequency spectra of the impedance magnitude of the two commonly used physiological solutions, cell culture medium (24.7 mS/cm) and PBS 1X (29.4 mS/cm) were closely matched as were their conductivities.

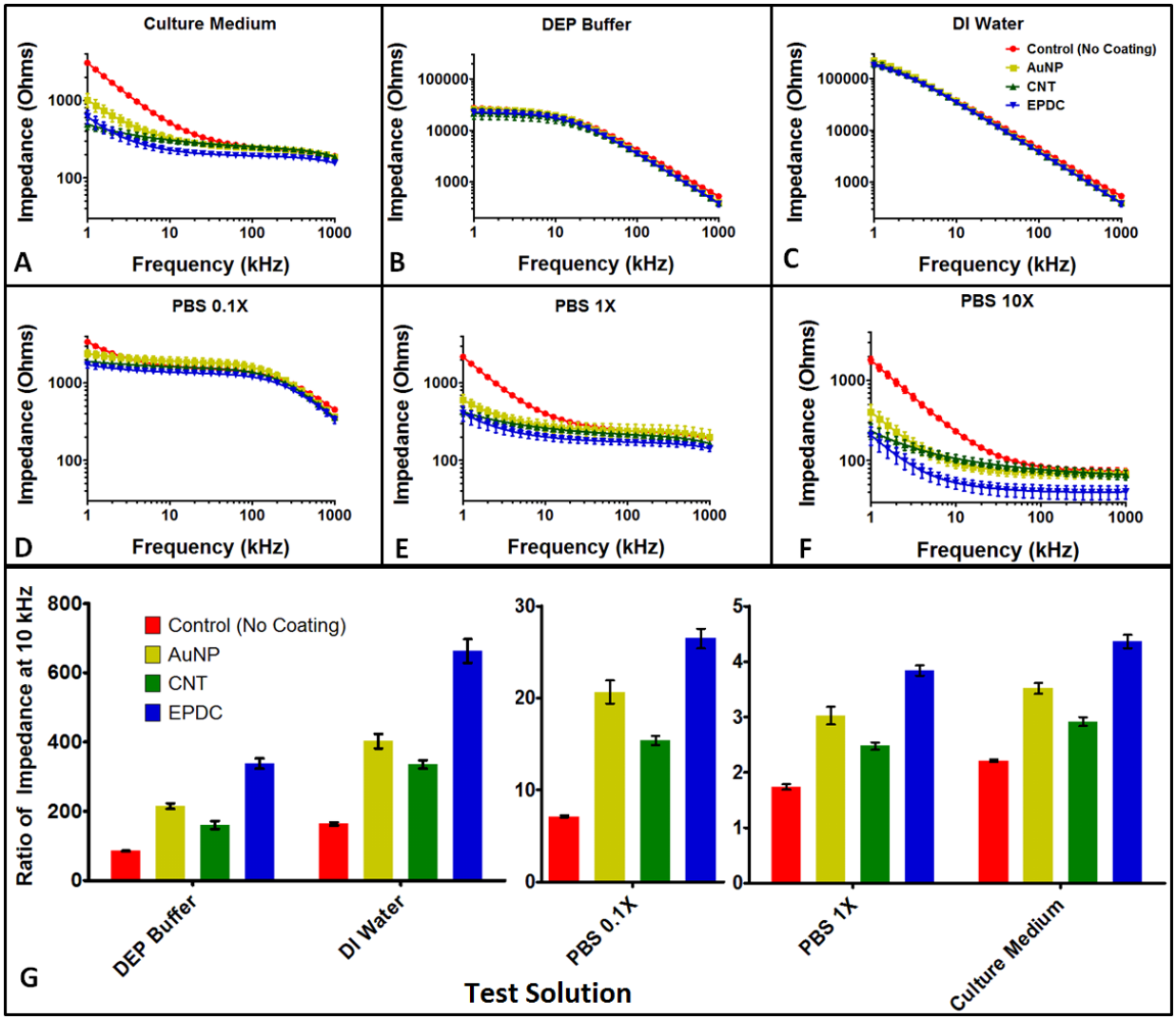

Figure 4.3 (A-F) The impedance of solutions with varying conductivities on the electrodes with nano-scale coatings over the frequency range 1 kHz – 1 MHz from n=8 electrodes in N=2 devices. Mean values are plotted and error bars indicate SEM. (G) The ratio of impedance at 10 kHz for each solution with respect to PBS 10X on coated and uncoated electrode.

To identify the electrode nano-scale topography providing the highest sensitivity to conductivity differences in biological solutions, the mean ± SEM of the percent changes in the measured impedances for the cell culture medium, PBS 1X and PBS 0.1X from that of PBS 10X

was computed for each electrode type. This analysis was performed across the entire bioimpedance spectra. A one-way analysis of variance (ANOVA) with a Bonferroni's multiple comparison post hoc test revealed that the percent changes in impedance in EPDC electrodes was significantly higher than other electrodes tested ($P<0.001$). **Figure 4.3(G)** shows the ratio of impedance values at 10 kHz of all the solutions tested with respect to PBS 10X. PBS 10X was chosen because this solution had the highest conductivity as well as the lowest impedance values on all the electrode types. A comparison of the coated electrodes with the uncoated (control) electrodes reveals that the EPDC electrodes showed higher changes in impedance for the same changes in solution conductivity consistently across all solutions tested. The figure shows the comparison only at 10 kHz but this trend was observed across all frequencies tested. Thus, the EPDC electrodes were found to be most sensitive to changes in the conductivity of the test solution.

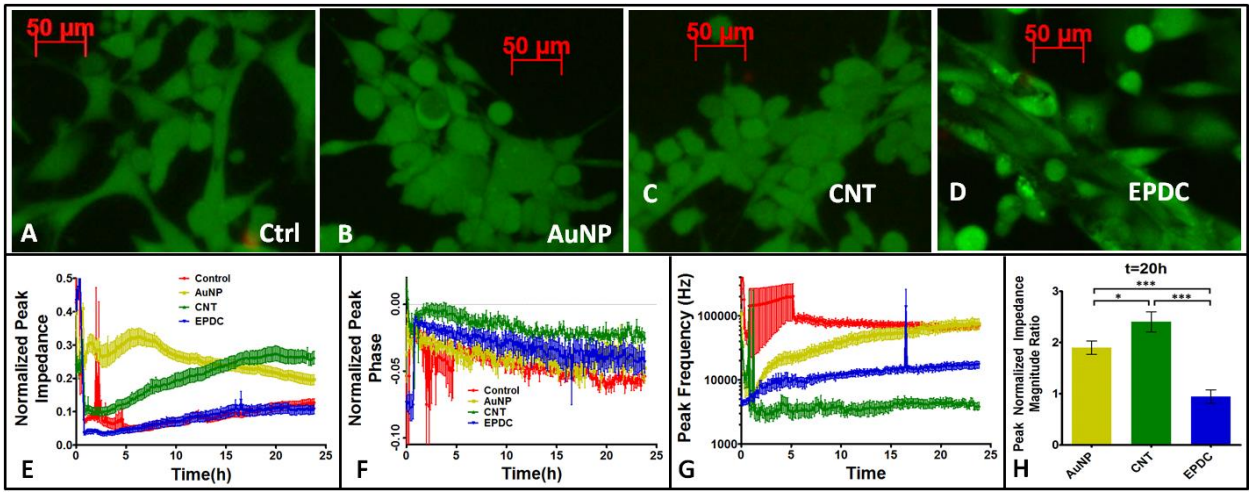

Figure 4.4 (A-D) Fluorescence images of the MDA-MB-231 cells on the electrodes. Normalized peak magnitude (E), normalized peak phase (F) and peak frequency (G) of the impedance of MDA-MB-231 cells on the control, AuNP, CNT and EPDC electrodes in 24 h after cell seeding. (H) The ratio of normalized peak impedance magnitude at t=20 h AuNP, CNT and EPDC coated electrodes with respect to the uncoated (control) electrodes. Data shown is from n=8 electrodes in N=2 devices. Mean values are plotted and error bars indicate SEM.

MDA-MB-231 cell suspensions in culture medium were seeded onto the same 8 electrodes in the 2 devices that were used to test the impedance of the biological solutions. Fluorescence images of the MDA-MB-231 cells stained with calcein AM (**Figure 4.4(A-D)**) show that the cells exhibit a more stretched morphology on the control and EPDC electrodes and are more rounded with more cell-cell contacts on the AuNP and CNT electrodes. The bioimpedance spectra of the cancer cells were analyzed on each electrode, and the mean and SEM values are summarized in **Figure 4.4(E-G)**. The small variation between electrodes and devices as revealed in the SEM values plotted

indicates the devices are very reliable. The nano-scale coatings on the electrodes elicit differential effects on the electrical properties of the cancer cells: normalized peak impedance magnitude (**Figure 4.4(E)**), normalized peak phase (**Figure 4.4(F)**) and peak frequency (**Figure 4.4(G)**).

The initial stage of cell adhesion to the electrodes occurs during time ($t<5$ h) and this is followed by a sustained stage of electrode attachment ($t \geq 5$ h-24 h). During the initial stage, values of all three measured electrical parameters showed some random variability. During the sustained stage, several electrode-specific patterns of emerged.

The magnitude of the normalized peak impedance (**Figure 4.4(E)**) is a well-accepted index of the nature of the cell-electrode interaction. Based on the magnitude of the bioimpedance, there is initially a somewhat stronger level of cancer cell adhesion to the AuNP nano-coated electrodes compared with the other electrode surfaces. However, electrical measurements from the AuNP-coated electrodes displayed certain anomalies during the sustained stage making AuNP-coated electrodes impractical for monitoring sustained electrical properties in the cancer cells. The underlying cause for these shifts is not certain, however, AuNP are readily taken up by cancer cells, raising the possibility that physical interactions between the cancer cells and the 3.2 nm AuNP are involved [164].

In contrast, cell adhesion is initially weaker to the other three electrode types compared to the AuNP-coated electrodes, but cell adhesion gradually strengthens during the entire sustained stage as monitored by the rise in bioimpedance magnitude (**Figure 4.4(E)**). This is particularly evident in the case of the CNT nanostructures. Structural similarities between the nano-scale web-like patterns created by the CNT on the gold electrodes and the electrospun collagen networks produced as simulated extracellular matrix for tissue engineering might foster the strong adhesion to the CNT-modified gold electrodes [165]. We observed that the CNT electrodes have the maximum normalized values for both peak impedance and peak frequency. A one-way ANOVA with Bonferroni's multiple comparison post hoc test confirmed that the CNT electrodes showed significantly higher changes in both peak normalized impedance ($P<0.001$) and peak normalized phase ($P<0.001$) in the presence of MDA-MB-231 cells. **Figure 4.4(H)** shows the ratio of the normalized peak impedance magnitude at t=20 h on the AuNP, CNT and EPDC electrodes with respect to the control electrodes. The figure clearly shows that the impedance change in response to metastatic breast cancer cells is maximal on the CNT coated electrodes followed by the AuNP

electrodes. Also, the EPDC electrode response is not significantly different from that of the control electrodes in the presence of breast cancer cells.

The most interesting finding of this study was the distribution of the average peak frequency (t>10 h) of the MDA-MB-231 cells on the control (79.7±7.4 kHz), CNT (3.8±0.9 kHz) and EPDC (20.1±3.9 kHz) electrodes over the frequency spectrum (**Figure 4.4(G)**). It should also be noted that the peak frequency values for each electrode coating are stable after t=10 h with less than 25% variation thereafter. The shift in peak frequency from control gold electrodes was significant on both electrode coatings and was greatest on the CNT electrodes. The fluorescence images in **Figure 4.4(A, C, D)** show cell morphology changes occur in response to these coatings, and this might be a factor in the bioimpedance frequency shift. This is the first demonstration that electrode coatings can be used to modulate the peak bioimpedance frequency of a cell, and opens a new avenue of research in engineering nanocomposite electrode coatings as a means to detect different types of cells based upon their impedance spectra. Further research will be directed towards investigation of the sensitivity of these coated electrodes to normal and other types of cancerous breast cells as well as the exploration of additional nanocomposite coatings.

4.4. Conclusion

Thus, planar gold microelectrodes were successfully coated with AuNP and CNT using a layer-by-layer deposition method as well as electroplated gold to create nano-scale roughness on the surface of the electrodes. The nano-scale coatings resulted in improved sensitivity of these electrodes but the type of coating that was most sensitive differed for the two applications tested. Experiments on the impedance of biologically relevant solutions with varying conductivities revealed that the EPDC electrodes displayed the highest sensitivity to changes in conductivity. The changes in the impedance due to the adherence of metastatic breast cells were most significant on the CNT-coated electrodes. We showed that nano-scale coatings can shift the frequency dependent sensitivity of the electrodes and suggest that such coatings might therefore be applied to resolution of the bioimpedance spectra of cancer from non-cancerous cells. Further studies on coatings with ordered nano-scale features could further enhance the sensitivity to the cells.

5. A high-throughput, reconfigurable electrode array for bioimpedance spectroscopy

5.1. Introduction

Bioimpedance refers to the opposition offered by biological samples such as bacteria, mammalian cells and tissues to the flow of electric current. Researchers have exploited this technique to monitor a variety of effects in the human body such as the flow of blood [166, 167], body composition such as water and fat [168, 169], and various tumors in the body [72, 74, 100, 170]. Studying cells at single-cell levels or in small populations expands our understanding of the fundamental electrical properties of these units that contribute to changes in larger scale tissue measurements [19, 22, 49, 63, 77, 92]. Electric Cell-substrate Impedance Sensing (ECIS) is a technique that serves this objective, where the impedance of adherent cell cultures is monitored using an electrode pair consisting of a small sensing or working electrode and a large counter or reference electrode [24, 85, 110]. Similar measurements have also been made with interdigitated electrode pairs which have two identical electrodes in a comb structure [116, 171].

Bioimpedance measurements can provide multi-parametric information such as impedance magnitude and phase angle as a function of excitation voltage and frequency. Since the impedance measured from adherent cell monolayers is sensitive to variations in cell attachment to the electrodes, some applications include cell growth and proliferation, motility measurements, cell-extracellular matrix interactions, electroporation, wound healing assays, migrations assays, cell toxicity studies, and drug response studies [22, 25, 67, 70, 172-174]. Commercial systems employing this technology have been successful in developing standardized multi-well platforms which are advantageous due to their simplicity, uniformity and ability to do high-throughput screening but only provide limited flexibility when used for research. For instance, one system only allows measurements at a pre-programmed list of excitation frequencies and offers limited flexibility in electrode design. Another system only provides a standardized measurement index limiting the extent of data acquisition. Hence, although these systems are useful in investigating initial feasibility, they do not necessarily provide the best platform to develop and hone technology for specific applications.

As many research reports have established previously, the design of the electrodes and their physical characteristics can influence their sensitivity [111, 138, 146]. Additionally, the same

electrode configuration may not exhibit the best sensitivity for different applications. Thus, there exists a research opportunity to tailor bioimpedance technology to achieve greatest sensitivity for each application which is currently limited by the capabilities of commercial and user-configured systems. Here, we present a new bioimpedance measurement platform with reconfigurable elements that can be used towards this objective.

In the past, our group has reported a device with four electrodes capable of making impedance measurements from *in vitro* cell populations [83, 84, 96]. With the 4-electrode sensor, we have shown the selective detection of breast cancer cells using the histone deacetylase inhibitor vorinostat and the improvement of electrode sensitivity using nano-scale coatings [82, 111]. However, the 4-electrode design places limitations on the experimental possibilities. In biological experiments, especially those evaluating the effect of stimuli, both physical and chemical, on samples such as drug effects, a number of conditions need to be tested in concert with appropriate controls to evaluate effect. In addition, biological samples such as cells are often sensitive to environmental conditions such as temperature, humidity and evaporation of culture medium in the incubator. Thus, there is a need for a platform that is capable of making bioimpedance measurements from a large number of samples or samples under different conditions; either physical, chemical or biological.

To address these needs, we designed a wafer-level impedance array with 36 electrodes in the prototype (expandable to 48 electrodes in future designs) and implemented a measurement system using off-the-shelf electronic instrumentation in combination with a custom fixture and automated measurement software. While commercially available systems offer multi-well impedance measurement devices, the uniqueness of our 36-electrode platform is that it is also reconfigurable to accommodate electrodes with physical differences in shape, design or surface and it can be fabricated on substrates of silicon and glass. We highlight this feature of our system by fabricating nine different electrode structures on a single impedance array device and systematically investigating the role of design parameters on electrode sensitivity to breast cancer cells. Additionally, the system offers flexibility at the software end with respect to measurement parameters such as excitation voltage, frequency and time interval between measurements. The configuration of the device and measurement system, its characterization and the demonstration of flexibility in our new bioimpedance platform are discussed in the following sections.

5.2. Materials and Methods

5.2.1. Design, fabrication and data analysis

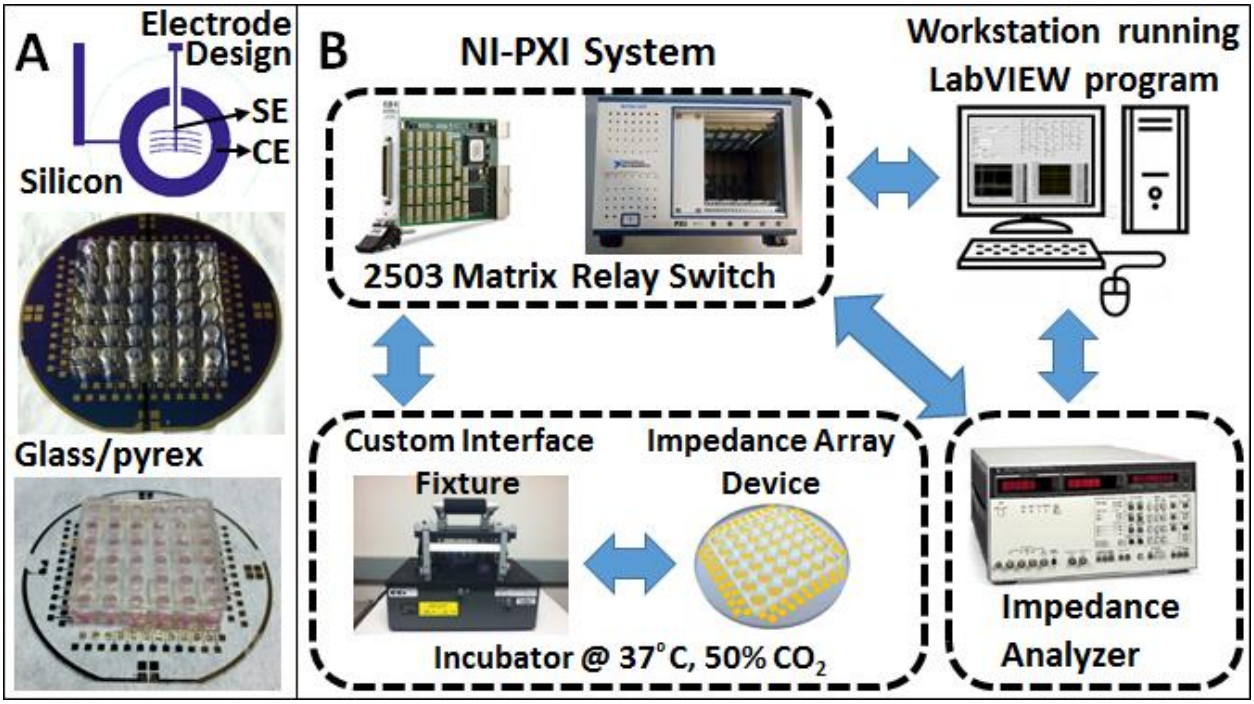

Figure 5.1 (A) Images of the fabricated bioimpedance array device on a silicon substrate (top) and glass/pyrex substrate (bottom). (B) The configuration of the automated measurement system implemented using an NI-PXI system, matrix relay switch cards, Agilent impedance analyzer and custom interface fixture controlled using a LabVIEW VI running on a workstation.

The wafer-level impedance array devices fabricated on both silicon and glass/pyrex substrates are shown in **Figure 5.1(A)**. Each impedance spectroscopy unit in the array consists of a sensing electrode (SE) and a counter electrode (CE). The electrodes are distributed on a 4 inch wafer as a 6X6 array with one electrode per well. The diameter of each well and the spacing between wells are set to 4.6 mm which makes commercially available multi-channel pipettes compatible for use with this device. The electrodes are connected via electrical lines to bond pads that are located along the periphery of the electrode array as seen in **Figure 5.1(A)** through which electrical connection to the measurement system can be made via the fixture.

To demonstrate flexibility, we designed and fabricated eight types of branched SE with distributed area having different widths ranging from 10 μm to 250 μm and spacing ranging from 25 μm to 100 μm. The branched electrode structure was chosen to achieve better electrode coverage in the sensing area. Their responses were compared to a lumped area electrode with a

500 μm square shape with the aim of identifying the geometry that can provide superior sensitivity to bioimpedance changes from breast cancer cells. We also designed the CE around the SE, unlike our previous devices, to allow for uniform distribution of cells on the SE and prevent any edge effect due to accumulation of cells from contributing to the measured bioimpedance. For characterization experiments, we used the branched electrode structure in the SE similar to our previously reported device to compare the measurements made from the new system with our previously reported results [82, 111]. The ratio of the surface areas of CE to that of SE for both devices was kept in the same range (10-15) to ensure that their sensitivities were comparable.

The device can be fabricated on a glass or an oxidized silicon substrate as electrical properties and the fabrication processes are similar. The fabrication of the electrodes follows our previously published methods [82, 111]. AZ9260 photoresist was spun coated on the wafer. Photolithography was used to transfer the pattern of the electrodes onto the photoresist. A 250 Å/1500 Å Cr/Au layer was then be deposited on the wafer using electron-beam evaporation. Lift-off in acetone was used to obtain the metal electrode pattern on the substrate. The PDMS layer is made by pouring PDMS pre-polymer mixed with curing agent in the ratio of 10:1 onto a silicon wafer and inserting an aluminum mold with cylindrical out of place features to form the wells. The setup is cured at 80 ˚C for 60 min to obtain the PDMS multi-well layer shown in **Figure 5.1(A)**. We also made a PDMS cover to seal the wells as seen in **Figure 5.1(A)** on the glass/pyrex device with out-of-plane cylindrical protrusions that go into the wells and provide a snug fit to minimize evaporation when covered. The device was cleaned with oxygen plasma for 10 min and 80 μl of collagen type IV (Sigma) solution in PBS (0.1 mg/ml) was introduced onto the electrodes immediately afterwards to coat them for 2 h at room temperature right before the start of the experiment. The collagen promotes cell attachment with the electrodes.

Figure 5.1(B) shows the electronic interface for the multi-well impedance array. The wafer level device is mounted on a custom made fixture from Circuit Check Inc. which makes the physical connections to the bond pads on the device via spring-loaded pins. The fixture has a mechanical system than can be released to open up the chamber for device loading purposes. It also has an opening from the top which can be used to gain access to the wells during experiments if required. The wafer-level device and the fixture are placed inside a humidified incubator maintained at 37 ˚C and 5% CO_2 to ensure proper growth conditions for the cells. The National Instruments PXI system was used as the multiplexing module and consists of a controller along

with two low voltage matrix relay switches (NI PXI-2503) which are used for switching between wells while making measurements from the fabricated devices. It is connected to a PCI Express board on the computer via a MXI link. The Agilent 4192A impedance analyzer is used to make the impedance measurements and is connected to the computer via a GPIB interface. It is also connected to the common terminal on both NI-PXI-2503 cards and configured to make two-wire impedance measurements. The fixture is also connected electrically to the terminal blocks of the matrix relay switches. A custom LabVIEW VI was developed to automate the process of switching between the electrodes, and to make and store impedance measurements in spreadsheets on the computer. It also provides the user interface to control specific measurement parameters including excitation voltage, frequency or frequencies, and the time interval between measurements. The results of impedance parameters from different wells are updated on-the-go and stored in excel sheets as designated by the user. The VI is configured to make measurements from all 36 wells at a single frequency point and cycle through all frequency points as specified by user. This ensures that measurements from all wells for any given frequency point are obtained within 60 s of each other and minimizes effects of any change in environmental conditions when comparing measurements among the 36 wells.

5.2.2. Cell culture

MDA-MB-231 cells were purchased from American Type Culture Collections (ATCC) and maintained in accordance with ATCC recommendations. The growth medium used was 10% fetal bovine serum (Atlanta Biologicals), 1% penicillin-streptomycin (100 U/ml) and the rest high glucose Dulbecco's Modified Eagle Medium (DMEM-HG from ATCC). The cell cultures were maintained in T-25 cm^2 flasks in a humidified incubator (37 ^oC, 5% CO_2) and passaged at confluence. For experiments, cells were harvested from confluent cell cultures, counted using the hemocytometer, and suspended in (10^5 cells/ ml) growth medium. The cells (8,000/80 μl) were introduced to each well. The viability of cells as evaluated using calcein AM was over 95% under the experimental conditions described here.

5.3. Results and Discussion

5.3.1. System Characterization

The performance of this new impedance array measurement system was compared with that of a previous generation device and which utilized a less sophisticated data acquisition system.

The 36-electrode impedance array has a total of 36 SE, each with its own CE located in a separate well or chamber with a capacity of 100 µl. In contrast, the previous 4-electrode sensor device had only four SE which were distributed radially around a shared CE and located in the same chamber having a capacity of 300 µl. The design of the SE and the ratio of the areas of SE and CE were kept the same in both devices to enable comparison of the system responses to a series of solutions varying in conductivity. The sensitivity of the new impedance array device to cell concentration changes was evaluated using two experimental protocols: 1) the initial cell concentrations in the wells was varied and 2) replicately plated numbers of cells were seeded onto each electrode, and cell numbers were increased by cell proliferation.

5.3.1.1. Effect of solution conductivity

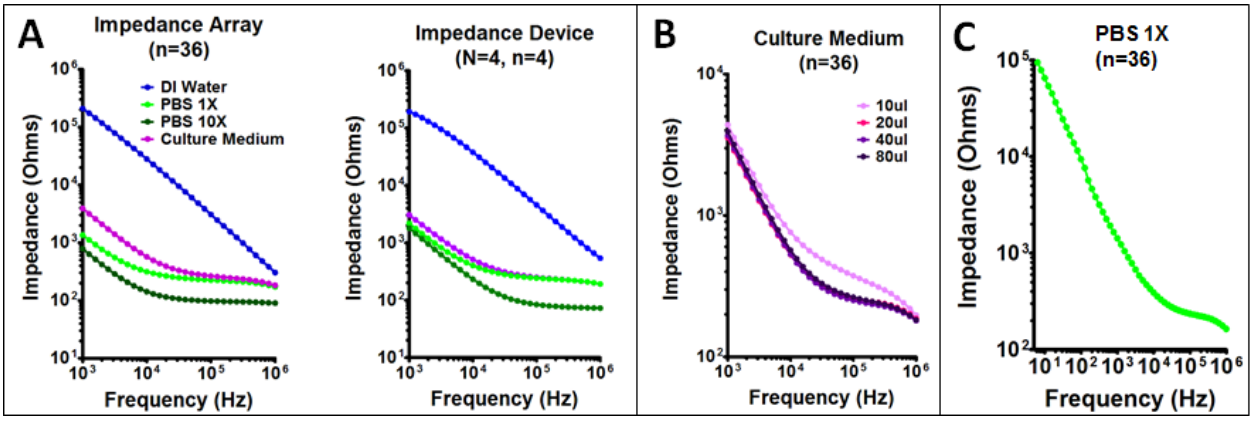

Figure 5.2 (A) Comparison of the impedance values (mean±SEM) measured using standard biological solutions over the 1 kHz-1 MHz frequency range on a single 36-electrode impedance array device (left) and four of our earlier generation 4-electrode sensor devices (right). (B) The impedance values (mean±SEM) measured from varying volumes of culture medium using the 36-electrode impedance array. (C) Impedance values (mean±SEM) of PBS 1X measured across the frequency spectrum (5Hz-1MHz) using the impedance array.

The impedance response from 80 µl of solutions of varying conductivities including deionized (DI) water, 1X and 10X phosphate buffered saline (PBS), and cell culture medium in the impedance array were recorded over 31 log-distributed frequency points in the range of 1 kHz to 1 MHz. The conductivities of the solutions determined using a hand-held conductivity meter were 3.09 µS/cm, 29.4 mS/cm, 209 mS/cm and 24.7 mS/cm for DI water, PBS 1X, PBS 10X and culture medium, respectively. The impedance magnitude over the entire frequency test range using the 36-electrode device (**Figure 5.2(A-left)**) was comparable with previously published results from our earlier generation 4-electrode sensor device (**Figure 5.2(A-right)**) [111]. It is to be noted that the

SE design and the surface area ratio of CE to SE are the same in both types of devices making the comparison permissible. In addition, the maximum percentage error in the measurements made from all the electrode pairs across the full range of impedance values from all the test solutions was 5.6% indicative of the high inter-electrode reliability of the new array impedance device. These results validated that the new 36-electrode scaled array system is capable of making equivalent impedance measurements as the 4-electrode version in the earlier generation design.

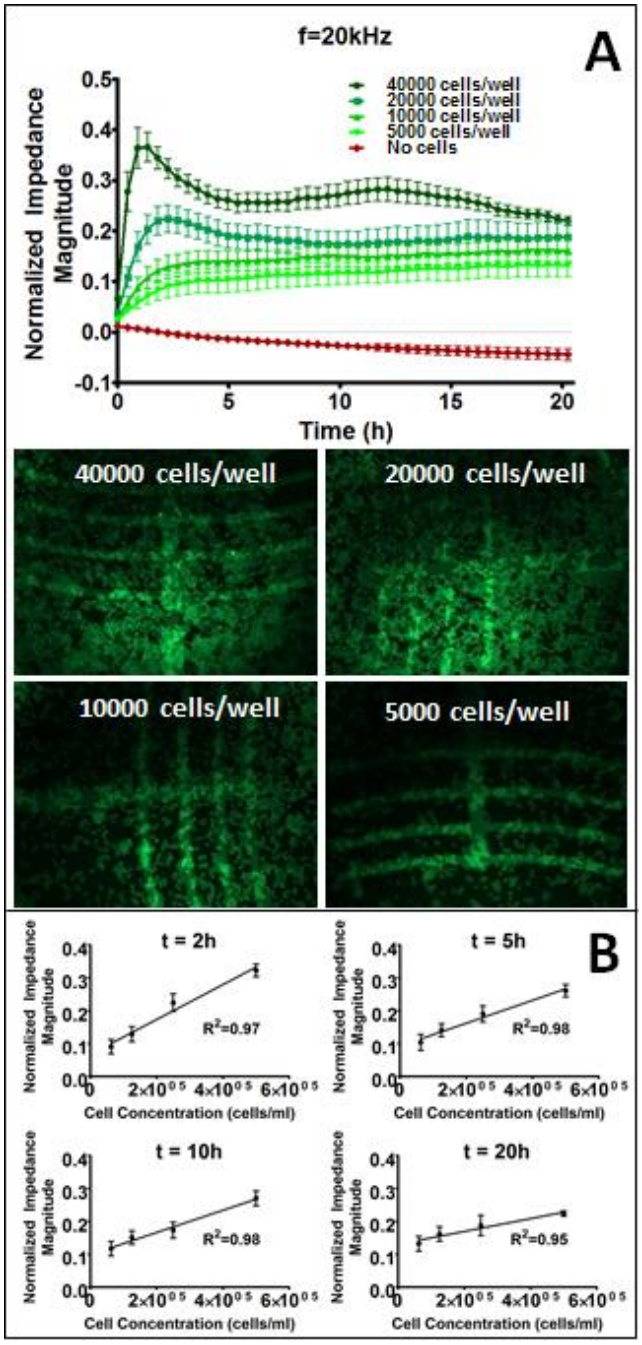

Figure 5.3 (A) The time course of the normalized impedance magnitude (mean±SEM) of varying concentrations of cells (top) and images of MDA-MB-231 cells on the electrodes in 36-electrode impedance array (bottom). (B) Linear regression analysis at four time points (2, 5, 10, 20 h).

The effect of varying the culture medium volume in the wells in the 36-electrode device was also evaluated with respect to impedance magnitude (**Figure 5.2(B)**). For volumes ranging between 20 µl and 80 µl, impedance values measured did not change significantly, however, when culture medium volume was reduced to 10 µl, impedance values deviated discernably. We define a working volume of at least 20 µl for the 36-electrode array device. This smaller working volume is advantageous for applications requiring rare and/or expensive reagents. In comparison, our earlier 4-electrode sensor and commercial systems require a working volume in the range of 100 to 200 µl. **Figure 5.2** shows the impedance of PBS1X measured in the frequency range 5 Hz-1

MHz. The impedance values display an increasing trend in the lower frequency spectrum as it is dominated by the double layer capacitance in this range and approach the DC value at 5 Hz.

5.3.1.2. Impedance magnitude as a sensitive indicator of cell concentration

The impedance array device was configured to measure the response from four different concentrations of MDA-MB-231 breast cancer cells with eight electrodes dedicated to each test concentration, 5000, 10000, 20000 and 40000 cells/well. Four electrodes served as no-cell controls. Impedance measurements were made continuously at 31 frequency points distributed logarithmically over the range of 1 kHz to 1 MHz with an excitation voltage of 50 mV for a duration of 20 h. **Figure 5.3(A)** is the plot of the time course of changes in Znorm for all the electrodes. Below this graph, selected images of electrode coverage by cells is displayed. Impedance is linearly related to the number of cells/well and **Figure 5.3(A)** shows how this impedance increases throughout the 20 h time course. **Figure 5.3(B)** shows the results from regression analysis for four different time points examined between 2 and 20 h. R^2 values ranged between 0.95 and 0.98 indicating strong linear relationship between cell number and normalized impedance.

5.3.1.3. Impedance monitoring of cell growth

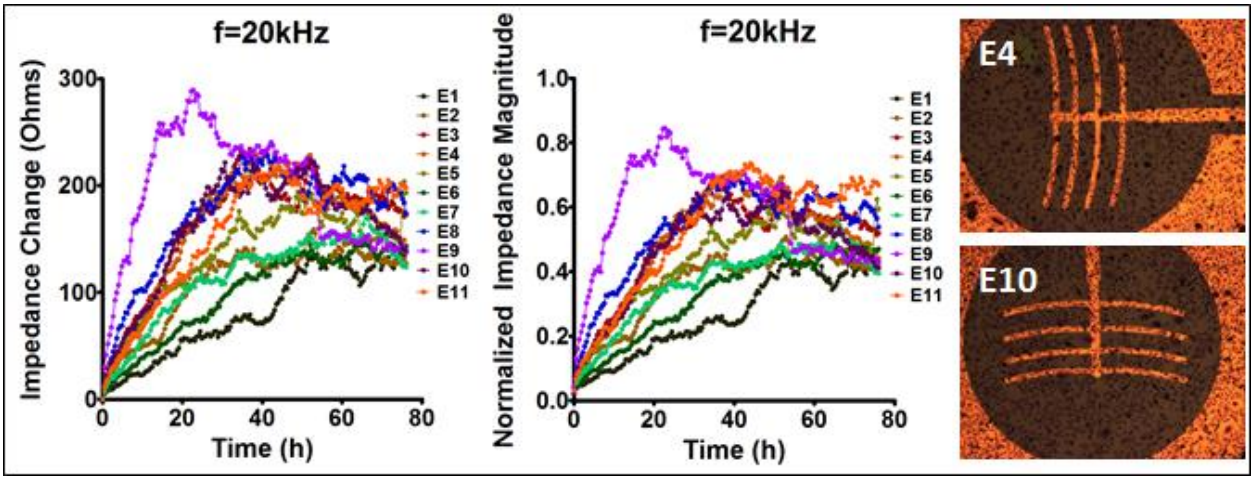

Figure 5.4 The time course of the impedance change with respect to t=0 (left) and normalized impedance magnitude with respect to impedance of cull culture medium (center) for n=11 electrodes capturing cell proliferation over three days. Images of crystal violet stained cells on the electrodes at the end point of the experiment (right).

MDA-MB-231cells were harvested from a 60% confluent culture and seeded 4000 cells/well. Impedance was monitored continuously over the 1 kHz- 1 MHz frequency range using an excitation voltage of 200 mV for 75 h. Figure 6 shows the impedance changes over a 3-day

time course using data from randomly selected electrodes on the full 36-electrode array. The impedance change (Zchange) was calculated by subtracting Z at each time point from Z at t=0 h (Zchange=Z(t)-Z(t=0h)). The increase in impedance over the first 40 h is consistent with a doubling in cell number and the doubling time of 24 h for MDA-MB-231 cells. After this time, there is saturation of the impedance values which corresponds to attainment of a confluent monolayer of cells covering the electrodes (**Figure 5.4**, crystal violet stained wells). These data, similar to impedance growth curves for other mammalian cells reported in literature [16, 175], validate the impedance measurements obtained from this new microelectrode array device which has extended capabilities for multi-well and multi-frequency determinations.

5.3.2. Device and system capabilities

The measurement system and the impedance array device can be configured in different ways to suit the application and the requirements of the user. From the software end, the system offers flexibility in the selection of measurement parameters such as excitation frequency, voltage, and the time interval between measurements. This enables measurements to be made either at a single frequency or at multiple frequencies in the range of 5 Hz- 13 MHz. Data can be acquired continuously or at specific longer intervals with the smallest interval being ~1 min per frequency point for 36 electrodes. The excitation voltage can also be varied in the range of 5 mV-1.1 V. From the device end, the effect of modifying physical characteristics such as electrode dimensions, shape, geometry, and surface characteristics on impedance measurements can be compared in parallel under similar environmental conditions. The impedance responses of biological samples can be investigated in parallel using varied electrode configurations to evaluate the most useful electrode design for specific applications. Furthermore, chemical stimuli in the form of drugs can be introduced into the wells to perform dose dependency studies using this platform. This reconfigurable system will prove itself very useful in multi-user facilities because of its inherent flexibility for application development. A high-throughput, reconfigurable system such as this offers researchers the opportunity to evaluate hypotheses in a more efficient manner to develop next generation technology. We demonstrate the flexibility offered, through two specific experiments as described below highlighting different aspects of the reconfigurable nature of this system.

5.3.2.1. Evaluation of electrode geometry on impedance measurements

Electrode geometry

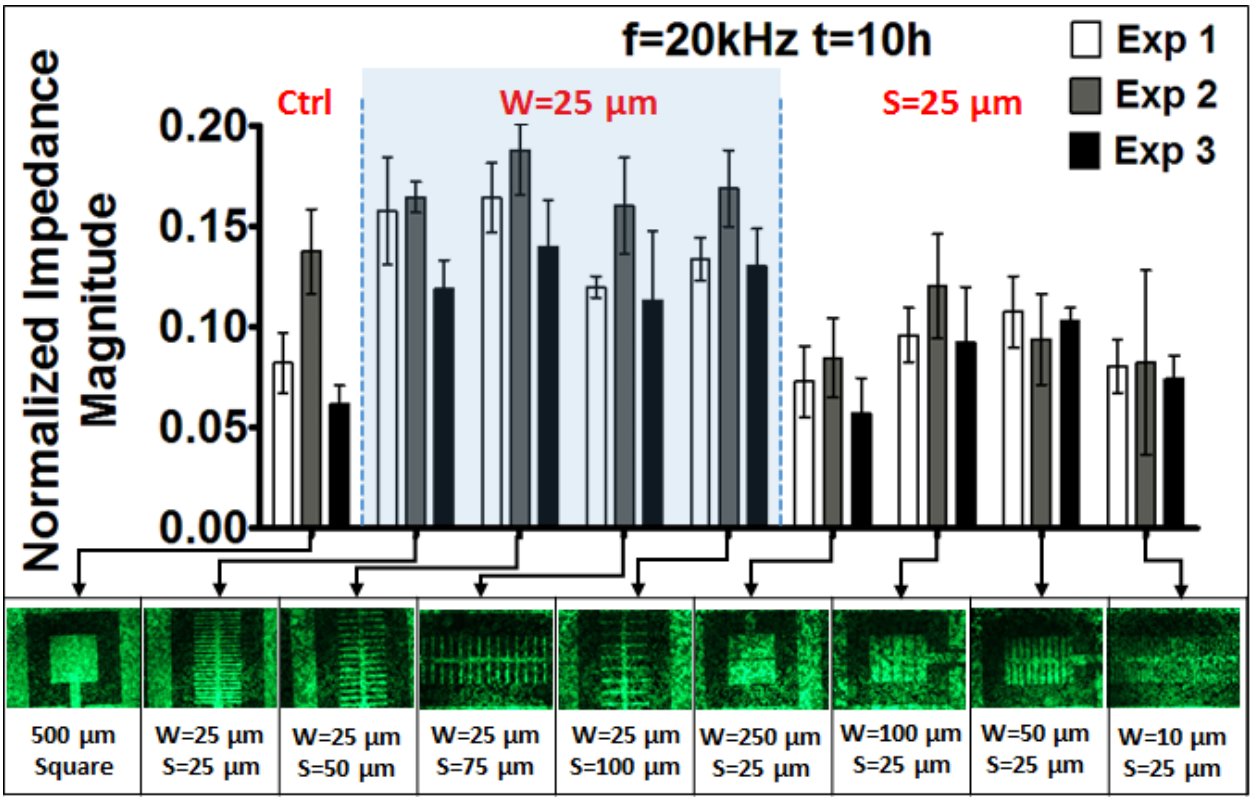

Figure 5.5 The normalized impedance magnitude 10 h after cell seeding at f=20 kHz for nine different electrode designs with varying branch widths and spacing (shown below). Bars represent mean±SEM and results shown are from three experiments with four electrodes per experiment.

We designed microelectrodes to systematically study the effect of electrode geometry parameters on the sensitivity of the electrodes to bioimpedance measurements from MDA-MB-231 breast cancer cells. A single lumped area electrode with a 500 µm square design and a total Area (A_L) =250000 µm^2 served as the control. A total of eight distributed area electrodes with a branched design were implemented where the total area of the electrode was equal to the control (A_D=A_L) (**Figure 5.5**). In the first four designs, the width of the electrode branch was fixed at W=25 µm which is comparable to the size of a single cell. The spacing between the electrode branches was varied between 25, 50, 75 and 100 µm in these designs. In all these designs, the number of branches was kept constant at 20. In the next four designs, the spacing between the electrode branches was kept constant at S=25 µm and the width of the electrode branch was varied between 250, 100, 50 and 10 µm. In these designs, the number of branches were also varied as 2, 5, 10 and 50, respectively. The counter electrode in all designs was positioned around the sensing

electrode and had an area of >5 times the area of the sensing electrode. The spacing between the electrode and the width of the counter electrode was 250 μm and kept constant in all designs for uniformity. It should also be noted that the length of the branches was also kept constant in all the designs and was equal to 500 μm. A total of nine electrode designs, in quadruplicate were realized in a single electrode array device. This enables the assessment of all the electrode designs in a single experiment with minimal variations in environmental and sample conditions.

Cell response dependency on electrode geometry

The device was pre-loaded with 80 μl culture medium/well, and background impedance measurements from cell culture medium were obtained. MDA-MB-231 breast cancer cells were harvested from confluent cell cultures and seeded (10^5 cells/ml or 8000 cells/well) onto the 36 electrodes in the high-throughput bioimpedance assay. The PDMS cover was used to seal the wells and parafilm was used to seal the edges of the device to further minimize evaporation. Bioimpedance measurements were made continuously over the frequency range of 1 kHz-1 MHz (31 log-distributed frequency points) for t=20 h and the experiment was repeated on three separate devices (N=3, n=36). Normalized impedance magnitude (Znorm) was obtained by subtracting first and then dividing the impedance due to cells by the corresponding impedance due to cell culture medium for each electrode. Overall, the results from n=12 electrodes of each design obtained from N=3 separate experiments were analyzed and shown in **Figure 5.5**. We chose the t=10 h time point for these analyses as it gives adequate time to cells to attach on electrodes It should also be noted that we show the data obtained at the frequency f=20 kHz which is at the middle of the frequency spectrum used. The electrodes with W=25 μm exhibit higher Znorm values than the wider electrodes including the control design. Cells prefer to attach and spread along the boundaries of electrode branches as can be seen in the inset fluorescence images in Figure 2. The cells in these images were stained fluorescently green with calcein AM. A branch width of W=25 μm is more closely matched with the size of a single cell and this provides a possible explanation for the higher sensitivity of branched electrodes to bioimpedance changes. Thus, branch width was identified as a more important design parameter than branch spacing based on the results from out experiment shown here. This determination was made possible within one week due to the flexibility and high-throughput offered by the system.

5.3.2.2. Effect of excitation voltage

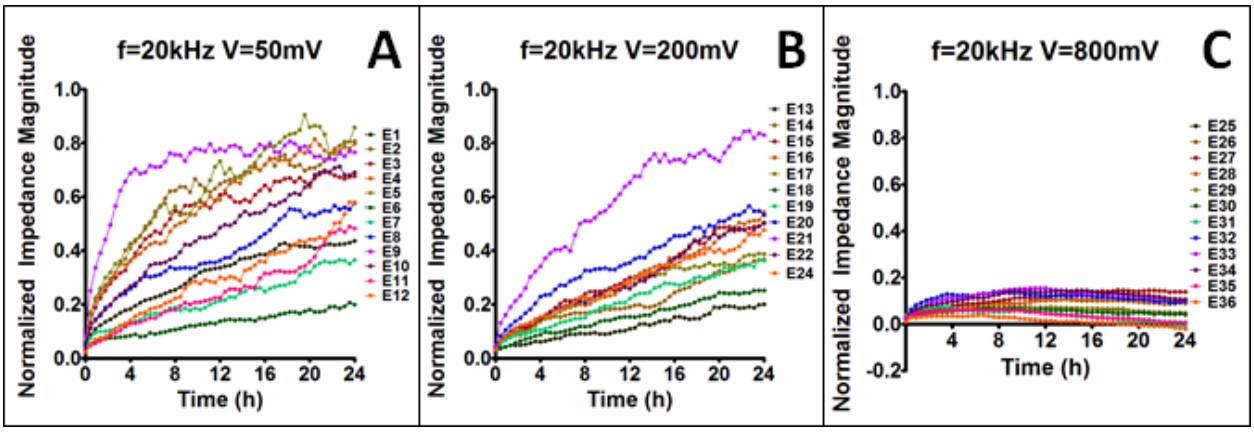

Figure 5.6 The time course of normalized impedance magnitude for each electrode for excitation voltages of 50 mV (A), 200 mV (B) and 800 mV (C) with n=12 electrodes each. Responses from individual electrodes (E = 1-36) are displayed in different colors.

The selection of the excitation voltage applied to biological samples is dependent on the application. For instance, electroporation which is a technique used to increase the permeability of cell membranes, requires a higher excitation voltage than bioimpedance measurements [27]. Bioimpedance measurements made with very low excitation voltages would also be susceptible to higher noise making the measurements less reliable. Here, the excitation voltage applied to the electrodes was varied under control of the LabVIEW VI in order to evaluate the effect on impedance measurements from MDA-MB-231 cells. Three different excitation voltages of 50 mV, 200 mV and 800 mV were tested on a single impedance array device with n=12 electrodes per excitation frequency. First the impedance of cell culture medium in the impedance array was measured and then MDA-MB-231 cells were harvested and introduced onto the electrodes. The impedance was monitored continuously on all 36 electrodes for 24 h.

The impedance measurements made at 20 kHz were normalized against the impedance of culture medium and plotted versus time in **Figure 5.6**. The scale of the graphs was held constant to illustrate the bioimpedance responses of identical cell populations to varying excitation voltages. Figure 3(C) indicates that an excitation of 800 mV was too high and adversely affected the cell culture. Cytotoxicity resulted in low Znorm values (<0.2) and decreasing trends in all the electrodes. Figure 3 (A, B) show that for excitation voltages of 50 mV and 200mV, the final value of Znorm at the end of 24 h is greater than 0.2 for majority of the electrodes. The differences in the final values of Znorm may be attributed to differences in the initial number of cells attaching to the electrodes after cell seeding. Even the electrodes with low Znorm values (<0.2) display an

increasing trend indicating continuing cell attachment. Thus, both 50 mV and 200 mV are suitable excitation voltages for making cell bioimpedance measurements in this system. The use of a higher excitation voltage is recommended to achieve a more favorable signal to noise ratio [176]. Hence, 200 mV excitation would be the appropriate choice for measurements of bioimpedance in mammalian cell monolayers in our system.

5.4. Conclusions

This section presents a new sensing system comprised of a wafer-level, high throughput 36-electrode impedance array in combination with electronic controls over frequency, voltage and time intervals and for bioimpedance measurements. The unique advantages of this system are the ability to readily reconfigure electrode design and electrical parameters which offer the user the flexibility required in developing and tailoring technology for specific applications, as well as providing a low working volume.

6. Microfluidic approach to high-content single-cell analysis of biophysical heterogeneity

6.1. Introduction

The need for technologies for single cell analysis is driven by a clear appreciation that a single clonogenic tumor stem cell is sufficient to produce a fatal tumor [177]. Such technologies also enable assessments of population-level heterogeneity present in cancer cells within a single tumor which has implications in predicting disease progression and therapy resistance [178, 179]. Quantifying cellular properties and their responses to treatments at the single cell level, in order to detect, cure or manage this disease is a great challenge. Recent technological advancements in micro- and nano-engineering have enabled researchers to identify, sort, and probe the properties of individual cancer cells [42, 180]. Han et al. recently reported a microfluidic chip for controlled separation and sequencing of nuclear genomic DNA and cytoplasmic messenger RNA from the same single leukemia cells which provides further opportunities to investigate the link between genetic and transcriptional signatures in cancer [181]. Another example is a high throughput microfluidic platform that employs hydrodynamic forces to measure the deformability of single cells which can be used for large population analyses such as identifying malignant cells in pleural fluids and pluripotency in stem cells [182]. These research directions promise to improve patient care by making more precise, individualized diagnostic and prognostic decisions for cancer patients possible.

The genetic heterogeneity of tumor populations is well-documented [183, 184]. More recently, the impact of non-genetic heterogeneity arising through epigenetic, metabolic and morphological/biophysical mechanisms on creation of distinct phenotypes has gained interest, and it will become important to decipher how these non-genetic sources of heterogeneity interact in tumor cells of diverse genetic backgrounds [185, 186]. Cells undergo biophysical changes as they go through cancer progression [187, 188]. Many research reports have shown that cancer cells are softer and less viscous than corresponding benign cells [189, 190]. The dysregulation of the cell cytoskeleton in cancer cells increases their invasion potential, enables them to escape from the primary tumor and migrate to distant sites during metastasis to form secondary tumors [191]. Our laboratory has used atomic force microscopy (AFM) to demonstrate this relationship between cancer progression and visco-elastic properties of cells in human breast and mouse ovarian cancer

cell models [190, 192]. In addition, metabolic reprogramming modulates intracellular signaling in cancer cells engages mitochondrial pathways [193], promotes alternative membrane glycosylation patterns [194] and effects desmoplasia, a process whereby cells increase stromal stiffness, both of which impact cellular biomechanics [195].

The electrical properties of biological cells and tissues become altered because of morphological and physiological changes [196]. For instance, the membrane capacitance can be impacted due to changes in surface charge, lipid composition and ion channel regulation which occur during cancer progression [197]. The use of bioimpedance in cancer has afforded investigators a simple means to monitor cell suspensions, tissues, cell-substrate adhesion, spreading, micromotility, and differentiate between normal and cancer cell types [65, 111, 198]. These differences have been attributed to the dielectric properties of cells which are governed by cell membrane composition, internal conductivities, and size [43, 82, 103]. All these studies support the development of devices to analyze the biophysical heterogeneity of individual cells within cell populations and the use of biophysical parameters as possible label-free biomarkers of tumor grade, metastatic potential, and response to drug treatments.

Microfluidics-based assays offer a variety of high throughput, rapid analysis platforms to measure the biophysical properties of single cells [42, 180]. The transit time of single cells through a narrow constriction channel has been used as a biophysical measure of deformability to differentiate between cell types [44, 199]. The remarkable cellular deformation that occurs during passage through a constriction channel suggests that cellular bioimpedance responses to this mechanical stress might provide new biophysical markers. We pursued development of technology to monitor bioimpedance properties in real-time as a function of mechanical stress. Here, we report a microfluidic assay in which the passage of single cells through a narrow deformation region is monitored using an electrode pair integrated into the microchannel. These electrodes serve the dual purpose of automating transit time measurements and measuring the impedance at multiple frequencies enabling content-rich measurements from single cells pre-, post- and during mechanical deformation. In addition, the narrow constriction channel confers high sensitivity to the impedance measurements due to the fact that the cells, being larger than the deformation region, occupy the channel completely when travelling through it, thereby minimizing alternate current paths around the cell. We used this assay to obtain measurements from two tumorigenic

(MDA-MB-468, MDA-MB-231) breast cancer and one non-tumorigenic (184A1) breast cell line and assessed the heterogeneity in their single-cell biophysical properties.

6.2. Materials and Methods

6.2.1. Design

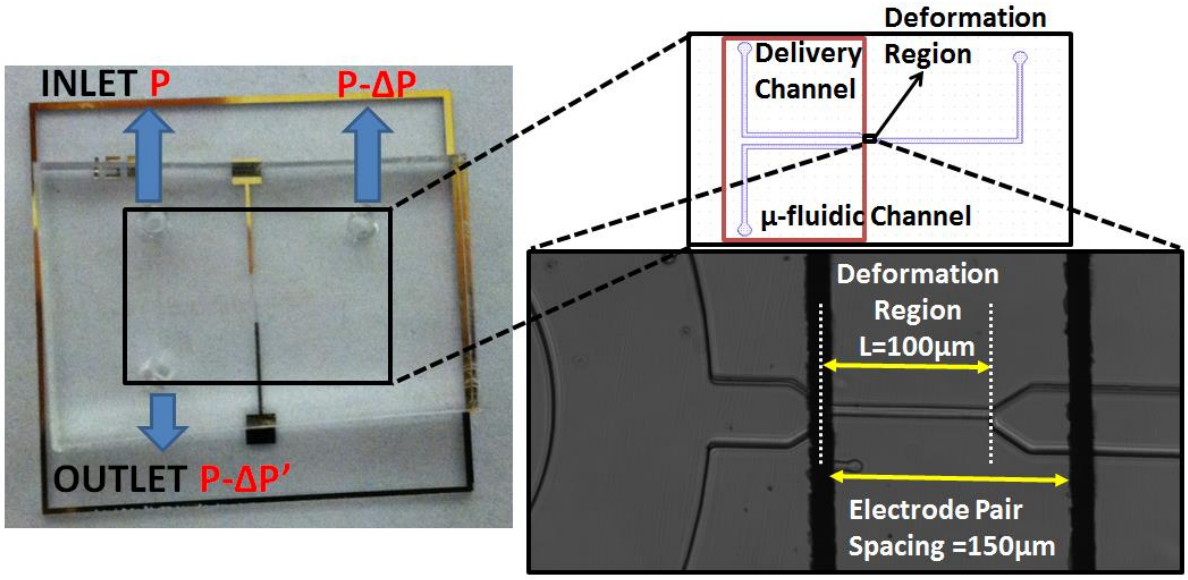

Figure 6.1 Photograph of the microfluidic device with a magnified view of the deformation region.

The device is shown in **Figure 6.1** with a magnified view of the microfluidic channel design. The delivery channel is U-shaped with an inlet and an outlet and the deformation region which is 8 μm-wide, 8 μm-deep, 100 μm-long branches off from the middle of the U. The dimensions of the cross section are about half the typical cell diameter and ensure that the cell is completely deformed when it passes through this region. A pressure gradient is applied through a difference in the liquid level in the inlet and outlet reservoirs which establishes a continuous free flow of single cells suspended in the culture medium through the delivery channel. Cells are then pulled through the deformation region by applying a negative pressure on the third port and two electrodes 150 μm apart are integrated into the channel to measure the impedance of single cells as they pass. It should be noted that when a cell is in the deformation region, it completely blocks the channel and shields the cells in the delivery channel from the influence of the negative pressure on the other side. Therefore, for the duration of its travel through the channel, it prevents a second cell from being attracted into the deformation region. Also, the pressure gradient in the delivery channel ensures that cells are deflected towards the outlet reservoir and do not line up near the

entrance, when a cell is already in the deformation region. This mechanism greatly reduces the clogging in the device.

6.2.2. Fabrication

The device was fabricated in polydimethylsiloxane (PDMS) using a master mold with the negative photoresist SU-8. The master mold was obtained using a two-step fabrication process with SU-8 2007 and SU-8 2025 to obtain different thicknesses for the channel (~60 μm) and the deformation region (8 μm). The electrodes were patterned on a pyrex/glass wafer by evaporation of Cr/Au after photolithography followed by a lift off process in acetone. The diced glass/pyrex and the PDMS layers were exposed to oxygen plasma for 50 seconds; the electrodes on the pyrex chip were aligned with the deformation region in the PDMS channel under a microscope using a few drops of methanol and transferred onto a hot plate. After 10 minutes, the device was removed from the hot plate and left to cure overnight for a strong bond before experiments.

6.2.3. Experimental Setup

The microfluidic device was mounted on a general purpose board (GPB), which has a cut-out for optical access to the device for microscopy and SMA adaptors for connectivity to make impedance measurements. The IDT Redlake NX-3 high speed camera was used to obtain images at the rate of 250 fps for 32 s. We used the Zurich instruments impedance spectroscope (HF2IS) to make measurements continuously at four frequencies (10 kHz, 20 kHz, 100 kHz and 800 kHz) in parallel using an excitation voltage of 1.25V at each frequency. The frame rate of the high speed camera was matched with the data acquisition rate of the impedance spectroscope and a measurement was made from the cell every 4 ms which was sufficient to get good resolution of the transit time measurements. A syringe pump (Harvard Apparatus) was used to apply the negative pressure on the third port. Since, the same device was used for measurements from different cell types, the device was cleaned by flushing the delivery and the deformation channels thoroughly with deionized water for 5 minutes prior to the introduction of a new cell type.

6.2.4. Cell Methods

Three breast cancer cell lines with low passage numbers, 184A1 (passage 12), MDA-MB-468 (passage 25) and MDA-MB-231 (passage 22), were used in this study that were generously provided to us by Dr. Ayesha Shajahan-Haq from Georgetown University. 184A1 cells are a non-tumorigenic breast epithelial cell line while the MDA-MB-468 and MDA-MB-231 cells are

tumorigenic triple-negative breast cancer cell lines with low and high metastatic potentials, respectively. The growth medium for the 184A1 cells was prepared from the MEGM kit obtained from Lonza by adding 0.005 mg/ml transferrin (Sigma Aldrich), 1 ng/ml cholera toxin (Sigma Aldrich) all the additives in the kit except the gentamycin-amphotericin B mix to the MEBM medium. The MDA-MB-468 cell growth medium was L-15 supplemented with 10% FBS. The MDA-MB-231 cell growth medium was DMEM-HG (ATCC) with 10% FBS. The 184A1 and MDA-MB-231 cells were maintained in a humidified incubator (37 ^{o}C, 5% CO_2) while the MDA-MB-468 cells were maintained in a chamber at 37 ^{o}C, 100% air. For experiments, cells were harvested from confluent cell cultures and suspended ($5x10^5$ cells/ml) in corresponding growth media.

6.2.5. Data Analysis

The high-speed movie for each run was analyzed in conjunction with the impedance profile to match the cells in the movies to events in the impedance profiles. Multicellular aggregates and cell fragments were eliminated from analysis at this stage. A MATLAB program was used to calculate cell entry and travel time through channel, peak and baseline impedance magnitude and phase at each frequency for single cells. Image J was used to measure the diameter of the cell in X and Y directions, before and after deformation. The size of the cell was calculated by taking the average of the diameter of the cell measured in the X and Y directions before deformation. The axial ratio (AR) before and after deformation was calculated by dividing the higher of the two values obtained from the diameter measurement in X and Y directions, by the lower value and is an indication of the shape of the cell. An AR of 1 indicated a uniformly round cell whereas ARs greater than one indicated the degree of elongation of the cell in one direction compared to another. The change between the peak and baseline of the real and imaginary parts of the complex impedance was calculated for 50 cells of each cell type.

6.2.6. Statistical Tests

The D'Agostino & Pearson omnibus statistical test in Prism GraphPad was performed on all biophysical parameters analyzed in this study to test for normality of the distribution. Since the majority of the biophysical parameters did not pass the statistical test for normality, the following statistical methods were used to compare and contrast the data obtained from different cell lines. Box and whiskers plots of the median interquartile with range were used to enable visualization of

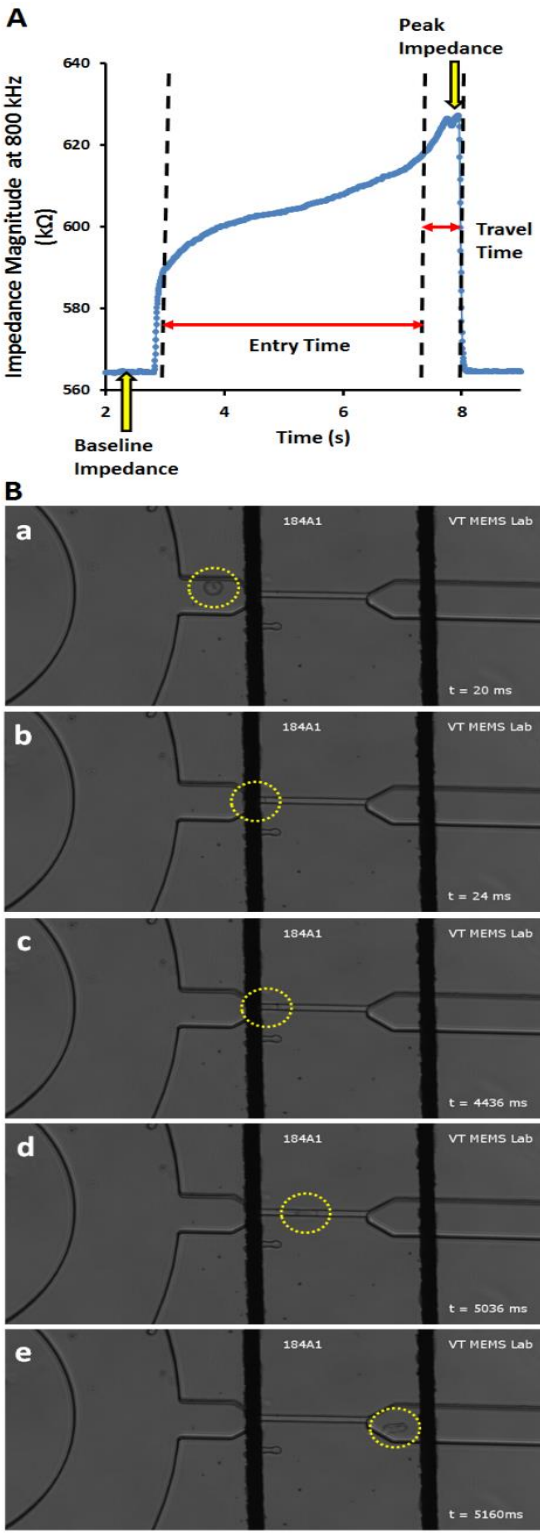

Figure 6.2 (A) The impedance change due to a single 184A1 cell as it passes through the deformation region (B) Images tracking the 184A1 cell through the deformation region.

the level of heterogeneity in the data for each cell line where larger boxes indicate a more heterogeneous population. The asymmetry of the box indicates the skewness in the population heterogeneity. Quadratic entropy (QE) was used as a metric for comparing heterogeneity levels among the three cell lines. It is sensitive to the spread of the distribution and has been used by researchers in quantifying the diversity of cellular phenotypes in cancer tissues[200]. It is calculated as

$$QE = \sum_{i>j=1}^{N} d_{ij} \times p_i \times p_j \quad (1)$$

where d_{ij} is the difference in the value of the ith and jth cells, p_i and p_j are the frequency of ith and jth values respectively. Bootstrapping was used to calculate 95% confidence intervals using 10000 bootstrap samples of the median in MATLAB. These confidence intervals are depicted using bars marked on the scatter plots along with the median. The non-parametric Kruskal-Wallis analysis of variance was used to test for statistical differences between the three cell lines and the Dunn-Sidak post hoc test was used to compare each pair.

6.3.Results

Figure 6.2(A) shows the characteristic impedance profile at 800 kHz as a single 184A1 cell moves through the deformation region in the microfluidic channel and **Figure 6.2(B)** tracks the cell in images obtained using the high-speed camera. The impedance value measured due to the

cell culture medium only in the absence of a cell is referred to as the baseline impedance. When a cell approaches the entrance of the channel (**Figure 6.2(B-a)**), there is a sudden change in the impedance as can be seen from the steep slope. When the cell gets trapped at the entrance and is squeezing into the deformation region (**Figure 6.2(B-b)**), the impedance rises more gradually. This process of cell entry is slow and contributes to the majority of the transit time of the cell through the deformation region as observed from the timestamp in **Figure 6.2(B-c)**. When the cell has completely entered the channel and is traveling through the deformation region, the impedance reaches a maximum or peak value (**Figure 6.2(B-d)**). The cell exits the deformation region rapidly as can be seen from the steep slope back to the baseline and **Figure 6.2(B-e)**. Therefore, the entry and travel times of the cell through the channel can be calculated from the impedance profile.

6.3.1. Cell deformability

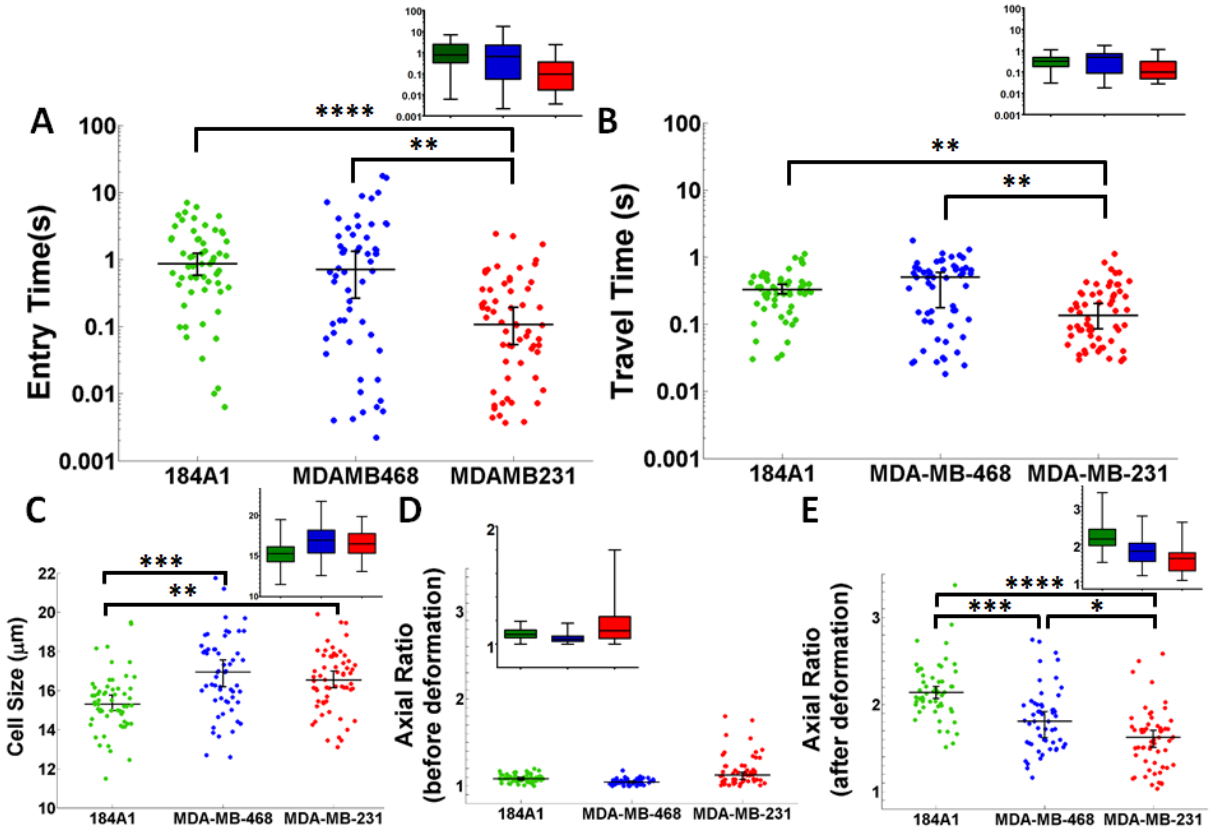

Figure 6.3 Scatter plots of entry time (A) and travel time (B) through the deformation region extracted from the impedance data and cell size (C), axial ratio before (D) and after (E) deformation extracted from the high-speed videos for (n=50) cells of each cell type. Bars indicate 95% confidence intervals for the median. Inset images are box and whiskers plots for same data. Bars indicate range. * P<0.05 ** P<0.01 *** P<0.001 **** P<0.0001

The time the cell takes to squeeze into the narrow channel is the entry time and the time the cell spends traveling through the channel is the travel time. As the cell has to completely deform in order to squeeze into the channel, the transit time, defined as entry time plus travel time through the deformation region, can be used as a measure of its deformability and hence, its mechanical properties. The entry time of cells into a narrow channel is a sensitive indicator of their visco-elastic properties [201]. Here, for populations of 50 cells of each cell line, we analyzed the entry time (**Figure 6.3(A)**) and travel time (**Figure 6.3(B)**) of cells moving through the deformation channel.

The entry times for the non-tumorigenic 184A1 cell population were more homogeneous (QE=0.3) and displayed a tight distribution near the central median in contrast with the tumorigenic MDA-MB-468 (QE=0.6) and MDA-MB-231 (QE=0.5) cell populations that displayed a larger spread (**Figure 6.3(A-inset)**). The highly metastatic MDA-MB-231 cells showed the shortest entry time which was significantly lower than the non-tumorigenic 184A1 and the MDA-MB-468 cells with low metastatic potential. These measurements indicate that the highly invasive MDA-MB-231 cells are more deformable than non-tumorigenic 184A1 cells, which is in agreement with previously published stiffness measurements from AFM [202]. The MDA-MB-468 cells with low metastatic potential are also significantly less deformable than the MDA-MB-231 but slightly more deformable than the non-tumorigenic 184A1 cells. Interestingly, the normal 184A1 cell line have the largest median entry time despite their smaller size indicating they were very stiff in comparison to the malignant cell lines. Hence, the entry time of a cell population can be correlated with its tumorigenic potential.

The travel time (**Figure 6.3(B)**) through the deformation channel followed a pattern similar to the entry time for three cell lines. Travel times through the channel occurred more rapidly than entry, and there was little heterogeneity in travel time. These observations agree with a previous study of non-tumorigenic and tumorigenic breast cells [201].

The variation in cell size within each of the cell lines studied was normally distributed (**Figure 6.3(C)**). The average diameter (±SD) of the metastatic cell lines, MDA-MB-468 (16.8±2.1 μm) and MDA-MB-231 (16.5±1.7 μm), was similar; because the highly metastatic MDA-MB-231 cells showed a significantly shorter entry time despite their similarity in size to the MDA-MB-468 cells, this suggests that the more highly metastatic cell line is more deformable. In contrast, the non-

tumorigenic 184A1 (15.4±1.6 μm) cells were significantly smaller than both metastatic cell lines, yet 184A1 had an entry time comparable to that of the MDA-MB-468 cells and slower than that of the MDA-MB-231 cells. Thus, taking into consideration both the cell size and the entry time parameters, the non-tumorigenic 184A1 line typifies a stiffer biophysical phenotype than observed for the metastatic lines which show greater ease of deformability.

6.3.2. Shape recovery after deformation

The median ARs of each cell culture line before deformation (**Figure 6.3(D)**) indicate that all 3 lines were comprised of highly rounded cells: 184A1 (1.08), MDA-MB-468 (1.04) and MDA-MB-231 (1.11). There was however, a greater range in the ARs within the MDA-MB-231 cell population (1.0-1.8; QE=0.09) than the MDA-MB-468 (QE=0.02) and 184A1 (QE=0.03) cells (**Figure 6.3 (D-inset)**) and these highly metastatic cells were more elongated with an AR skewed towards a value of 2. During transit through the constriction channel where cells were forced to deform to the channel size (8 μm) and hence, AR of all cell lines was similar (median AR≈3.75).

As a measure of recovery from mechanical deformation, the ARs of the cells as they emerged from the deformation channel were compared. After exiting the deformation channel, the non-tumorigenic 184A1 (AR 2.14) breast epithelial cells were significantly more elongated than both the breast cancer cell lines MDA-MB-468 (AR 1.81) and MDA-MB-231 (AR 1.62) (**Figure 6.3(E)**). The non-tumorigenic 184A1 cells recovered more slowly than either metastatic cell line and, the most highly metastatic MDA-MB-231 cells recovered fastest. AR at exit thus correlated with tumorigenicity and metastatic potential.

6.3.3. Electrical model

Impedance is a complex number that is a measure of the opposition to the flow of electric current. In this device, electrodes are located on either side of the deformation region and the path of current flow is through the narrow channel. A cell positioned in the deformation region blocks the flow of electric current more effectively than culture medium. Thus, impedance increases when the cell is in the channel. Also, the electric field lines are concentrated in the narrow deformation region as seen from a two dimensional simulation done in COMSOL Multiphysics. **Figure 6.4(A)** shows the surface plot of the electric field strength in the microfluidic device and it shows that the electric field due to the applied voltage (1.25 V, 800 kHz) on the electrodes with 150 μm spacing is maximal in the deformation region. This is true for all excitation frequencies tested and implies

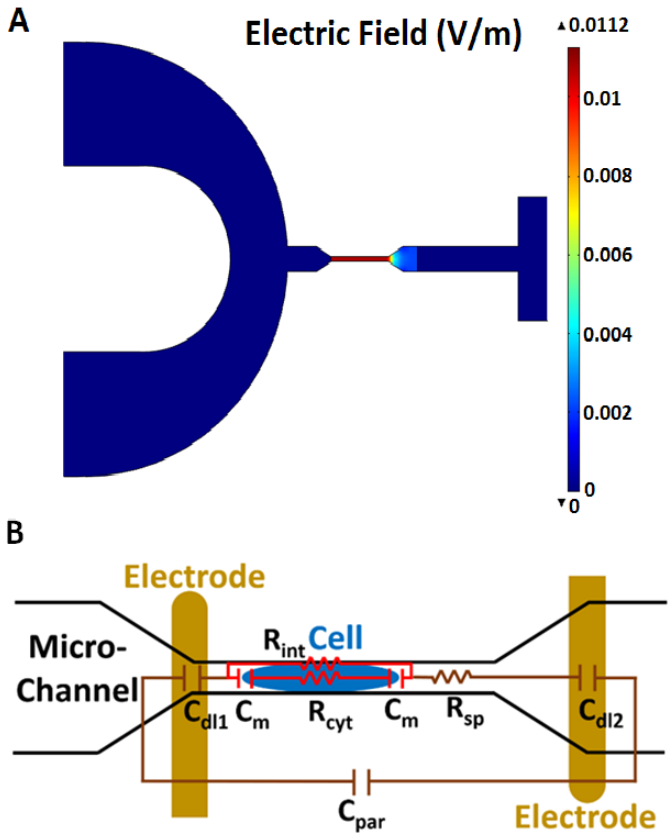

Figure 6.4 (A) 2D surface plot of electric field strength in the microfluidic channel. (B) Schematic of the electric circuit model used to extract cell parameters from impedance measurements. Circuit element legend Cdl1,2- double layer capacitance; Rsp- spreading resistance; Cpar- parasitic capacitance; Cm- membrane capacitance; Rcyt- cytoplasm resistance; Rint- cell-channel wall interface resistance

that the impedance measurements are most sensitive to events occurring close to or in this deformation region.

The cell electrical response during deformation was continuously and simultaneously monitored at four frequencies, 10 kHz, 20 kHz, 100 kHz and 800 kHz, (**Figure 6.4**) to capture the cell impedance profile to mechanical stress at both high and low frequency imposed voltages. The electric circuit model used to extract cell parameters from the multi-frequency impedance measurements is shown in **Figure 6.4(B)**. When no cells are present near the electrode, the primary contribution to complex impedance is the capacitance of the double layer formed at the interface of the electrode and the surrounding medium that effectively acts as an electrolyte. Hence, the circuit used to model the baseline impedance consists of a double layer capacitance (Cdl1, Cdl2) at each electrode present in series with the spreading resistance (Rsp) of the culture medium in the deformation region. Capacitance (Cpar) is used to capture any parasitic effects in the measurement circuit.

Biological cell membranes can be modeled as a capacitance (Cm) and the cell cytoplasm as a resistance (Rcyt). The maximum change in impedance magnitude or peak impedance, occurs when the cell is in the center of the deformation region and completely blocks the channel. Hence, the path of current flow at the peak impedance is either through the cell, which is represented by cell membrane capacitance in series with cytoplasm resistance, or between the cell and the channel wall which is represented by the interface resistance (Rint). The deformed cell is approximately 30 µm long when it is in the narrow channel. Hence, the spreading resistance (Rsp') in this circuit

was estimated as 0.7*Rsp. It should be noted that all capacitors in the circuit were modeled as constant phase elements which is a standard practice in electrochemical circuits.

To obtain unique values from curve fitting, Cdl1 and Cdl2 were modeled together to obtain a single capacitance Cdl. First, the baseline impedance was used to obtain Cdl, Cpar and Rsp. These values were inserted into the circuit for peak impedance to obtain Cm, Rcyt and Rint. All parameter values were obtained from curve fitting in MATLAB using the non-linear least squares method where the R^2 values for goodness of fit were greater than 0.95. The membrane capacitance (Cm) obtained from the model was converted to specific membrane capacitance by dividing by area of cell membrane at the two ends which is estimated as the hemispherical surface area ($4\pi r^2$ where r=4 μm). The cytoplasm conductivity was obtained by multiplying the inverse of Rcyt with the cell length in the channel (~30 μm) and dividing it by the channel cross section area (8×8 μm^2).

6.3.4. Cell bioelectrical properties

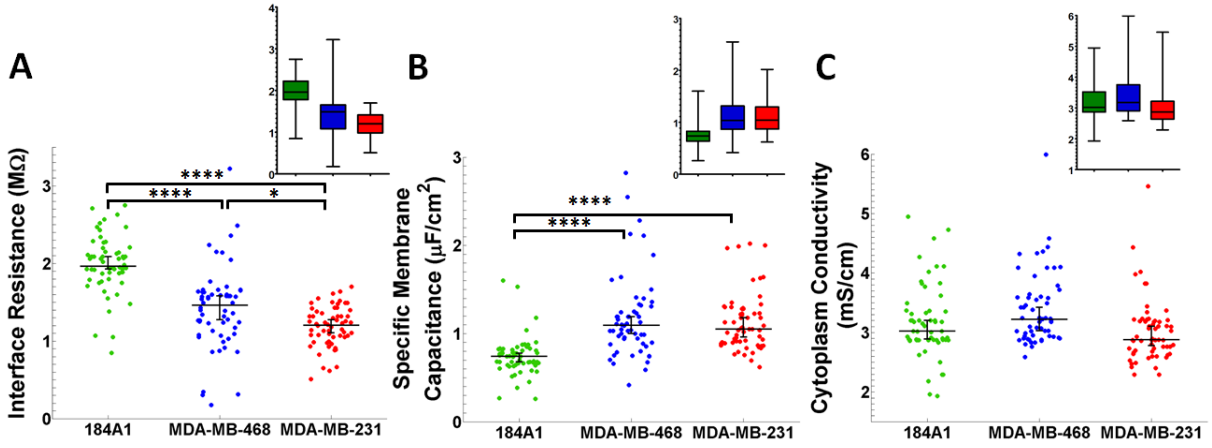

Figure 6.5 Interface resistance (A), specific membrane capacitance (B), and cytoplasm conductivity (C) obtained for the three breast cell lines. Bars indicate 95% confidence intervals for the median. Inset images are box and whiskers plots for same data. Bars indicate range. * P<0.05 **** P<0.0001

The interface resistance (Rint) represents the resistance between the cell and the walls of the narrow microfluidic channel as the cell is traveling through it. Rint was significantly larger in non-tumorigenic 184A1 cells in comparison to the tumorigenic cells. Thus, 184A1 cells, despite their smaller size appear to contact the channel wall more tightly during deformation, which might reflect increased surface friction. The median Rint values of the highly metastatic MDA-MB-231 cells were significantly lower than that of 184A1 cells.

The tumorigenic breast cell lines (MDA-MB-468 and MDA-MB-231) had significantly higher specific membrane capacitance than the non-tumorigenic 184A1 cells. Biological determinants of membrane capacitance include changes in cell dielectric properties due to alterations in lipid composition, surface charges and ion channel profile, and there is some published evidence that these alterations do associate with increasing invasion potential [197, 203]. The specific membrane capacitance values for the tumorigenic MDA-MB-468 (QE=0.5) and MDA-MB-231 (QE=0.2) cell populations were prominently more heterogeneous than the non-tumorigenic 184A1 (QE=0.1) cell line (**Figure 6.5(B-inset)**).

The cytoplasm conductivity is one measure of the biophysical properties of the cell interior. Interestingly, the cytoplasmic conductivity of all three cell lines studied was similar. This suggests that the known tumor-associated reorganization of internal cytoskeleton, particularly acto-myosin complexes [204], microtubules [205], and the marker of epithelial-mesenchymal transition, the intermediate filament vimentin [206], do not effect significant changes in the cells' electrical conductivity.

Resistance at the interface (Rint) between the cell and the channel wall is dependent on the closeness of contact and the friction between these two surfaces. A parametric analysis (**Figure 6.6**) shows that of all the cell parameters, Rint has the largest effect on peak impedance changes.

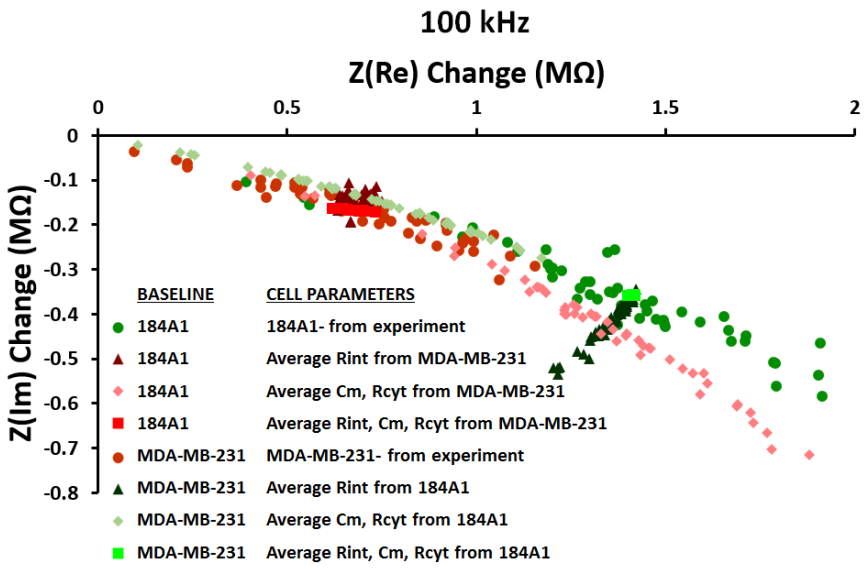

Figure 6.6 Parametric analysis of impedance changes with respect to baseline.

When, the average Rint value from MDA-MB-231 cells was combined with parameters obtained from 184A1 baseline impedance, the impedance changes of these 'hypothetical' cells moved into MDA-MB-231 cell regime on the graph. Whereas, when the cell parameters Ccell and Rcyt were used, they resulted in

smaller shifts in impedance. Lower surface friction also enables faster transit through the deformation region suggesting aggressive cells maybe aided by this factor during metastasis [199].

6.3.5. Classification of normal and tumor cells using single-cell biophysics

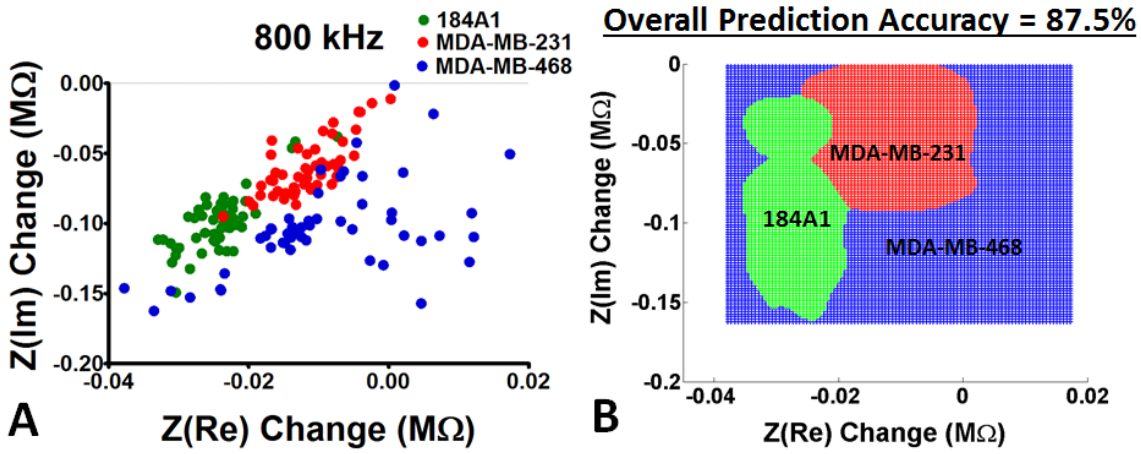

Figure 6.7 (A) Impedance changes in real versus imaginary parts due to single cells at 800 kHz and (B) zones defined for each cell line by the non-parametric Naive Bayes classification.

The highly sensitive measurement of bioimpedance in cells during deformation within a narrow channel provided us with a detailed single-cell impedance profile. The complex impedance value measured at each frequency can be expressed as a magnitude (Z) and a phase angle (θ) or as the real part (Z(Re)=Zcosθ) and imaginary part (Z(Im)=Zsinθ). In **Figure 6.7(A)**, single-cell changes in real ((Z(Re)) versus imaginary (Z(Im)) components of impedance at 800 kHz are plotted. Individual normal 184A1 cells (green) are distinguishable from the tumorigenic MDA-MB-468 (blue) and MDA-MB-231 (red) cells. The high frequency (800 kHz) stimulation probes the internal cytoskeletal and membrane properties, and the assortment of cells into the green, red, and blue sub-groups is an indication that internal/membrane structures differ sufficiently among these cells to enable their identification using bioelectric profiling.

To analyze the accuracy of bioelectric profiling, cell zones were defined using the Naive Bayes classifiers (**Figure 6.7(B)**). This model was then applied to the raw bioimpedance data that was used to assign a cell to a particular cell line. The percentage of non-tumorigenic 184A1 cells that were correctly assigned was 92%. Highly metastatic MDA-MB-231 were correctly identified in 94% of cells. Thus the electrical distinctions between non-tumorigenic and highly metastatic breast cell lines were quite prominent. Somewhat less robust identification (76%) of the low

metastatic breast cells of the MDA-MB-468 line was achieved by electrical profiling. Overall, Naive Bayes analysis of the complex components of single-cell impedance using our technology accurately identified three pathologically distinct subtypes of breast cancer with 87.5% accuracy.

6.4. Discussion and Conclusion

During cancer progression, cells and their microenvironment undergo coevolution that ultimately results in tumor metastasis [207]. During this process, tumors frequently undergo what is referred to as the epithelial-mesenchymal transition [208], and tumor cell-stromal cell cross-talk results in pro-metastatic alterations in gene expression and cytoskeleton [209]. Among tumors there is also variation in the relative composition of tumor stem cells/cancer-initiating cells that will impact progression to metastatic disease [210]. These represent sources of cell heterogeneity in tumor populations which we and others suggest are important in ascertaining disease progression and patient prognosis. Biophysical profiling of tumor cell populations is an emerging approach to ascertain malignancy and risk for cell invasion and migration considered to be one of the hallmarks of cancer [211].

The tendency for cell softening in the viscoelastic properties during cancer progression is a well-documented biophysical alteration that might play a role in tumor cell penetration of the tissue-matrix, access to circulatory systems and metastasis [212]. Mechanical changes have been attributed to the reorganization of the cell cytoskeletal proteins actin and tubulin and cytoskeleton-targeted therapeutics is one strategy to contain cancer and impede metastasis [213, 214]. Also important are alterations in cell electrical properties during cancer progression. Tumor cell membranes are relatively enriched in many classes of lipids [197, 203, 215], with the result that tumor cells can exhibit an increased electronic polarizability of the cell membrane and increased specific membrane capacitance. In fact, we observed that 84% of breast cancer cells exhibited increased membrane capacitance compared to non-tumorigenic 184A1 cells (**Figure 6.5(B)**). Within the cell membrane, levels of subtypes of calcium, chloride, and potassium ion channels are extensively modified, and these effect not only intracellular signaling pathways, but also cell membrane potential [216, 217].

Our interests lie in the design and development of microfluidic based devices to profile single-cell biomechanical and bioelectrical attributes simultaneously as a means for identifying individual cells within a sample population that display “high-risk” profiles. To achieve this, we fabricated a

microfluidic chip with embedded electrodes and profiled a small panel of breast cells using cell lines of known tumorigenic and metastatic potential. Using the combined capabilities of microfluidics and bioimpedance, we observed that model breast cell lines representing tumorigenic and non-tumorigenic breast epithelium display significant differences in the parameters of channel entry time, cell shape recovery after deformation, cell-channel interface resistance, and specific membrane capacitance. The Naïve Bayes classification method applied to bioelectric profiling accurately assigned individual cells from three different breast cell culture models to their appropriate pathobiologic subtypes. Furthermore, the unique ability of our technology to obtain deformability and multi-frequency impedance information simultaneously for the same single cell permits us to begin to understand the biophysical attributes resulting in the outlier cells in the Naïve Bayes classification system. For instance, tumorigenic cells with very high ARs after deformation also had lower specific membrane capacitance values. We showed that these cells exhibit properties similar to the non-tumorigenic cells. A further application of this work is the use of label-free profiling of single-cell biophysical properties to quantify the effectiveness of targeted therapeutic drugs in cell populations.

7. Biophysical characterization of a hormone therapy resistant breast cancer cell model

7.1. Introduction

Breast cancer occurs due to mutations in breast cells that result in uncontrolled cell growth in the breast. From statistics published recently, it is the most commonly diagnosed form of cancer in American women with the highest rate of death [59]. Current treatment options for breast cancer primarily include surgery for localized tumor removal, radiation therapy and chemotherapy. In addition, several targeted secondary therapies are used to prevent breast cancer recurrence in patients. One such commonly used adjuvant therapy is hormone therapy, which is efficient in treatment of breast cancers expressing receptors for the female hormone estrogen.

MCF-7 is an immortalized cell line that is used as a model to study hormone therapy for breast cancer [218]. It is an estrogen receptor positive (ER+) cell line that is responsive to anti-estrogen drugs. The effect of these drugs has been shown to be reversible in MCF-7 cells on treatment with estrogen. In order to understand acquired resistance to anti-estrogen drugs in breast cancer genetically related variants were derived, two of which are LCC-1 and LCC-9 [219]. The LCC-1 cell line has been derived from a subpopulation of MCF-7 cells by further passaging them in nude mice. These cells are hormone-independent but hormone-responsive [220]. The LCC-9 cell line was derived from LCC-1 cells by selecting for resistance to the anti-estrogen drug Faslodex (ICI). This cell line is also tamoxifen resistant even though it has never been exposed to it [221]. Obatoclax (GX-15-070 or GX) is an experimental anti-cancer agent that is currently in clinical trials for many cancers. In cancer cells, GX inhibits proteins of Bcl-2 family, which induces apoptosis and causes cell death [222, 223].

In this work, we used LCC-1 and LCC-9 cells as a model to represent hormone therapy sensitive and resistant cells and studied their biophysical properties using electric cell-substrate impedance sensing (ECIS) and the microfluidic single-cell biophysics assay. These assays were used to probe the mechanism of GX action on LCC-1 add LCC-9 cells. Our results suggest differential sensitivity of LCC-1 and LCC-9 cells to GX with LCC-9 cells being more sensitive. Equivalent circuit models were used to estimate the role of the cell components such as cell membrane and in hormone therapy resistance and sensitivity to GX.

7.2. ECIS response of LCC-1 and LCC-9 cells treated with Obatoclax

7.2.1. Cell Methods

LCC-1 and LCC-9 cells were obtained from Dr. Ayesha Shajahan-Haq at the Lombardi cancer center in Georgetown University. They were propagated in T-25 cm^2 flasks and maintained in an incubator at 37 ^oC and 5% CO_2. The growth medium was IMEM supplemented with charcoal stripped serum. Cells (passage numbers 18-25) were harvested in growth phase from 60% confluent flasks for experiments. A stock solution of GX with a concentration of 10 mM was prepared in dimethylsulfoxide (DMSO) and the required concentration was obtained by diluting in cell culture medium.

7.2.2. Experiments

The 6X6 impedance array devices described in section 5.2.1 were used to obtain ECIS data from LCC-1 and LCC-9 cells. Bioimpedance measurements were made at 31 log-distributed frequency points over the frequency range 1 kHz–1 MHz with one measurement roughly made every half an hour. Cells were seeded at a density of 6125 cells/well with each experiment having both LCC-1 and LCC-9 cells with appropriate controls. Cell impedance was monitored for 24 h and then Obatoclax (GX) at with concentration 10 nM, 500 nM or 1 µM was added to each well. Impedance was monitored for another 48 h to evaluate the effect of GX. Due to increased evaporation occurring in the peripheral wells over the 72 hour experiments, only data obtained from the center 16 wells (4X4 array) were used in analyses.

7.2.3. Results

Figure 7.1(A) shows only the mean impedance value at 30 kHz from all electrodes in n=6 experiments. A red arrow is used to indicate the time point when GX is introduced in the wells over the 72 h time course of the experiment. GX induces apoptosis in LCC-9 cells [223] which is associated with cell detachment from the electrode and ultimately cell death. This is measured through a significant decrease in the impedance magnitude obtained from LCC-9 cells in response to GX (**Figure 7.1(C)**). In addition, higher concentrations of GX resulted in a more significant drops in impedance magnitude over time.

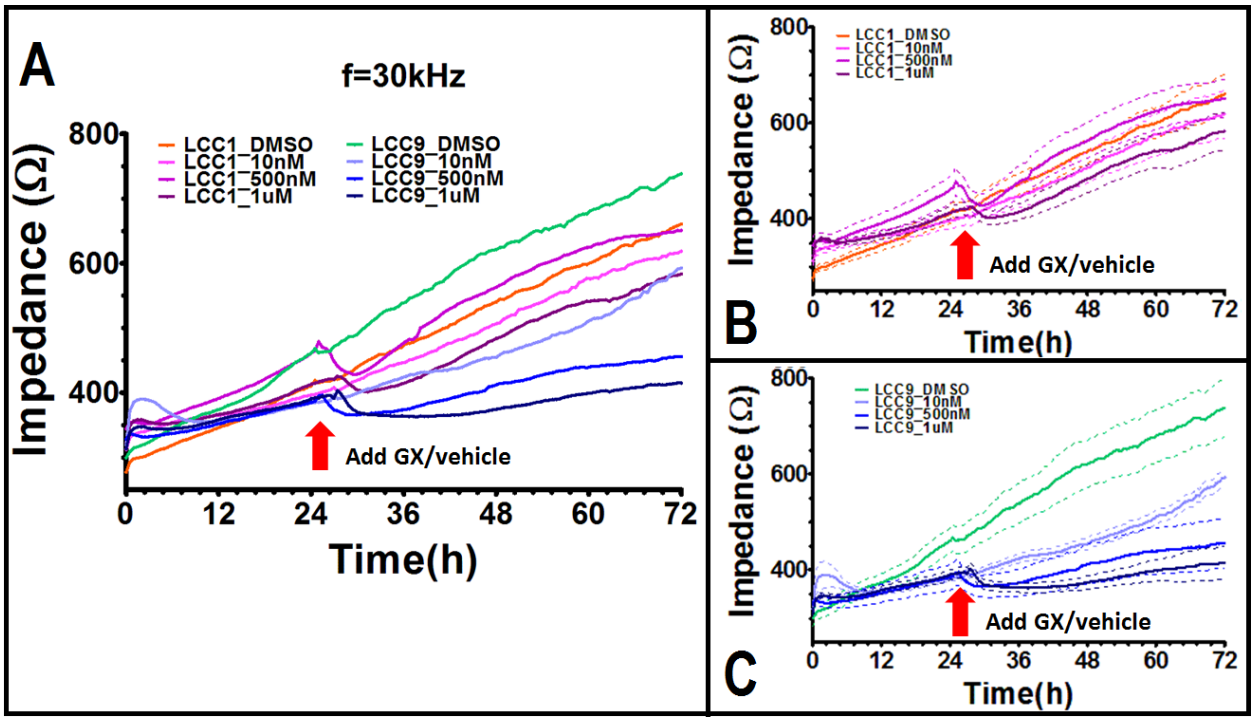

Figure 7.1 (A) Time course of mean values of impedance magnitude at 30 kHz. Plot (A) shown separately for LCC-1 (B) and LCC-9 (C) cells. The range of SEM is shown in dashed lines.

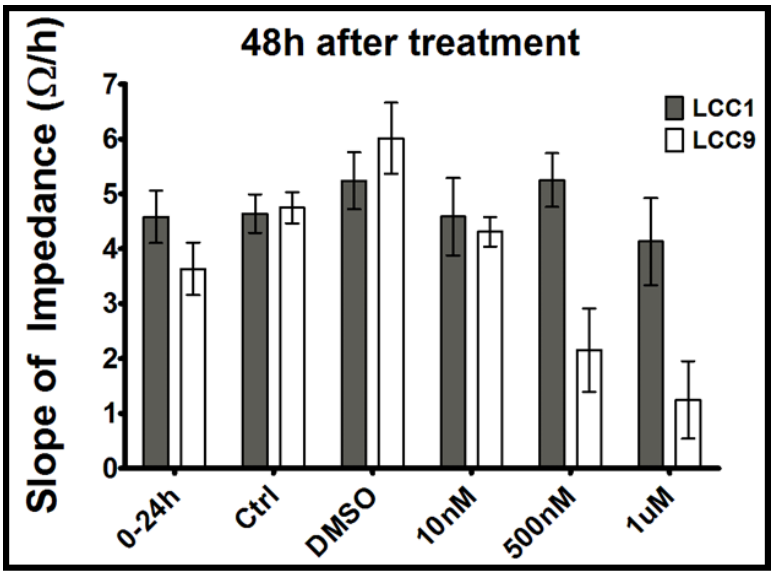

Figure 7.2 Slope of impedance magnitude indicates the effect of GX on LCC-1 and LCC-9 cells.

The effect of the GX on LCC-1 and LCC-9 cells can be quantitatively measured using ECIS data by evaluating the slope of the impedance magnitude over the 48 h time course after the addition of GX. Slopes were calculated from the time point of the lowest impedance value after the introduction of GX, till the end point of experiment. **Figure 7.2** summarizes the slope values obtained from all electrodes in n=6 experiments. Two controls were used, one with no drug

additions, another with vehicle (DMSO). The growth rate of LCC-9 cells in the first 24 hours is slightly lower than LCC-1 cells which is also observed during standard cell propagation. The lower concentration of 10 nM GX does not have a significant effect on the LCC-9 cell population even after 48 hours. This is inferred from similar slope changes for both LCC-1 and LCC-9 cells in electrodes representing control, DMSO and 10nM GX conditions. However, both 500nM and 1μM GX result in a significant decrease in the slope of electrodes with LCC-9 cells compared to LCC-1 as well as control LCC-9. This indicates a significant decrease in the cell density on the electrodes for these conditions which is in agreement with previously published data [223].

ECIS can provide quantitative measurements of the changes in cell morphology and density occurring due to cell growth or cell detachment/cell death. Hence, this technique can be used to perform dose dependency and efficacy studies when evaluating pharmaceutical agents. Here, we used impedance measurements to evaluate the effect of GX on a breast cancer cell model representing hormone therapy sensitive and resistant cells.

7.3. Single-cell biophysical measurements via microfluidics

7.3.1. Experiments

The microfluidics assay shown in chapter 6. was used to probe individual cells passing through a narrow constriction region (8X8 μm). Impedance signals were recorded by an electrode pair in the channel at seven frequencies (1 kHz, 10 kHz, 25 kHz, 50 kHz, 75 kHz, 100 kHz, 800 kHz, 1 MHz) simultaneously. LCC-1 and LCC-9 cells with passage number 18 were used. All data shown were obtained from a single device and experiment. The cells were treated with GX (10 nM) for 48h prior to the experiment. The device was flushed with DI water continuously for 5 minutes between different cell lines and/or conditions. . The transit time of the cells through the constriction channel and the cell bioelectrical properties (specific membrane capacitance, interface resistance) were obtained by analysis of the multi-frequency impedance data using MATLAB scripts. All statistical tests were done in MATLAB and p-values were obtained using non-parametric Kruskal-Walis test to compare different groups.

7.3.2. Results

The impedance recorded at eight frequencies was used to extract electrical circuit parameters using curve fitting as described in section 6.3.3. **Figure 7.3** shows the specific membrane capacitance and interface resistance of LCC-1 and LCC-9 cells obtained from curve fitting.

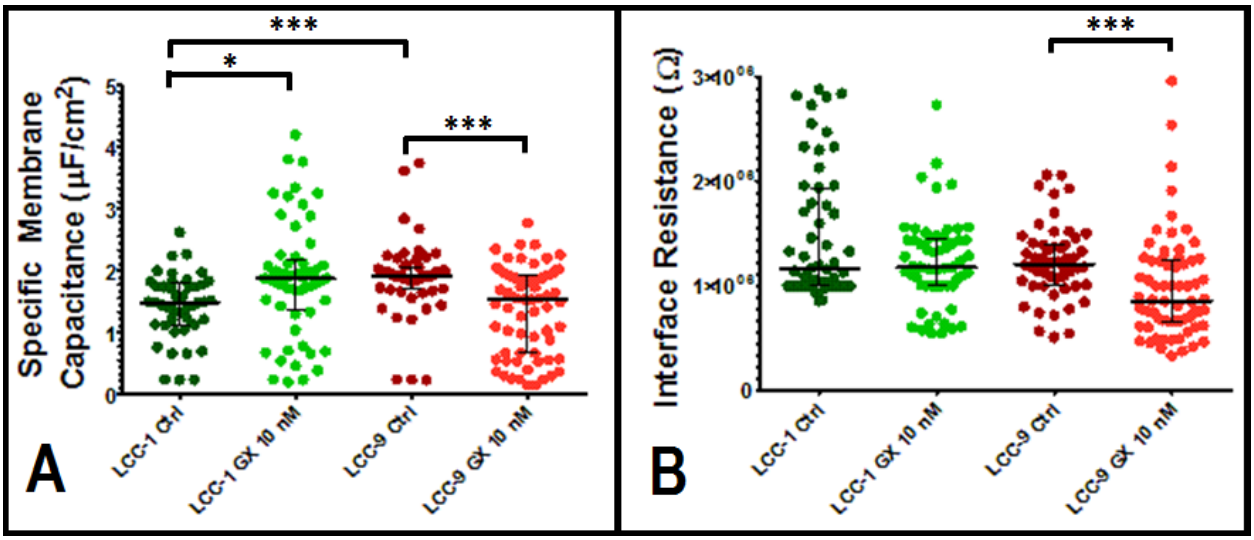

Figure 7.3 Specific membrane capacitance and interface resistance of individual control and GX (10 nM) treated LCC-1 and LCC-9 cells. Bars indicate median with interquartile range. * $P<0.05$ and *** $P<0.001$.

The control LCC-9 cell population has a larger specific membrane capacitance than in LCC-1 cells. This parameter is dependent on membrane composition and structure. One possible source of variation could be the Bcl-2 family of proteins which is overexpressed in LCC-9 cells and localized in the cell membrane (see supplementary figure 1 in [223]). However, detailed investigation of the lipid composition of the membranes and surface charge, ion channel activity needs to be performed to identify the exact cause of increased capacitance seen in the hormone therapy resistant LCC-9 cells. Further, the LCC-9 cells upon treatment with GX (10nM for 48h) display decreased specific membrane capacitance than the control cells. Since, apoptotic cells have leaky plasma membranes, the decrease in capacitance might be an indicator that these cells are pre-apoptotic and have compromised cell membranes. LCC-1 cells exposed to obatoclax had an slightly increased expression of Annexin-V (see supplementary figure 2 in [223]). Annexins are localized in plasma membranes due to their ability to bind to phospholipids and regulated by Ca^{2+} ions. This might be the reason for the increase in the specific membrane capacitance of the LCC-1 cells after treatment with GX.

Interface resistance is the resistance in the electric circuit model between the cell and the constriction channel wall. LCC-9 cells have significantly lower values of interface resistance upon treatment with GX as seen in **Figure 7.3**. This indicates changes in the surface properties of the cell and its interactions with the channel wall. Annexin-V is overexpressed in LCC-9 cells and its

binding to the plasma membrane translocates phosphatidylserine (PS) from the inner to the outer leaflet of the plasma membrane [224]. This could change the surface properties of GX-treated LCC-9 cells and their friction with the channel wall.

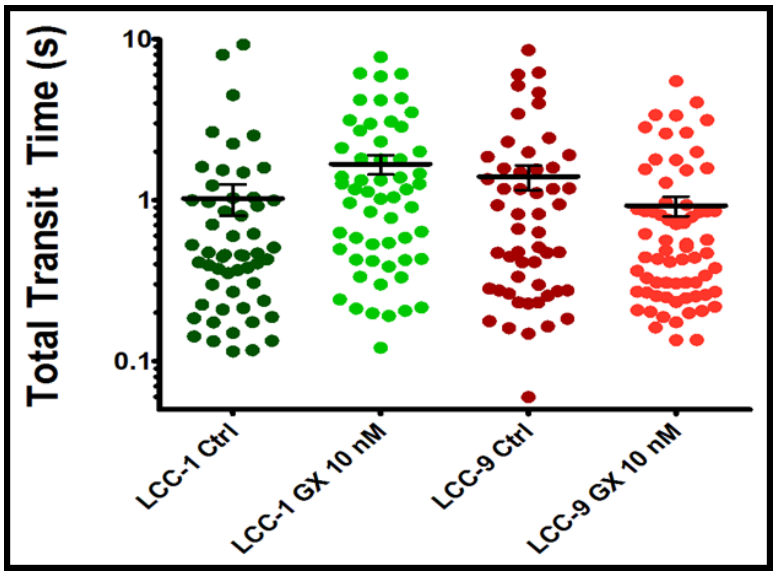

Figure 7.4 Total transit time of cells through the constriction channel. Bars indicate median with interquartile range.

The total transit time of individual cells through a narrow constriction region (8X8 µm) was obtained from impedance signals recorded by an electrode pair in the channel and is an indicator of cell deformability. LCC-9 cells move through the deformation channel faster upon treatment with GX as seen in **Figure 7.4** in comparison with the control cells. Decreased friction between these cells and the channel wall could explain the lower transit times observed. This would also be consistent with the decrease in interface resistance seen in **Figure 7.3**.

7.4. Conclusion

Single cell biophysical characterization was performed on LCC-1 and LCC-9 cells and their response to GX (10 nM) was examined. Our results indicate that this assay is suitable for evaluating non-toxic concentrations of pharmaceutical agents on individual cells. In addition, results from the assay can aid further investigation in identifying the mechanism of drug action.

8. Summary and Outlook

This dissertation aims to expand our fundamental understanding of the bioelectrical properties of breast cancer cells. In addition, miniaturized sensors employing bioimpedance technology have been developed and optimized to improve sensitivity and ability to differentiate between critically important subtypes of breast cancer. The following provides a summary of the research conducted and significant outcomes.

Chapter 3. Microelectrode bioimpedance analysis distinguishes basal and claudin-low subtypes of triple negative breast cancer cells

Triple negative breast cancer (TNBC) is highly aggressive and has a poor prognosis when compared to other molecular subtypes. In particular, the claudin-low subtype of TNBC exhibits tumor-initiating/cancer stem cell like properties. Here, we sought to find new biomarkers to discriminate different forms of TNBC by characterizing their bioimpedance. A customized bioimpedance sensor with four identical branched microelectrodes with branch widths adjusted to accommodate spreading of individual cells was fabricated on silicon and pyrex/glass substrates. Cell analyses were performed on the silicon devices which showed somewhat improved inter-electrode and intra-device reliability. We performed detailed analysis of the bioimpedance spectra of four TNBC cell lines, comparing the peak magnitude, peak frequency and peak phase angle between claudin-low TNBC subtype represented by MDA-MB-231 and Hs578T with that of two basal cells types, the TNBC MDA-MB-468, and an immortalized non-malignant basal breast cell line, MCF-10A. The claudin-low TNBC cell lines showed significantly higher peak frequencies and peak phase angles than the basal cell lines providing evidence that these bioelectrical properties might be useful in distinguishing the clinically significant claudin-low subtype of TNBC.

Chapter 4. A comparative study of nano-scale coatings on gold electrodes for bioimpedance studies of breast cancer cells

The relative sensitivity of standard gold microelectrodes for electric cell-substrate impedance sensing was compared with that of gold microelectrodes coated with gold nanoparticles, carbon nanotubes, or electroplated gold to introduce nano-scale roughness on the surface of the electrodes. For biological solutions, the electroplated gold coated electrodes had significantly higher sensitivity to changes in conductivity than electrodes with other coatings. In contrast, the carbon

nanotube coated electrodes displayed the highest sensitivity to MDA-MB-231 metastatic breast cancer cells. There was also a significant shift in the peak frequency of the cancer cell bioimpedance signal based on the type of electrode coating. The results indicate that nano-scale coatings which introduce varying degrees of surface roughness can be used to modulate the frequency dependent sensitivity of the electrodes and optimize electrode sensitivity for different bioimpedance sensing applications.

Chapter 5. A high-throughput, reconfigurable electrode array for bioimpedance spectroscopy

Bioimpedance spectroscopy is a versatile, label-free method used to monitor real-time events in biological samples with minimal perturbation of the biological system. Applications of this technique frequently require optimization of design and test parameters to obtain improved sensitivities. We developed a system with reconfigurable elements which addresses this need by providing flexibility in the design of electrodes and the acquisition of bioimpedance parameters. A high-throughput electrode array is realized in a multi-well format which serves to increase screening potential and minimize environmental influences as demonstrated through minimal well to well variations. The impedance measurements are made using a setup configured with commercially available and custom components. The flexibility in the system configuration was demonstrated by reconfiguring the device to include nine different electrode designs that were used to systematically study the effect of geometry on impedance measurements from breast cancer cells and by varying excitation voltages applied within the same device. Characterization of the platform was performed using standard biological solutions and varying cell concentration to evaluate system performance. Our reconfigurable system displays the reproducibility, sensitivity, and versatility that are requisite traits of next-generation instrumentation in bioimpedance spectroscopy.

Chapter 6. Microfluidic approach to high-content single-cell analysis of biophysical heterogeneity

Malignant tumors embody heterogeneous cell populations. The properties of single cells within tumors are now recognized to critically impact tumor pathophysiology, patient prognosis, and response to therapy. Here, we report a microfluidic approach to single-cell biophysical profiling of heterogeneity within cell populations based on individual cell biomechanical-bioelectrical properties. The instrumentation consists of parallel microelectrodes embedded within

a PDMS chip which acquire automated biophysical measurements from individual cells as they are subjected to deformation stress imposed by entry and travel through an 8x8 μm constriction channel. Single cell impedance at 10 kHz, 20 kHz, 100 kHz and 800 kHz is captured simultaneously in real-time. Analysis of biomechanical-biophysical properties of a normal breast cell line and malignant breast cell lines with weak and high metastatic abilities indicated that malignant cells have greater heterogeneity in shape before deformation, constriction entry time and specific membrane capacitance than normal cells. The shift of cells to an increasingly more metastatic phenotype was characterized by a significant decrease in constriction entry time, more rapid shape recovery after deformation, a decrease in channel interface resistance, and an increase in specific membrane capacitance. Complex impedance changes at 800 kHz were sufficient to assign individual cells to their respective normal, low metastatic, or highly metastatic cell line with 87.5% accuracy. In conclusion, we demonstrate a biomechanical-bioelectrical profiling method in human breast cell lines that has predictive value in identifying metastatic breast tumor cells. This has potential application to evaluation of metastatic risk in human breast disease.

Chapter 7. Biophysical characterization of a hormone therapy resistant breast cancer cell model

Hormone therapy is a commonly used adjuvant treatment used to prevent recurrence of breast cancer in patients. However, many patients develop resistance to hormone therapy over time after being exposed to anti-hormone pharmaceuticals. In order to improve our understanding of hormone therapy resistance, the LCC-9 cell line was developed by exposing MCF-7 (ER+) cells to the anti-hormone drug Faslodex (ICI). We used the LCC-9 cell line as a model for hormone therapy resistant breast cancer and LCC-1, a genetically related variant, as its hormone therapy sensitive counterpart and examined their bioelectrical responses to the drug Obatoclax (GX). ECIS studies revealed that the slope of the impedance magnitude captures the increased sensitivity of the LCC-9 cells to GX which correlates with cell density measurements obtained previously. The single-cell microfluidic assay captures the bioelectrical differences between LCC-1 and LCC-9 cells as an increased membrane capacitance in the LCC-9 cells. Further, GX results in a significant decrease in the membrane capacitance even when a non-toxic concentration of GX (10 nM) is applied to the LCC-9 cells. This suggests that the onset of apoptosis is triggered even with very low concentrations of the drug. Our results demonstrate the promise of bioimpedance techniques

in monitoring the effect of pharmaceuticals, identifying optimal dose and narrowing down the mechanism of action in cells.

8.1. Significance of contribution

Bioimpedance presents an economical and simple means of monitoring biological cells and their responses to various stimuli. Previously, we attempted to detect the presence of breast cancer cells using the anti-cancer agent Vorinostat in a simulated breast cancer biopsy model. This work aims to improve our understanding of the bioimpedance spectra of various breast cancer cell lines which could ultimately translate to the use of these types of measurements for the identification and discrimination of critical subtypes of breast cancer in biopsies obtained from patients. We investigated a panel of triple negative breast cancer (TNBC) cell lines comprised of basal and claudin-low subtypes, and identified unique differentiators acquired using ECIS-based impedance spectroscopy. We also examined a hormone therapy resistant model of breast cancer (LCC-1 and LCC-9) and showed differential bioimpedance responses to an anti-cancer agent Obatoclax. This highlights the promise this technology holds for the easy determination of patient response to pharmaceuticals. Further, the electronic readout of results facilitates the development of algorithms to predict subtype and sensitivity to drugs and eliminates human error as well as the need for trained personnel in decision making. As part of our effort to realize this vision of the clinical use of bioimpedance spectroscopy, we also pursued the development of miniaturized bioimpedance sensors that have the requisite traits of reliability, ease-of-use, low-cost and disposability. Two generations of bioimpedance sensors were developed. In the first generation, a single-well biosensor with four identical branched electrodes was developed. Our experiments on these devices highlighted the need to increase screening potential in order to evaluate physical design factors, biological samples and dose dependency under identical environmental conditions for the optimization of application specific bioimpedance sensors. This led to the development of a reconfigurable, wafer-level sensor with a 6X6 array of microelectrodes and supporting instrumentation to make reliable bioimpedance measurements using this device. We also developed a microfluidic biosensor that is capable of evaluating bioimpedance changes in response to mechanical stress. This sensor addresses the need to examine cell biophysical properties at the single-cell level in order to evaluate heterogeneity in the tumor cell populations. Finally, we explored two different strategies to improve the sensitivity of the microelectrodes to bioimpedance measurements from breast cancer cells. First, we used nano-scale coatings of gold nanoparticles,

carbon nanotubes and electroplated gold on the surface of the electrode, which resulted in maximum sensitivity improvement of 2.5X in carbon nanotube coated electrodes. Second, we explored the effect of design parameters in a branched electrode geometry, where we showed that branch width played a more significant role in electrode sensitivity and a width of 25 µm was identified as optimal. Below is a diagram representation of key contributions made by this dissertation.

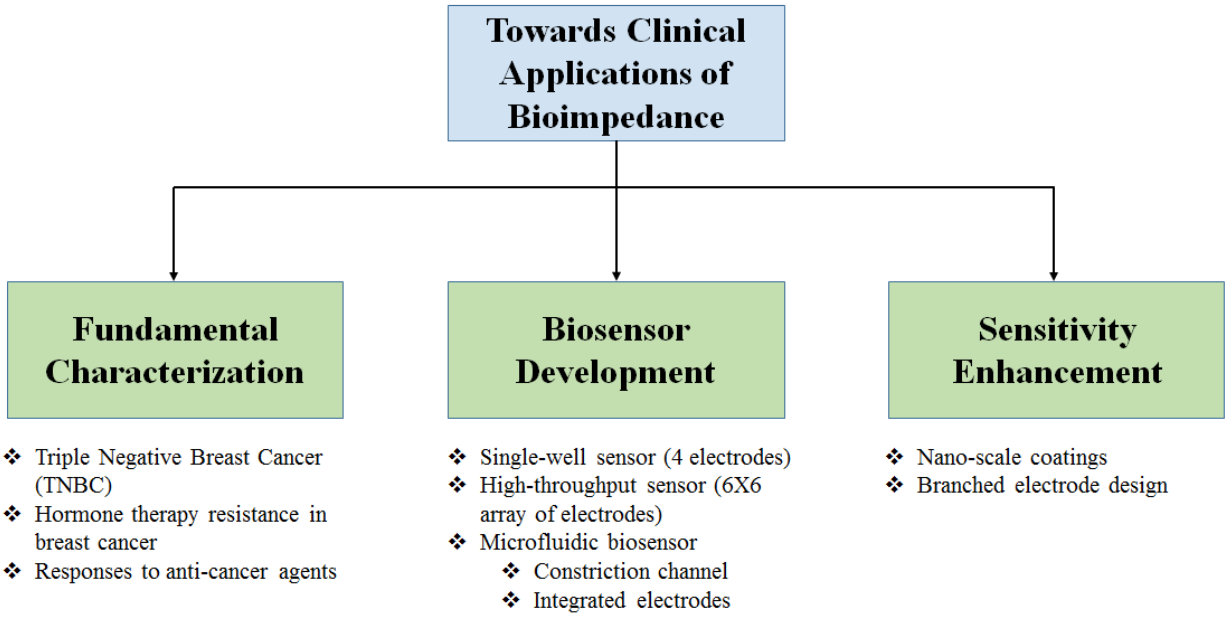

Figure 8.1 Summary of key contributions to bioimpedance technology made by this dissertation.

8.2. Future directions

This dissertation makes significant advances on the optimization of bioimpedance devices and characterization of critical subtypes of breast cancer. However, there are a number of research avenues that can be pursued in the development of bioimpedance technologies towards clinical use. The comprehensive characterization of bioimpedance spectra of all subtypes of breast cancer cells to determine unique bioelectrical signatures is a challenging problem. Since bioimpedance is a complex value that is a function of frequency, there are multiple parameters like magnitude, phase, frequency, and real and imaginary impedance that can be considered as candidates to successfully differentiate between different samples. In addition, stimuli such as pharmaceuticals can be used for targeted testing in a high-throughput impedance array to achieve this goal. The use of bioimpedance measurements in high-throughput format to screen compounds for

pharmacological activity and/or efficacy needs to be developed and transferred for use in the pharmaceutical industry. The improvement of electrode sensitivity for bioimpedance measurements is another avenue for research and development. As mentioned before, there is a need for optimization of electrode sensitivity based on the application for effective use of bioimpedance technology. It would also be interesting to study the effect of ordered conductive nano-scale coatings to guide and enhance cell spreading on the electrodes. Other distributed area electrode shapes can also be considered to improve the sensitivity. Finally, more microfluidic biosensors can incorporate electrodes as a detection strategy to be used during/after separation, trapping, mixing or treatments in reactive chambers. This avenue probably holds the most promise for translation of this technology to the clinic. In addition, these electrodes can be coated with antibodies or other bio-recognition elements to improve their selectivity to the biological analyte of interest.

9. References

[1] Martinsen OG, Grimnes S. Bioimpedance and bioelectricity basics: Academic press; 2011.

[2] Timberlake KC. Chemistry: An introduction to general, organic, and biological chemistry: Pearson Higher Ed; 2014.

[3] Lodish H, Berk A, Zipursky SL, Matsudaira P, Baltimore D, Darnell J. Molecular Cell Biology. 4th ed. New York: W. H. Freeman; 2000.

[4] Mazzanti M, Bustamante JO, Oberleithner H. Electrical dimension of the nuclear envelope. Physiological Reviews. 2001;81:1-19.

[5] Schwan HP. The practical success of impedance techniques from an historical perspective. Annals of the New York Academy of Sciences. 1999;873:1-12.

[6] Kyle UG, Bosaeus I, De Lorenzo AD, Deurenberg P, Elia M, Gómez JM, et al. Bioelectrical impedance analysis—part I: review of principles and methods. Clinical nutrition. 2004;23:1226-43.

[7] Jaffrin MY, Morel H. Body fluid volumes measurements by impedance: A review of bioimpedance spectroscopy (BIS) and bioimpedance analysis (BIA) methods. Medical engineering & physics. 2008;30:1257-69.

[8] Khalil SF, Mohktar MS, Ibrahim F. The theory and fundamentals of bioimpedance analysis in clinical status monitoring and diagnosis of diseases. Sensors. 2014;14:10895-928.

[9] Kyle UG, Bosaeus I, De Lorenzo AD, Deurenberg P, Elia M, Gómez JM, et al. Bioelectrical impedance analysis—part II: utilization in clinical practice. Clinical nutrition. 2004;23:1430-53.

[10] Bioelectrical impedance analysis in body composition measurement: program and abstracts, December 12-14: National Institutes of Health; 1994.

[11] Barbosa-Silva MCG, Barros AJ. Bioelectrical impedance analysis in clinical practice: a new perspective on its use beyond body composition equations. Current Opinion in Clinical Nutrition & Metabolic Care. 2005;8:311-7.

[12] Rutkove SB, Aaron R, Shiffman CA. Localized bioimpedance analysis in the evaluation of neuromuscular disease. Muscle & nerve. 2002;25:390-7.

[13] Lukaski H. Regional bioelectrical impedance analysis: applications in health and medicine. Acta diabetologica. 2003;40:s196-s9.

[14] Zlochiver S, Arad M, Radai M, Barak-Shinar D, Krief H, Engelman T, et al. A portable bio-impedance system for monitoring lung resistivity. Medical engineering & physics. 2007;29:93-100.

[15] Toso S, Piccoli A, Gusella M, Menon D, Bononi A, Crepaldi G, et al. Altered tissue electric properties in lung cancer patients as detected by bioelectric impedance vector analysis. Nutrition. 2000;16:120-4.

[16] Wegener J, Keese CR, Giaever I. Electric cell-substrate impedance sensing (ECIS) as a noninvasive means to monitor the kinetics of cell spreading to artificial surfaces. Experimental Cell Research. 2000;259:158-66.

[17] Xiao C, Luong JHT. On-line monitoring of cell growth and cytotoxicity using electric cell-substrate impedance sensing (ECIS). Biotechnology Progress. 2003;19:1000-5.

[18] Arndt S, Seebach J, Psathaki K, Galla HJ, Wegener J. Bioelectrical impedance assay to monitor changes in cell shape during apoptosis. Biosensors & Bioelectronics. 2004;19:583-94.

[19] Asphahani F, Thein M, Veiseh O, Edmondson D, Kosai R, Veiseh M, et al. Influence of cell adhesion and spreading on impedance characteristics of cell-based sensors. Biosensors & Bioelectronics. 2008;23:1307-13.

[20] Liu QJ, Yu JJ, Xiao L, Tang JCO, Zhang Y, Wang P, et al. Impedance studies of bio-behavior and chemosensitivity of cancer cells by micro-electrode arrays. Biosensors & Bioelectronics. 2009;24:1305-10.

[21] Arias LR, Perry CA, Yang LJ. Real-time electrical impedance detection of cellular activities of oral cancer cells. Biosensors & Bioelectronics. 2010;25:2225-31.

[22] Ghenim L, Kaji H, Hoshino Y, Ishibashi T, Haguet V, Gidrol X, et al. Monitoring impedance changes associated with motility and mitosis of a single cell. Lab on a Chip. 2010;10:2546-50.

[23] Luong JH, Habibi-Rezaei M, Meghrous J, Xiao C, Male KB, Kamen A. Monitoring motility, spreading, and mortality of adherent insect cells using an impedance sensor. Analytical chemistry. 2001;73:1844-8.

[24] Giaever I, Keese CR. Micromotion of mammalian-cells measured electrically. Proceedings of the National Academy of Sciences of the United States of America. 1993;90:1634-.

[25] Heijink IH, Brandenburg SM, Noordhoek JA, Postma DS, Slebos DJ, van Oosterhout AJM. Characterisation of cell adhesion in airway epithelial cell types using electric cell-substrate impedance sensing. European Respiratory Journal. 2010;35:894-903.

[26] Liu CL, Tam JCW, Sanders AJ, Jiang DG, Ko CH, Fung KP, et al. Electric Cell-Substrate Impedance Sensing as a Screening Tool for Wound Healing Agents. Electric Cell-Substrate Impedance Sensing and Cancer Metastasis: Springer; 2012. p. 203-16.

[27] Wegener J, Keese CR, Giaever I. Recovery of adherent cells after in situ electroporation monitored electrically. Biotechniques. 2002;33:348-+.

[28] Stolwijk JA, Hartmann C, Balani P, Albermann S, Keese CR, Giaever I, et al. Impedance analysis of adherent cells after in situ electroporation: non-invasive monitoring during intracellular manipulations. Biosensors and Bioelectronics. 2011;26:4720-7.

[29] Xu Y, Yao H, Wang L, Xing W, Cheng J. The construction of an individually addressable cell array for selective patterning and electroporation. Lab on a Chip. 2011;11:2417-23.

[30] Saleh O, Sohn L. Quantitative sensing of nanoscale colloids using a microchip Coulter counter. Review of Scientific Instruments. 2001;72:4449-51.

[31] Zhe J, Jagtiani A, Dutta P, Hu J, Carletta J. A micromachined high throughput Coulter counter for bioparticle detection and counting. Journal of Micromechanics and Microengineering. 2007;17:304.

[32] Sun T, Morgan H. Single-cell microfluidic impedance cytometry: a review. Microfluidics and Nanofluidics. 2010;8:423-43.

[33] Gawad S, Schild L, Renaud P. Micromachined impedance spectroscopy flow cytometer for cell analysis and particle sizing. Lab on a Chip. 2001;1:76-82.

[34] Gawad S, Sun T, Green NG, Morgan H. Impedance spectroscopy using maximum length sequences: Application to single cell analysis. Review of Scientific Instruments. 2007;78:054301.

[35] Heileman K, Daoud J, Tabrizian M. Dielectric spectroscopy as a viable biosensing tool for cell and tissue characterization and analysis. Biosensors & Bioelectronics. 2013;49:348-59.

[36] Cheung K, Gawad S, Renaud P. Impedance spectroscopy flow cytometry: On-chip label-free cell differentiation. Cytometry Part A. 2005;65A:124-32.

[37] Du E, Ha S, Diez-Silva M, Dao M, Suresh S, Chandrakasan AP. Electric impedance microflow cytometry for characterization of cell disease states. Lab on a chip. 2013;13:3903-9.

[38] Han A, Yang L, Frazier AB. Quantification of the heterogeneity in breast cancer cell lines using whole-cell impedance spectroscopy. Clinical Cancer Research. 2007;13:139-43.

[39] Huh D, Gu W, Kamotani Y, Grotberg JB, Takayama S. Microfluidics for flow cytometric analysis of cells and particles. Physiological measurement. 2005;26:R73.

[40] Lan KC, Jang LS. Integration of single-cell trapping and impedance measurement utilizing microwell electrodes. Biosensors & Bioelectronics. 2011;26:2025-31.

[41] Chen J, Zheng Y, Tan QY, Shojaei-Baghini E, Zhang YL, Li J, et al. Classification of cell types using a microfluidic device for mechanical and electrical measurement on single cells. Lab on a Chip. 2011;11:3174-81.

[42] Chen J, Xue C, Zhao Y, Chen D, Wu M-H, Wang J. Microfluidic Impedance Flow Cytometry Enabling High-Throughput Single-Cell Electrical Property Characterization. International Journal of Molecular Sciences. 2015;16:9804-30.

[43] Zhao Y, Zhao X, Chen D, Luo Y, Jiang M, Wei C, et al. Tumor cell characterization and classification based on cellular specific membrane capacitance and cytoplasm conductivity. Biosensors and Bioelectronics. 2014;57:245-53.

[44] Adamo A, Sharei A, Adamo L, Lee B, Mao S, Jensen KF. Microfluidics-Based Assessment of Cell Deformability. Analytical Chemistry. 2012;84:6438-43.

[45] Lisdat F, Schäfer D. The use of electrochemical impedance spectroscopy for biosensing. Analytical and bioanalytical chemistry. 2008;391:1555-67.

[46] Pei R, Cheng Z, Wang E, Yang X. Amplification of antigen–antibody interactions based on biotin labeled protein–streptavidin network complex using impedance spectroscopy. Biosensors and Bioelectronics. 2001;16:355-61.

[47] Patolsky F, Katz E, Bardea A, Willner I. Enzyme-linked amplified electrochemical sensing of oligonucleotide-DNA interactions by means of the precipitation of an insoluble product and using impedance spectroscopy. Langmuir. 1999;15:3703-6.

[48] Wang J. Electrochemical nucleic acid biosensors. Analytica chimica acta. 2002;469:63-71.

[49] Arya SK, Lee KC, Bin Dah'alan D, Daniel, Rahman ARA. Breast tumor cell detection at single cell resolution using an electrochemical impedance technique. Lab on a Chip. 2012;12:2362-8.

[50] Venkatanarayanan A, Keyes TE, Forster RJ. Label-free impedance detection of cancer cells. Analytical chemistry. 2013;85:2216-22.

[51] Heller A, Feldman B. Electrochemical glucose sensors and their applications in diabetes management. Chemical Reviews. 2008;108:2482-505.

[52] Ho WO, Krause S, McNeil CJ, Pritchard JA, Armstrong RD, Athey D, et al. Electrochemical sensor for measurement of urea and creatinine in serum based on ac impedance measurement of enzyme-catalyzed polymer transformation. Analytical Chemistry. 1999;71:1940-6.

[53] Keefer EW, Botterman BR, Romero MI, Rossi AF, Gross GW. Carbon nanotube coating improves neuronal recordings. Nature Nanotechnology. 2008;3:434-9.

[54] Abdolahad M, Taghinejad M, Taghinejad H, Janmaleki M, Mohajerzadeh S. A vertically aligned carbon nanotube-based impedance sensing biosensor for rapid and high sensitive detection of cancer cells. Lab on a Chip. 2012;12:1183-90.

[55] Baranauskas G, Maggiolini E, Castagnola E, Ansaldo A, Mazzoni A, Angotzi GN, et al. Carbon nanotube composite coating of neural microelectrodes preferentially improves the multiunit signal-to-noise ratio. Journal of Neural Engineering. 2011;8:12.

[56] Elshafey R, Tavares AC, Siaj M, Zourob M. Electrochemical impedance immunosensor based on gold nanoparticles–protein G for the detection of cancer marker epidermal growth factor receptor in human plasma and brain tissue. Biosensors and Bioelectronics. 2013;50:143-9.

[57] Zhang HN, Shih J, Zhu J, Kotov NA. Layered Nanocomposites from Gold Nanoparticles for Neural Prosthetic Devices. Nano Letters. 2012;12:3391-8.

[58] Hrapovic S, Majid E, Liu Y, Male K, Luong JHT. Metallic nanoparticle-carbon nanotube composites for electrochemical determination of explosive nitroaromatic compounds. Analytical Chemistry. 2006;78:5504-12.

[59] DeSantis C, Ma J, Bryan L, Jemal A. Breast cancer statistics, 2013. CA: a cancer journal for clinicians. 2014;64:52-62.

[60] Siegel RL, Miller KD, Jemal A. Cancer statistics, 2015. CA: a cancer journal for clinicians. 2015;65:5-29.

[61] Dunnwald LK, Rossing MA, Li CI. Hormone receptor status, tumor characteristics, and prognosis: a prospective cohort of breast cancer patients. Breast Cancer Res. 2007;9:R6.

[62] Romero A, Prat A, García-Sáenz JÁ, del Prado N, Pelayo A, Furió V, et al. Assignment of tumor subtype by genomic testing and pathologic-based approximations: implications on patient's management and therapy selection. Clinical and Translational Oncology. 2013.

[63] Hong JL, Lan KC, Jang LS. Electrical characteristics analysis of various cancer cells using a microfluidic device based on single-cell impedance measurement. Sensors and Actuators B-Chemical. 2012;173:927-34.

[64] Kang G, Yoo SK, Kim HI, Lee JH. Differentiation Between Normal and Cancerous Cells at the Single Cell Level Using 3-D Electrode Electrical Impedance Spectroscopy. Ieee Sensors Journal. 2012;12:1084-9.

[65] Yang LJ, Arias LR, Lane TS, Yancey MD, Mamouni J. Real-time electrical impedance-based measurement to distinguish oral cancer cells and non-cancer oral epithelial cells. Anal Bioanal Chem. 2011;399:1823-33.

[66] Cho Y, Kim HS, Frazier AB, Chen ZG, Shin DM, Han A. Whole-Cell Impedance Analysis for Highly and Poorly Metastatic Cancer Cells. Journal of Microelectromechanical Systems. 2009;18:808-17.

[67] Tran TB, Cho S, Min J. Hydrogel-based diffusion chip with Electric Cell-substrate Impedance Sensing (ECIS) integration for cell viability assay and drug toxicity screening. Biosensors and Bioelectronics. 2013;50:453-9.

[68] Said R, Aykut Ü. A real-time electrical impedance based technique to measure invasion of endothelial cell monolayer by cancer cells. Journal of Visualized Experiments. 2011.

[69] Han KH, Han A, Frazier AB. Microsystems for isolation and electrophysiological analysis of breast cancer cells from blood. Biosensors & Bioelectronics. 2006;21:1907-14.

[70] Asphahani F, Wang K, Thein M, Veiseh O, Yung S, Xu JA, et al. Single-cell bioelectrical impedance platform for monitoring cellular response to drug treatment. Physical Biology. 2011;8.

[71] Patani N, Douglas-Jones A, Mansel R, Jiang W, Mokbel K. Tumour suppressor function of MDA-7/IL-24 in human breast cancer. Cancer Cell International. 2010;10:9.

[72] Gupta D, Lammersfeld CA, Vashi PG, King J, Dahlk SL, Grutsch JF, et al. Bioelectrical impedance phase angle as a prognostic indicator in breast cancer. Bmc Cancer. 2008;8:7.

[73] Gupta D, Lammersfeld CA, Vashi PG, King J, Dahlk SL, Grutsch JF, et al. Bioelectrical impedance phase angle in clinical practice: implications for prognosis in stage IIIB and IV non-small cell lung cancer. BMC cancer. 2009;9:37.

[74] Gupta D, Lis CG, Dahlk SL, King J, Vashi PG, Grutsch JF, et al. The relationship between bioelectrical impedance phase angle and subjective global assessment in advanced colorectal cancer. Nutrition Journal. 2008;7:6.

[75] Rahman ARA, Lo CM, Bhansali S. A Detailed Model for High-Frequency Impedance Characterization of Ovarian Cancer Epithelial Cell Layer Using ECIS Electrodes. Ieee Transactions on Biomedical Engineering. 2009;56:485-92.

[76] Malleo D, Nevill JT, Lee LP, Morgan H. Continuous differential impedance spectroscopy of single cells. Microfluidics and nanofluidics. 2010;9:191-8.

[77] Abdolahad M, Janmaleki M, Taghinejad M, Taghnejad H, Salehi F, Mohajerzadeh S. Single-cell resolution diagnosis of cancer cells by carbon nanotube electrical spectroscopy. Nanoscale. 2013;5:3421-7.

[78] Abdolahad M, Shashaani H, Janmaleki M, Mohajerzadeh S. Silicon nanograss based impedance biosensor for label free detection of rare metastatic cells among primary cancerous colon cells, suitable for more accurate cancer staging. Biosensors and Bioelectronics. 2014;59:151-9.

[79] Hong J-L, Lan K-C, Jang L-S. **Electrical characteristics analysis of various cancer cells using a microfluidic device based on single-cell impedance measurement**. Sensors and Actuators B: Chemical. 2012;173:927–34.

[80] Zhao Y, Chen D, Li H, Luo Y, Deng B, Huang S-B, et al. A microfluidic system enabling continuous characterization of specific membrane capacitance and cytoplasm conductivity of single cells in suspension. Biosensors and Bioelectronics. 2013;43:304-7.

[81] Zhao Y, Chen D, Luo Y, Li H, Deng B, Huang S-B, et al. A microfluidic system for cell type classification based on cellular size-independent electrical properties. Lab on a Chip. 2013;13:2272-7.

[82] Srinivasaraghavan V, Strobl J, Agah M. Bioimpedance rise in response to histone deacetylase inhibitor is a marker of mammary cancer cells within a mixed culture of normal breast cells. Lab on a Chip. 2012;12:5168-79.

[83] Srinivasaraghavan V, Strobl J, Agah M. Chemical induced impedance spectroscopy for single cancer cell detection. Solid-State Sensors, Actuators and Microsystems Conference (Transducers). Beijing, China2011. p. 2247-50.

[84] Srinivasaraghavan V, Strobl J, Agah M. Detection of breast cancer cells in tri-culture using impedance spectroscopy. 15th International Conference on Miniaturized Systems for Chemistry and Life Sciences. Seattle, WA: Royal Society of Chemistry; 2011. p. 1713-5.

[85] Giaever I, Keese CR. Monitoring fibroblast behavior in tissue-culture with an applied electric-field. Proceedings of the National Academy of Sciences of the United States of America-Biological Sciences. 1984;81:3761-4.

[86] Mitra P, Keese CR, Giaever I. ELECTRIC MEASUREMENTS CAN BE USED TO MONITOR THE ATTACHMENT AND SPREADING OF CELLS IN TISSUE-CULTURE. Biotechniques. 1991;11:504-&.

[87] Giaever I, Keese CR. MICROMOTION OF MAMMALIAN-CELLS MEASURED ELECTRICALLY (PROC NATL ACAD SCI USA, VOL 88, PG 7896, 1991). Proceedings of the National Academy of Sciences of the United States of America. 1993;90:1634-.

[88] Vistejnova L, Dvorakova J, Hasova M, Muthny T, Velebny V, Soucek K, et al. The comparison of impedance-based method of cell proliferation monitoring with commonly used metabolic-based techniques. Neuroendocrinology Letters. 2009;30:121-7.

[89] Otto AM, Brischwein M, Motrescu E, Wolf B. Analysis of drug action on tumor cell metabolism using electronic sensor chips. Archiv Der Pharmazie. 2004;337:682-6.

[90] Dittami GM, Ayliffe HE, King CS, Rabbitt RD. A multilayer MEMS platform for single-cell electric impedance spectroscopy and electrochemical analysis. Journal of Microelectromechanical Systems. 2008;17:850-62.

[91] Kurz CV, Buth H, Sossalla A, Vermeersch V, Toncheva V, Dubruel P, et al. Chip-based impedance measurement on single cells for monitoring sub-toxic effects on cell membranes. Biosensors & Bioelectronics. 2011;26:3405-12.

[92] Morgan H, Sun T, Holmes D, Gawad S, Green NG. Single cell dielectric spectroscopy. Journal of Physics D-Applied Physics. 2007;40:61-70.

[93] Han A, Frazier AB. Ion channel characterization using single cell impedance spectroscopy. Lab on a Chip. 2006;6:1412-4.

[94] Qiao GF, Wang W, Duan W, Zheng F, Sinclair AJ, Chatwin CR. Bioimpedance Analysis for the Characterization of Breast Cancer Cells in Suspension. Ieee Transactions on Biomedical Engineering. 2012;59:2321-9.

[95] Hong J-L, Lan K-C, Jang L-S. Electrical characteristics analysis of various cancer cells using a microfluidic device based on single-cell impedance measurement. Sensors and Actuators B: Chemical. 2012;In Press.

[96] Narayanan S, Nikkhah M, Strobl JS, Agah M. Analysis of the passivation layer by testing and modeling a cell impedance micro-sensor. Sensors and Actuators a-Physical. 2010;159:241-7.

[97] Nikkhah M, Strobl JS, De Vita R, Agah M. The cytoskeletal organization of breast carcinoma and fibroblast cells inside three dimensional (3-D) isotropic silicon microstructures. Biomaterials. 2010;31:4552-61.

[98] Barr VA, Bunnell SC. Interference reflectance microscopy. Current Protocols in Cell Biology. 2009;Chapter 4:Unit 4.23.

[99] Srinivasaraghavan V, Strobl J, Agah M. Microelectrode bioimpedance analysis distinguishes basal and claudin-low subtypes of triple negative breast cancer cells. Biomedical microdevices. 2015;17:1-11.

[100] Morimoto T, Kimura S, Konishi Y, Komaki K, Uyama T, Monden Y, et al. A study of the electrical bio-impedance of tumors. Investigative Surgery. 1993;6:25-32.

[101] Cornish B, Chapman M, Hirst C, Mirolo B, Bunce I, Ward L, et al. Early diagnosis of lymphedema using multiple frequency bioimpedance. Lymphology. 2001;34:2-11.

[102] Gregory WD, Marx JJ, Gregory CW, Mikkelson WM, Tjoe JA, Shell J. The Cole relaxation frequency as a parameter to identify cancer in breast tissue. Medical Physics. 2012;39:4167-74.

[103] Heileman K, Daoud J, Tabrizian M. Dielectric spectroscopy as a viable biosensing tool for cell and tissue characterization and analysis. Biosensors and Bioelectronics. 2013;49:348-59.

[104] Pick H, Terrettaz S, Baud O, Laribi O, Brisken C, Vogel H. Monitoring proliferative activities of hormone-like odorants in human breast cancer cells by gene transcription profiling and electrical impedance spectroscopy. Biosensors and Bioelectronics. 2013;50:431-6.

[105] Lo CM, Keese CR, Giaever I. Impedance analysis of MDCK cells measured by electric cell-substrate impedance sensing. Biophysical Journal. 1995;69:2800-7.

[106] Chauveau N, Hamzaoui L, Rochaix P, Rigaud B, Voigt JJ, Morucci JP. Ex vivo discrimination between normal and pathological tissues in human breast surgical biopsies using bioimpedance spectroscopy. Electrical Bioimpedance Methods: Applications to Medicine and Biotechnology. 1999;873:42-50.

[107] Ng EYK, Sree SV, Ng KH, Kaw G. The use of tissue electrical characteristics for breast cancer detection: A perspective review. Technology in Cancer Research & Treatment. 2008;7:295-308.

[108] Raneta O, Bella V, Bellova L, Zamecnikova E. The use of electrical impedance tomography to the differential diagnosis of pathological mammographic/sonographic findings. Neoplasma. 2013;60:647-54.

[109] Jahnke H-G, Heimann A, Azendorf R, Mpoukouvalas K, Kempski O, Robitzki AA, et al. Impedance spectroscopy—An outstanding method for label-free and real-time discrimination between brain and tumor tissue in vivo. Biosensors and Bioelectronics. 2013;46:8-14.

[110] Giaever I, Keese CR. A morphological biosensor for mammalian-cells. Nature. 1993;366:591-2.

[111] Srinivasaraghavan V, Strobl J, Wang D, Heflin JR, Agah M. A comparative study of nano-scale coatings on gold electrodes for bioimpedance studies of breast cancer cells. Biomedical microdevices. 2014:1-8.

[112] Prat A, Parker JS, Karginova O, Fan C, Livasy C, Herschkowitz JI, et al. Phenotypic and molecular characterization of the claudin-low intrinsic subtype of breast cancer. Breast Cancer Research. 2010;12:18.

[113] Choi J, Jung WH, Koo JS. Clinicopathologic features of molecular subtypes of triple negative breast cancer based on immunohistochemical markers. Histology and Histopathology. 2012;27:1481-93.

[114] Gerhard R, Ricardo S, Albergaria A, Gomes M, Silva AR, Logullo AF, et al. Immunohistochemical features of claudin-low intrinsic subtype in metaplastic breast carcinomas. Breast. 2012;21:354-60.

[115] Lu SL, Singh K, Mangray S, Tavares R, Noble L, Resnick MB, et al. Claudin expression in high-grade invasive ductal carcinoma of the breast: correlation with the molecular subtype. Modern Pathology. 2013;26:485-95.

[116] Alexander Jr F, Price DT, Bhansali S. Optimization of interdigitated electrode (IDE) arrays for impedance based evaluation of Hs 578T cancer cells. Journal of Physics: Conference Series: IOP Publishing; 2010. p. 012134.

[117] Rakha EA, Chan S. Metastatic Triple-negative Breast Cancer. Clinical Oncology. 2011;23:587-600.

[118] Hudis CA, Gianni L. Triple-Negative Breast Cancer: An Unmet Medical Need. Oncologist. 2011;16:1-11.

[119] Prat A, Perou CM. Deconstructing the molecular portraits of breast cancer. Molecular Oncology. 2011;5:5-23.

[120] Sarrio D, Franklin CK, Mackay A, Reis JS, Isacke CM. Epithelial and Mesenchymal Subpopulations Within Normal Basal Breast Cell Lines Exhibit Distinct Stem Cell/Progenitor Properties. Stem Cells. 2012;30:292-303.

[121] Neve RM, Chin K, Fridlyand J, Yeh J, Baehner FL, Fevr T, et al. A collection of breast cancer cell lines for the study of functionally distinct cancer subtypes. Cancer Cell. 2006;10:515-27.

[122] Harrell JC, Prat A, Parker JS, Fan C, He XP, Carey L, et al. Genomic analysis identifies unique signatures predictive of brain, lung, and liver relapse. Breast Cancer Research and Treatment. 2012;132:523-35.

[123] Carotenuto P, Roma C, Rachiglio AM, Botti G, D'Alessio A, Normanno N. Triple Negative Breast Cancer: From Molecular Portrait to Therapeutic Intervention. Critical Reviews in Eukaryotic Gene Expression. 2010;20:17-34.

[124] Hennessy BT, Gonzalez-Angulo AM, Stemke-Hale K, Gilcrease MZ, Krishnamurthy S, Lee JS, et al. Characterization of a Naturally Occurring Breast Cancer Subset Enriched in Epithelial-to-Mesenchymal Transition and Stem Cell Characteristics. Cancer Research. 2009;69:4116-24.

[125] Herschkowitz JI, Zhao W, Zhang M, Usary J, Murrow G, Edwards D, et al. Comparative oncogenomics identifies breast tumors enriched in functional tumor-initiating cells. Proceedings of the National Academy of Sciences of the United States of America. 2012;109:2778-83.

[126] Creighton CJ, Li XX, Landis M, Dixon JM, Neumeister VM, Sjolund A, et al. Residual breast cancers after conventional therapy display mesenchymal as well as tumor-initiating features. Proceedings of the National Academy of Sciences of the United States of America. 2009;106:13820-5.

[127] Heiser LM, Sadanandam A, Kuo WL, Benz SC, Goldstein TC, Ng S, et al. Subtype and pathway specific responses to anticancer compounds in breast cancer. Proceedings of the National Academy of Sciences of the United States of America. 2012;109:2724-9.

[128] Ricardo S, Gerhard R, Cameselle-Teijeiro JF, Schmitt F, Paredes J. Claudin expression in breast cancer: High or low, what to expect? Histology and Histopathology. 2012;27:1283-95.

[129] Chavez KJ, Garimella SV, Lipkowitz S. Triple negative breast cancer cell lines: One tool in the search for better treatment of triple negative breast cancer. Breast Disease. 2011;32:35-48.

[130] Walia V, Yu Y, Cao D, Sun M, McLean JR, Hollier BG, et al. Loss of breast epithelial marker hCLCA2 promotes epithelial-to-mesenchymal transition and indicates higher risk of metastasis. Oncogene. 2012;31:2237-46.

[131] Gupta IR, Ryan AK. Claudins: unlocking the code to tight junction function during embryogenesis and in disease. Clinical Genetics. 2010;77:314-25.

[132] Sarrió D-P, Socorro MaríaHardisson, DavidCano, AmparoMoreno-Bueno, GemaPalacios, José. Epithelial-mesenchymal transition in breast cancer relates to the basal-like phenotype. Cancer Research. 2008;68:989-97.

[133] Harrell JC, Pfefferle AD, Zalles N, Prat A, Fan C, Khramtsov A, et al. Endothelial-like properties of claudin-low breast cancer cells promote tumor vascular permeability and metastasis. Clinical & Experimental Metastasis. 2013.

[134] Wu XY, Chen HX, Parker B, Rubin E, Zhu T, Lee JS, et al. HOXB7, a homeodomain protein, is overexpressed in breast cancer and confers epithelial-mesenchymal transition. Cancer Research. 2006;66:9527-34.

[135] Marshall A, Pai V, Sartor M, Horseman N. In vitro multipotent differentiation and barrier function of a human mammary epithelium. Cell and Tissue Research. 2009;335:383-95.

[136] Strobl JS, Nikkhah M, Agah M. Actions of the anti-cancer drug suberoylanilide hydroxamic acid (SAHA) on human breast cancer cytoarchitecture in silicon microstructures. Biomaterials. 2010;31:7043-50.

[137] Huang XQ, Nguyen D, Greve DW, Domach MM. Simulation of microelectrode impedance changes due to cell growth. Ieee Sensors Journal. 2004;4:576-83.

[138] Price DT, Rahman ARA, Bhansali S. Design rule for optimization of microelectrodes used in electric cell-substrate impedance sensing (ECIS). Biosensors & Bioelectronics. 2009;24:2071-6.

[139] Sommers CL, Byers SW, Thompson EW, Torri JA, Gelmann EP. Differentiation state and invasiveness of human breast cancer cell lines. Breast cancer research and treatment. 1994;31:325-35.

[140] Youlden DR, Cramb SM, Dunn NAM, Muller JM, Pyke CM, Baade PD. The descriptive epidemiology of female breast cancer: An international comparison of screening, incidence, survival and mortality. Cancer Epidemiology. 2012;36:237-48.

[141] Chin L, Andersen JN, Futreal PA. Cancer genomics: from discovery science to personalized medicine. Nature Medicine. 2011;17:297-303.

[142] Masuda H, Baggerly KA, Wang Y, Zhang Y, Gonzalez-Angulo AM, Meric-Bernstam F, et al. Differential response to neoadjuvant chemotherapy among 7 triple-negative breast cancer molecular subtypes. Clinical Cancer Research. 2013.

[143] Sarrio D, Palacios J, Hergueta-Redondo M, Gomez-Lopez G, Cano A, Moreno-Bueno G. Functional characterization of E- and P-cadherin in invasive breast cancer cells. Bmc Cancer. 2009;9:14.

[144] Di Cello F, Cope L, Li HL, Jeschke J, Wang W, Baylin SB, et al. Methylation of the Claudin 1 Promoter Is Associated with Loss of Expression in Estrogen Receptor Positive Breast Cancer. Plos One. 2013;8:8.

[145] Fogg VC, Liu CJ, Margolis B. Multiple regions of Crumbs3 are required for tight junction formation in MCF10A cells. Journal of Cell Science. 2005;118:2859-69.

[146] K'Owino IO, Sadik OA. Impedance spectroscopy: A powerful tool for rapid biomolecular screening and cell culture monitoring. Electroanalysis. 2005;17:2101-13.

[147] Spiga FM, Bonyar A, Ring B, Onofri M, Vinelli A, Santha H, et al. Hybridization chain reaction performed on a metal surface as a means of signal amplification in SPR and electrochemical biosensors. Biosensors & Bioelectronics. 2014;54:102-8.

[148] Pei JH, Tian F, Thundat T. Glucose biosensor based on the microcantilever. Analytical Chemistry. 2004;76:292-7.

[149] Huang C-J, Chen Y-H, Wang C-H, Chou T-C, Lee G-B. Integrated microfluidic systems for automatic glucose sensing and insulin injection. Sensors and Actuators B-Chemical. 2007;122:461-8.

[150] Hong J, Kandasamy K, Marimuthu M, Choi CS, Kim S. Electrical cell-substrate impedance sensing as a non-invasive tool for cancer cell study. Analyst. 2011;136:237-45.

[151] Lim JY, Donahue HJ. Cell sensing and response to micro- and nanostructured surfaces produced by chemical and topographic patterning. Tissue Engineering. 2007;13:1879-91.

[152] Stevens MM, George JH. Exploring and engineering the cell surface interface. Science. 2005;310:1135-8.

[153] Biggs MJP, Richards RG, Gadegaard N, McMurray RJ, Affrossman S, Wilkinson CDW, et al. Interactions with nanoscale topography: Adhesion quantification and signal transduction in cells of osteogenic and multipotent lineage. Journal of Biomedical Materials Research Part A. 2009;91A:195-208.

[154] Christopherson GT, Song H, Mao HQ. The influence of fiber diameter of electrospun substrates on neural stem cell differentiation and proliferation. Biomaterials. 2009;30:556-64.

[155] Feng YY, Yang T, Zhang W, Jiang C, Jiao K. Enhanced sensitivity for deoxyribonucleic acid electrochemical impedance sensor: Gold nanoparticle/polyaniline nanotube membranes. Analytica Chimica Acta. 2008;616:144-51.

[156] Shen Q, You SK, Park SG, Jiang H, Guo DD, Chen BA, et al. Electrochemical Biosensing for Cancer Cells Based on TiO2/CNT Nanocomposites Modified Electrodes. Electroanalysis. 2008;20:2526-30.

[157] Chen J, Zhang W-D, Ye J-S. Nonenzymatic electrochemical glucose sensor based on MnO2/MWNTs nanocomposite. Electrochemistry Communications. 2008;10:1268-71.

[158] Decher G, Hong JD, Schmitt J. Buildup of ultrathin multilayer films by a self-assembly process. 3. Consecutively alternating adsorption of anionic and cationic polyelectrolytes on charged surfaces. Thin Solid Films. 1992;210:831-5.

[159] Liu S, Montazami R, Liu Y, Jain V, Lin MR, Zhou X, et al. Influence of the conductor network composites on the electromechanical performance of ionic polymer conductor network composite actuators. Sensors and Actuators a-Physical. 2010;157:267-75.

[160] Wang ZY, Heflin JR, Van Cott K, Stolen RH, Ramachandran S, Ghalmi S. Biosensors employing ionic self-assembled multilayers adsorbed on long-period fiber gratings. Sensors and Actuators B-Chemical. 2009;139:618-23.

[161] Heflin JR, Figura C, Marciu D, Liu Y, Claus RO. Thickness dependence of second-harmonic generation in thin films fabricated from ionically self-assembled monolayers. Applied Physics Letters. 1999;74:495-7.

[162] DeLongchamp DM, Hammond PT. Multiple-color electrochromism from layer-by-layer-assembled polyaniline/Prussian Blue nanocomposite thin films. Chemistry of Materials. 2004;16:4799-805.

[163] Wang D, Shakeel H, Lovette J, Rice GW, Heflin JR, Agah M. Highly Stable Surface Functionalization of Microgas Chromatography Columns Using Layer-By-Layer Self-Assembly of Silica Nanoparticles. *Analytical Chemistry*. 2013;85:8135-41.

[164] Trono JD, Mizuno K, Yusa N, Matsukawa T, Yokoyama K, Uesaka M. Size, Concentration and Incubation Time Dependence of Gold Nanoparticle Uptake into Pancreas Cancer Cells and its Future Application to X-ray Drug Delivery System. Journal of Radiation Research. 2011;52:103-9.

[165] Lin HY, Kuo YJ, Chang SH, Ni TS. Characterization of electrospun nanofiber matrices made of collagen blends as potential skin substitutes. Biomedical Materials. 2013;8:9.

[166] Stanley Jr AW, Athanasuleas CL, Jacob SC, Sims SW, Tsoglin AN. Multi-channel electrical bioimpedance: a new noninvasive method to simultaneously measure cardiac and peripheral blood flow. Journal of clinical monitoring and computing. 2007;21:345-51.

[167] Spinale FG, Reines HD, Crawford FA. Comparison of bioimpedance and thermodilution methods for determining cardiac output: Experimental and clinical studies. Annals of Thoracic Surgery. 1988;45:421-5.

[168] Matthie JR. Bioimpedance measurements of human body composition: critical analysis and outlook. Expert Review of Medical Devices. 2008;5:239-61.

[169] Salmi JA. Body composition assessment with segmental multifrequency bioimpedance method. J Sports Sci Med. 2003;2:1-29.

[170] Ohmine Y, Morimoto T, Kinouchi Y, Iritani T, Takeuchi M, Monden Y. Noninvasive measurement of the electrical bioimpedance of breast tumors. Anticancer Research. 2000;20:1941-6.

[171] Ehret R, Baumann W, Brischwein M, Schwinde A, Stegbauer K, Wolf B. Monitoring of cellular behaviour by impedance measurements on interdigitated electrode structures. Biosensors & Bioelectronics. 1997;12:29-41.

[172] Escudero-Esparza A, Jiang WG, Martin TA. Claudin-5 is involved in breast cancer cell motility through the N-WASP and ROCK signalling pathways. Journal of Experimental & Clinical Cancer Research. 2012;31:18.

[173] Alexander FA, Celestin M, Price DT, Nanjundan M, Bhansali S. Design and validation of a multi-electrode bioimpedance system for enhancing spatial resolution of cellular impedance studies. Analyst. 2013;138:3728-34.

[174] Seriburi P, McGuire S, Shastry A, Bohringer KF, Meldruim DR. Measurement of the cell-substrate separation and the projected area of an individual adherent cell using electric cell-substrate impedance sensing. Analytical Chemistry. 2008;80:3677-83.

[175] Keese CR, Giaever I. A biosensor that monitors cell morphology with electrical fields. Ieee Engineering in Medicine and Biology Magazine. 1994;13:402-8.

[176] Agilent Impedance Measurement Handbook 4th ed. USA: Agilent Technologies, Inc.; 2013.

[177] Wicha MS, Liu SL, Dontu G. Cancer stem cells: An old idea - A paradigm shift. Cancer Research. 2006;66:1883-90.

[178] Gough AH, Chen N, Shun TY, Lezon TR, Boltz RC, Reese CE, et al. Identifying and Quantifying Heterogeneity in High Content Analysis: Application of Heterogeneity Indices to Drug Discovery. PloS one. 2014;9:e102678.

[179] Meacham CE, Morrison SJ. Tumour heterogeneity and cancer cell plasticity. Nature. 2013;501:328-37.

[180] Weaver WM, Tseng P, Kunze A, Masaeli M, Chung AJ, Dudani JS, et al. Advances in high-throughput single-cell microtechnologies. Current opinion in biotechnology. 2014;25:114-23.

[181] Han L, Zi X, Garmire LX, Wu Y, Weissman SM, Pan X, et al. Co-detection and sequencing of genes and transcripts from the same single cells facilitated by a microfluidics platform. Scientific reports. 2014;4.

[182] Gossett DR, Henry T, Lee SA, Ying Y, Lindgren AG, Yang OO, et al. Hydrodynamic stretching of single cells for large population mechanical phenotyping. Proceedings of the National Academy of Sciences. 2012;109:7630-5.

[183] Yang T, Rycaj K, Liu Z-M, Tang DG. Cancer stem cells: constantly evolving and functionally heterogeneous therapeutic targets. Cancer research. 2014;74:2922-7.

[184] Martelotto LG, Ng C, Piscuoglio S, Weigelt B, Reis-Filho JS. Breast cancer intra-tumor heterogeneity. Breast Cancer Res. 2014;16:210.

[185] Gottlieb B, Beitel LK, Trifiro M. Changing genetic paradigms: creating next-generation genetic databases as tools to understand the emerging complexities of genotype/phenotype relationships. Hum Genomics. 2014;8.

[186] Huang S. Non-genetic heterogeneity of cells in development: more than just noise. Development. 2009;136:3853-62.

[187] Suresh S. Biomechanics and biophysics of cancer cells. Acta Biomater. 2007;3:413-38.

[188] Mierke CT. The fundamental role of mechanical properties in the progression of cancer disease and inflammation. Reports on Progress in Physics. 2014;77:076602.

[189] Weder G, Hendriks-Balk MC, Smajda R, Rimoldi D, Liley M, Heinzelmann H, et al. Increased plasticity of the stiffness of melanoma cells correlates with their acquisition of metastatic properties. Nanomedicine: Nanotechnology, Biology and Medicine. 2014;10:141-8.

[190] Ketene AN, Schmelz EM, Roberts PC, Agah M. The effects of cancer progression on the viscoelasticity of ovarian cell cytoskeleton structures. Nanomed: Nanotechnology, Biol and Med. 2012;8:93-102.

[191] Wirtz D, Konstantopoulos K, Searson PC. The physics of cancer: the role of physical interactions and mechanical forces in metastasis. Nature Reviews Cancer. 2011;11:512-22.

[192] Babahosseini H, Ketene AN, Schmelz EM, Roberts PC, Agah M. Biomechanical profile of cancer stem-like/tumor-initiating cells derived from a progressive ovarian cancer model. Nanomedicine: Nanotechnology, Biology and Medicine. 2014.

[193] Tan AS, Baty JW, Berridge MV. The role of mitochondrial electron transport in tumorigenesis and metastasis. Biochimica et Biophysica Acta (BBA)-General Subjects. 2014;1840:1454-63.

[194] Häuselmann I, Borsig L. Altered tumor-cell glycosylation promotes metastasis. Frontiers in oncology. 2014;4.

[195] Tung JC, Barnes JM, Desai SR, Sistrunk C, Conklin M, Schedin P, et al. Tumor mechanics and metabolic dysfunction. Free Radical Biology and Medicine. 2014.

[196] Gascoyne PR, Shim S, Noshari J, Becker FF, Stemke-Hale K. Correlations between the dielectric properties and exterior morphology of cells revealed by dielectrophoretic field-flow fractionation. Electrophoresis. 2013;34:1042-50.

[197] Szachowicz-Petelska B, Dobrzynska I, Sulkowski S, Figaszewski Z. Characterization of the cell membrane during cancer transformation. Journal of Environmental Biology. 2010;31:845-50.

[198] Murdoch C, Brown BH, Hearnden V, Speight PM, D'Apice K, Hegarty AM, et al. Use of electrical impedance spectroscopy to detect malignant and potentially malignant oral lesions. International journal of nanomedicine. 2014;9:4521.

[199] Byun S, Son S, Amodei D, Cermak N, Shaw J, Kang JH, et al. Characterizing deformability and surface friction of cancer cells. Proceedings of the National Academy of Sciences of the United States of America. 2013;110:7580-5.

[200] Potts SJ, Krueger JS, Landis ND, Eberhard DA, Young GD, Schmechel SC, et al. Evaluating tumor heterogeneity in immunohistochemistry-stained breast cancer tissue. Laboratory Investigation. 2012;92:1342-57.

[201] Hou HW, Li QS, Lee GYH, Kumar AP, Ong CN, Lim CT. Deformability study of breast cancer cells using microfluidics. Biomed Microdevices. 2009;11:557-64.

[202] Lekka M, Gil D, Pogoda K, Dulinska-Litewka J, Jach R, Gostek J, et al. Cancer cell detection in tissue sections using AFM. Archives of Biochemistry and Biophysics. 2012;518:151-6.

[203] Doria ML, Cotrim Z, Macedo B, Simoes C, Domingues P, Helguero L, et al. Lipidomic approach to identify patterns in phospholipid profiles and define class differences in mammary epithelial and breast cancer cells. Breast Cancer Research and Treatment. 2012;133:635-48.

[204] Betapudi V, Licate LS, Egelhoff TT. Distinct roles of nonmuscle myosin II isoforms in the regulation of MDA-MB-231 breast cancer cell spreading and migration. Cancer research. 2006;66:4725-33.

[205] Dvir L, Nissim R, Alvarez-Elizondo MB, Weihs D. Quantitative measures to reveal coordinated cytoskeleton-nucleus reorganization during in vitro invasion of cancer cells. New Journal of Physics. 2015;17:043010.

[206] Vuoriluoto K, Haugen H, Kiviluoto S, Mpindi J, Nevo J, Gjerdrum C, et al. Vimentin regulates EMT induction by Slug and oncogenic H-Ras and migration by governing Axl expression in breast cancer. Oncogene. 2011;30:1436-48.

[207] Polyak K, Haviv I, Campbell IG. Co-evolution of tumor cells and their microenvironment. Trends in Genetics. 2009;25:30-8.

[208] Vincent-Salomon A, Thiery JP. Epithelial-mesenchymal transition in breast cancer development. Breast Cancer Research. 2003;5:101-6.

[209] Peng C-W, Liu X-L, Liu X, Li Y. Co-evolution of cancer microenvironment reveals distinctive patterns of gastric cancer invasion: laboratory evidence and clinical significance. J Transl Med. 2010;8:1479-5876.

[210] Baccelli I, Schneeweiss A, Riethdorf S, Stenzinger A, Schillert A, Vogel V, et al. Identification of a population of blood circulating tumor cells from breast cancer patients that initiates metastasis in a xenograft assay. Nature Biotechnology. 2013;31:539-44.

[211] Hanahan D, Weinberg RA. Hallmarks of Cancer: The Next Generation. Cell. 2011;144:646-74.

[212] Ward K, Li W, Zimmer S, Davis T. Viscoelastic properties of transformed cells: role in tumor cell progression and metastasis formation. Biorheology. 1990;28:301-13.

[213] Ketene AN, Roberts PC, Shea AA, Schmelz EM, Agah M. Actin filaments play a primary role for structural integrity and viscoelastic response in cells. Integr Biol. 2012;4:540-9.

[214] Stehn JR, Haass NK, Bonello T, Desouza M, Kottyan G, Treutlein H, et al. A Novel Class of Anticancer Compounds Targets the Actin Cytoskeleton in Tumor Cells. Cancer Research. 2013;73:5169-82.

[215] Cífková E, Holčapek M, Lísa M, Vrána D, Gatěk J, Melichar B. Determination of lipidomic differences between human breast cancer and surrounding normal tissues using HILIC-HPLC/ESI-MS and multivariate data analysis. Analytical and bioanalytical chemistry. 2014:1-12.

[216] Yang M, Brackenbury WJ. Membrane potential and cancer progression. Frontiers in Physiology. 2013;4:10.

[217] Strobl JS, Wonderlin WF, Flynn DC. Mitogenic signal transduction in human breast cancer cells. General Pharmacology: The Vascular System. 1995;26:1643-9.

[218] Levenson AS, Jordan VC. MCF-7: the first hormone-responsive breast cancer cell line. Cancer research. 1997:3071-8.

[219] Nehra R, Riggins RB, Shajahan AN, Zwart A, Crawford AC, Clarke R. BCL2 and CASP8 regulation by NF-κB differentially affect mitochondrial function and cell fate in antiestrogen-sensitive and-resistant breast cancer cells. The FASEB Journal. 2010;24:2040-55.

[220] Brünner N, Boulay V, Fojo A, Freter CE, Lippman ME, Clarke R. Acquisition of hormone-independent growth in MCF-7 cells is accompanied by increased expression of estrogen-regulated genes but without detectable DNA amplifications. Cancer research. 1993;53:283-90.

[221] Brünner N, Boysen B, Jirus S, Skaar TC, Holst-Hansen C, Lippman J, et al. MCF7/LCC9: an antiestrogen-resistant MCF-7 variant in which acquired resistance to the steroidal antiestrogen ICI 182,780 confers an early cross-resistance to the nonsteroidal antiestrogen tamoxifen. Cancer research. 1997;57:3486-93.

[222] Konopleva M, Watt J, Contractor R, Tsao T, Harris D, Estrov Z, et al. Mechanisms of antileukemic activity of the novel Bcl-2 homology domain-3 mimetic GX15-070 (obatoclax). Cancer research. 2008;68:3413-20.

[223] Schwartz-Roberts JL, Shajahan AN, Cook KL, Wärri A, Abu-Asab M, Clarke R. GX15-070 (Obatoclax) Induces Apoptosis and Inhibits Cathepsin D-and L–Mediated Autophagosomal Lysis in Antiestrogen-Resistant Breast Cancer Cells. Molecular cancer therapeutics. 2013;12:448-59.

[224] Glander H-J, Schaller J. Binding of annexin V to plasma membranes of human spermatozoa: a rapid assay for detection of membrane changes after cryostorage. Molecular human reproduction. 1999;5:109-15.

Appendix

A1. List of Publications

Book Chapter

V. Srinivasaraghavan and M. Agah, “Impedance sensing techniques for biomedical microdevices”, Encyclopedia of Nanotechnology, Springer, 2015, In production.

Journal Articles

V. Srinivasaraghavan, J. Strobl, A. Shajahan-Haq, R. Clarke and M. Agah, "Biophysical characterization of a hormone therapy resistant breast cancer cell model," Under preparation.

H. Babahosseini, V. Srinivasaraghavan, Z. Zhao, F. Gillam, E. Childress, J. Strobl, W. Santos, C. Zhang and M. Agah, " The impact of sphingosine kinase inhibitor-loaded nanoparticles on bioelectrical and biomechanical properties of cancer cells," Under review.

V. Srinivasaraghavan, J. Strobl and M. Agah, "A high-throughput, reconfigurable electrode array for bioimpedance spectroscopy," Under revision.

V. Srinivasaraghavan, H. Babahosseini, J. Strobl and M. Agah, "Microfluidic approach to high-content single-cell analysis of biophysical heterogeneity," Under revision.

V. Srinivasaraghavan, J. Strobl and M. Agah, "Microelectrode bioimpedance analysis distinguishes basal and claudin-low subtypes of triple negative breast cancer cells," Biomedical Microdevices, vol. 17, no. 4, July 2015.

V. Srinivasaraghavan, J. Strobl, D. Wang, J. R. Heflin, and M. Agah, "A comparative study of nano-scale coatings on gold electrodes for bioimpedance studies of breast cancer cells," Biomedical Microdevices, vol. 16, no. 5, October 2014, pp. 689-696.

M. Nikkhah, J. Strobl, V. Srinivasaraghavan, and M. Agah, "Isotropically-Etched Silicon Microwell Arrays for Rapid Breast Cancer Cell Capture," IEEE Sensors Journal, vol. 13, no. 3, January 2013, pp. 1125-1132.

Conference Proceedings/Abstracts

H. Babahosseini, V. Srinivasaraghavan, C. Zhang, and M. Agah, "Nanoparticles Modulate Bio-Electromechanical Properties of Cells," 19th International Conference on Miniaturized Systems for Chemistry and Life Sciences (MicroTAS 2015), October 2015, Gyeongju-South Korea.

V. Srinivasaraghavan, H. Babahosseini, J. Strobl and M. Agah, "Content-rich biophysical measurements from single cells," 2015 Single Cell Analysis Program (SCAP) Investigators Meeting, April 2015, NIH, Bethesda, MD.

V. Srinivasaraghavan, D. Aggarwal, H. Babahosseini, D. Nakidde, J. Strobl and M. Agah, "Analyses of single-cell mechanoelectrical properties via microfluidics," IEEE Sensors 2014, November 2014, Valencia, Spain, pp. 1772 - 1775.

V. Srinivasaraghavan, J. Strobl, D. Wang, J. R. Heflin , and M. Agah, "A study of nano-scale coatings on planar gold microelectrodes for bioimpedance measurements," Biomedical Engineering Society (BMES) Annual Meeting 2014, October 2014, San Antonio, TX, USA.

T. Shake, V. Srinivasaraghavan, P. Zellner and M. Agah, "Mammary cancer cell manipulation with Embedded Passivated-electrode Insulator-based Dielectrophoresis (EπDEP)," IEEE Sensors 2013, November 2013, Baltimore, MD, pp. 750-753.

V. Srinivasaraghavan, J. Strobl and M. Agah, "Quantitative analysis of mammary cancer cell-substrate contacts using Interference Reflection Microscopy to elucidate drug modulated bioimpedance mechanisms," Biomedical Engineering Society (BMES) Annual Meeting 2013, September 2013, Seattle, WA.

V. Srinivasaraghavan, H. Babahosseini, E. M. Schmelz, P.C. Roberts and M. Agah, "Actin filaments regulate migration time of cells through a microfluidic constriction channel," Biomedical Engineering Society (BMES) Annual Meeting 2013, September 2013, Seattle, WA.

Hesam Babahosseini, Vaishnavi Srinivasaraghavan, and Masoud Agah, "Microfluidic Chip Bio-Sensor for Detection of Cancer Cells," IEEE Sensors 2012, October 2012, Taipei, Taiwan, pp. 2030-2033.

A2. MATLAB Codes

Time Course Analysis (ECIS)

```
clear
clc
n=48; % Loop Number
%preS=20*2+1; %Pre SAHA time
%postS=35*2+1; %Post SAHA time
N=8; %Number of electrodes
path='D:\Vaishnavi\Journal
Papers\Journal2_TNBC\SAHA2.75uM_ImpedanceData\MDAMB468_6_22_13\';
for k=0:1:n
   fn1(k+1)=strcat(path,{'zxm_imped'},int2str(k),{'.xls'});
   fn2(k+1)=strcat(path,{'zxm_phase'},int2str(k),{'.xls'});
   fn3(k+1)=strcat(path,{'norm_imped'},int2str(k),{'.xls'});
end
fn4=strcat(path,{'med_phase0.xls'});
r1=[0 0 110 0]; %Range for frequency data
r2=[0 1 110 N]; %Range for impedance data
p_med=dlmread(char(fn4),'\t',r2);
for i=0:1:n
   freq=dlmread(char(fn1(i+1)),'\t',r1);
   imped=dlmread(char(fn1(i+1)),'\t',r2);
   phase=dlmread(char(fn2(i+1)),'\t',r2);
   norm=dlmread(char(fn3(i+1)),'\t',r2);
   p_norm=(phase-p_med).*(p_med).^-1;
   for j=1:1:N
      [pn(i+1,j),pn_i(i+1,j)]=max(norm(:,j));
      pf(i+1,j)=freq(pn_i(i+1,j));
      pi(i+1,j)=imped(pn_i(i+1,j),j);
      pp(i+1,j)=phase(pn_i(i+1,j),j);
      pnp(i+1,j)=p_norm(pn_i(i+1,j),j);
   end
end
%Create excel file with data analysis
fn=strcat(path,{'DataAnalysis_Peak_MDAMB468_6_22_13.xls'});
xlswrite(char(fn),pf,'Peak Frequency');
xlswrite(char(fn),pp,'Peak Phase');
xlswrite(char(fn),pi,'Peak Impedance');
xlswrite(char(fn),pn,'Peak Normalized Impedance');
```

```
xlswrite(char(fn),pnp,'Peak Normalized Phase');
```

Automated Curve Fitting (ECIS)

```
clear
clc
%Automated Fitting
%NOTES
A=2.91800e-7; % Area of electrode in m^2
% Double layer capacitance Cdl_coeff and ndl %CPE exponent
% K=Correction factor for cells K=1 when no cells on electrode and K>1 for electrode with
cells.
%Spreading resistance
%Rsp_coeff = 4.2e-1; % Resistivity of cell culture medium
% Rsp= 4.2e-1/(4*(2.91800e-7/pi)^.5)=345 Ohms; %Spreding resistance of circular electrode
% K_Rsp=Correction factor due to geometry
%Parasitic capacitance Cpar and npar
%Gap resistance due to cells Rgap_coeff where Rgap = Rgap_coeff/A;
%Capacitance of cells Ccell_coeff and ncell where Ccell = Ccell_coeff*A;
N=8; %number of electrodes
celltype='MDAMB231';
DeviceNum='2';
r=[0 0 110 0]; %Range for frequency data
r1=[0 1 110 N]; %Range for impedance data
%med
fmed=dlmread('D:\Vaishnavi\Journal
Papers\Journal2_TNBC\Modeling2015\MDAMB2312med_imped0.xls','\t',r);
Zmed=dlmread('D:\Vaishnavi\Journal
Papers\Journal2_TNBC\Modeling2015\MDAMB2312med_imped0.xls','\t',r1);
%cells
fcell=dlmread('D:\Vaishnavi\Journal
Papers\Journal2_TNBC\Modeling2015\MDAMB2312_imped40.xls','\t',r);
Zcell=dlmread('D:\Vaishnavi\Journal
Papers\Journal2_TNBC\Modeling2015\MDAMB2312_imped40.xls','\t',r1);
%OutputFile
out_path='D:\Vaishnavi\Journal Papers\Journal2_TNBC\Modeling2015\Modeling_TNBC.xls';
% f=fopen(char(out_path),'a+');
%
fprintf(f,'%s\t%s\t%s\t%s\t%s\t%s\t%s\t%s\t\t%s\t%s\t%s\t%s\t\t%s\t%s\t%s\t%s\t%s\t%s\t\t%s\
t%s\t%s\n','CellType','Device Number','Electrode
```

```
Number','Qdl','ndl','Rsp','Qpar','npar','Model1','Qdl','ndl','Rsp','Model2','Qdl','ndl','Rsp','Qcell','nce
ll','RsquareMedium','RsquareCell1','RsquareCell2');
% fclose(f);
%FIT Parameters
for i=1:1:N
   Zm=Zmed(:,i);
   ftype_med=fittype('abs((((j*2*pi*fmed*Cdlcoeff*A)^-ndl+KRsp*345)^-
1+(j*Cpar*2*pi*fmed)^npar)^-1)','problem',{'A'},'independent',
{'fmed'},'dependent',{'Zm'},'coefficients',{'Cdlcoeff','ndl','KRsp','Cpar','npar'});
   foptions_med=fitoptions('Method','NonlinearLeastSquares','Algorithm','Trust-
Region','DiffMaxChange', 1e-15,'DiffMinChange',1e-
15,'MaxFunEvals',2e3,'MaxIter',2e3,'TolX',1e-15,'TolFun',1e-15,'Lower',[1e-5,0.8,0.6,1e-
12,0.8],'Upper',[1,1,1,1e-9,1],'Startpoint',[1e-3,0.8,0.76,1e-11,0.95]);
   [fobjmed gofmed]=fit(fmed,Zm,ftype_med,foptions_med,'problem',A);
   Cdl_med(i)=fobjmed.Cdlcoeff*A;
   ndl_med(i)=fobjmed.ndl;
   Rsp_med(i)=fobjmed.KRsp*345;
   Cpar(i)=fobjmed.Cpar;
   npar(i)=fobjmed.npar;
   Rsquare_med(i)=gofmed.adjrsquare;
   Zc=Zcell(:,i);
   ftype_cell1=fittype('abs((((j*2*pi*fmed*Cdlcoeff*A)^-ndl+KRsp*345)^-
1+(j*Cpar*2*pi*fmed)^npar)^-1)','problem',{'A','Cpar','npar'},'independent',
{'fmed'},'dependent',{'Zc'},'coefficients',{'Cdlcoeff','ndl','KRsp'});
   foptions_cell1=fitoptions('Method','NonlinearLeastSquares','Algorithm','Trust-
Region','DiffMaxChange', 1e-15,'DiffMinChange',1e-
15,'MaxFunEvals',2e3,'MaxIter',2e3,'TolX',1e-15,'TolFun',1e-15,'Lower',[1e-5,0,0.6],'Upper',[1e-
1,1,5],'Startpoint',[1e-3,0.8,0.76]);
   [fobjcell1 gofcell1]=fit(fcell,Zc,ftype_cell1,foptions_cell1,'problem',{A,Cpar(i),npar(i)});
   Cdl_cell1(i)=fobjcell1.Cdlcoeff*A;
   ndl_cell1(i)=fobjcell1.ndl;
   Rsp_cell1(i)=fobjcell1.KRsp*345;
   Rsquare_cell1(i)=gofcell1.adjrsquare;
   ftype_cell2=fittype('abs((((i*2*pi*fmed*Cdlcoeff*A)^-ndl + (i*2*pi*fmed*Ccellcoeff*A)^-
ncell + 345*KRsp )^-1 + (i*Cpar*2*pi*fmed)^npar )^-
1)','problem',{'A','Cpar','npar'},'independent',
{'fmed'},'dependent',{'Zc'},'coefficients',{'Cdlcoeff','ndl','Ccellcoeff','ncell','KRsp'});
   foptions_cell2=fitoptions('Method','NonlinearLeastSquares','Algorithm','Trust-
Region','DiffMaxChange', 1e-15,'DiffMinChange',1e-
```

```
15,'MaxFunEvals',2e3,'MaxIter',2e3,'TolX',1e-15,'TolFun',1e-15,'Lower',[1e-5,0.8,1e-
5,0,0.6],'Upper',[1,1,1,1,5],'Startpoint',[1e-3,0.8,1e-3,0.8,0.76]);
   [fobjcell2 gofcell2]=fit(fcell,Zc,ftype_cell2,foptions_cell2,'problem',{A,Cpar(i),npar(i)});
   Cdl_cell2(i)=fobjcell2.Cdlcoeff*A;
   ndl_cell2(i)=fobjcell2.ndl;
   Ccell(i)=fobjcell2.Ccellcoeff*A;
   ncell(i)=fobjcell2.ncell;
   Rsp_cell2(i)=fobjcell2.KRsp*345;
   Rsquare_cell2(i)=gofcell2.adjrsquare;
     %Print Values in Spreadsheet
   f=fopen(char(out_path),'a+');
   fprintf(f,'%s\t%s\t',celltype,DeviceNum);

fprintf(f,'%u\t%e\t%e\t%e\t%e\t%e\t%e\t\t\t%e\t%e\t%e\t%e\t\t\t%e\t%e\t%e\t%e\t%e\t%e\t\t%e\t%e\t%e\n',[i
Cdl_med(i) ndl_med(i) Rsp_med(i) Cpar(i) npar(i) Cdl_cell1(i) ndl_cell1(i) Rsp_cell1(i)
Cdl_cell2(i) ndl_cell2(i) Rsp_cell2(i) Ccell(i) ncell(i) Rsquare_med(i) Rsquare_cell1(i)
Rsquare_cell2(i)]);
   fclose(f);
end
```

Transit Time (Image Processing - Microfluidics)

```
clear
clc
%setting up and array of filenames in order of frames
for i=0:1:2
   for j=0:1:9
      for k=0:1:9
         for l=0:1:9
            if(i*10^3+j*10^2+k*10+l>2744) %If frame number >last frame number exit loop
               break;
            else
               fn1(i*10^3+j*10^2+k*10+l+1) =  strcat({'C:\My Stuff\VT MEMS\Matlab
Programs\Microfluidics\Video1\Video1_'},int2str(i),int2str(j),int2str(k),int2str(l),{'.jpeg'});
            end
         end
      end
   end
end
rgb_img1=imread(char(fn1(1034)));
I1 = .2989*rgb_img1(:,:,1)+.5870*rgb_img1(:,:,2)+.1140*rgb_img1(:,:,3);
```

```
%rgb_img2=imread(char(fn1(1033)));
%I2 = .2989*rgb_img2(:,:,1)+.5870*rgb_img2(:,:,2)+.1140*rgb_img2(:,:,3);
%I(:,:)=imabsdiff(I2,I1);
imshow(I1,colormap(gray(256)));
[x,y]=ginput(2);
X=round(x);
Y=round(y);

%subtracting consecutive images and scanning for cells
j=1;
for i=1447:1:1469
   if(j==1)
      c_in=0;
      c_out=0;
   end
   rgb_img1=imread(char(fn1(i)));
   I1 = .2989*rgb_img1(:,:,1)+.5870*rgb_img1(:,:,2)+.1140*rgb_img1(:,:,3);
   rgb_img2=imread(char(fn1(i+1)));
   I2 = .2989*rgb_img2(:,:,1)+.5870*rgb_img2(:,:,2)+.1140*rgb_img2(:,:,3);
   I(:,:)=imabsdiff(I2,I1);
   for x=1:1:576
      for y=1:1:720
         if(I(x,y)<127)
            I(x,y)=uint8(0);
         else
            I(x,y)=uint8(255);
         end
      end
   end
   p_in=c_in;
   p_out=c_out;
   c_in=I(Y(1),X(1));
   c_out=I(Y(2),X(2));
   if(p_in==c_in&j>1)
      events_in(j)=events_in(j-1);
   elseif(j==1)
      events_in(j)=0;
   elseif(p_in<c_in|p_in>c_in)
      events_in(j)=events_in(j-1)+1;
   end
```

```
    if(p_out==c_out&j>1)
        events_out(j)=events_out(j-1);
    elseif(j==1)
        events_out(j)=0;
    elseif(p_out>c_out|p_out<c_out)
        events_out(j)=events_out(j-1)+1;
    end
    j=j+1;
end
%transit time calculation
l=1;
for k=2:1:j-1
    if (mod(events_in(k),2)==1 & mod(events_in(k-1),2)==0)
        enter=k;
    elseif(mod(events_out(k),2)==0 & mod(events_out(k-1),2)==1)
        exit=k;
        tt(l)=exit-enter+1;
        l=l+1;
    end
end
%displaying subtracted images
%for i=1:1:11
%    imshow(I(:,:,i),colormap(gray(256)));
%    pause(0.5);
%end
```

Bioimpedance Analysis (Microfluidics)

```
clear;
clc;
%Enter cell number in Line 4
j=50;
in_path='C:\Users\Vaishnavi\My Stuff\VT
MEMS\Microfluidics_Impedance\10_8_2014_8X8umChannel_150umEP\8X8umChannel_150u
mEP_MCF10A_Run4 Impedance_Oct08_2014_02-08PMDemod0.xls';
in_path1='C:\Users\Vaishnavi\My Stuff\VT
MEMS\Microfluidics_Impedance\10_8_2014_8X8umChannel_150umEP\8X8umChannel_150u
mEP_MCF10A_Run4 Impedance_Oct08_2014_02-08PMDemod1.xls';
```

```
in_path2='C:\Users\Vaishnavi\My Stuff\VT
MEMS\Microfluidics_Impedance\10_8_2014_8X8umChannel_150umEP\8X8umChannel_150u
mEP_MCF10A_Run4 Impedance_Oct08_2014_02-08PMDemod2.xls';
in_path3='C:\Users\Vaishnavi\My Stuff\VT
MEMS\Microfluidics_Impedance\10_8_2014_8X8umChannel_150umEP\8X8umChannel_150u
mEP_MCF10A_Run4 Impedance_Oct08_2014_02-08PMDemod3.xls';
in_path4='C:\Users\Vaishnavi\My Stuff\VT
MEMS\Microfluidics_Impedance\10_8_2014_8X8umChannel_150umEP\8X10umChannel_150
umEP_MCF10A_Run4 Impedance_Oct08_2014_02-08PMDemod4.xls';
in_path5='C:\Users\Vaishnavi\My Stuff\VT
MEMS\Microfluidics_Impedance\10_8_2014_8X8umChannel_150umEP\8X10umChannel_150
umEP_MCF10A_Run4 Impedance_Oct08_2014_02-08PMDemod5.xls';
out_path='C:\Users\Vaishnavi\My Stuff\VT
MEMS\Microfluidics_Impedance\10_8_2014_8X8umChannel_150umEP\DataAnalysis_MCF10
A.xls';
if(j==1)
   f=fopen(char(out_path),'a+');

fprintf(f,'%s\t%s\t%s\t%s\t%s\t%s\t%s\t%s\t%s\t%s\t%s\t%s\t%s\t%s\t%s\t%s\t%s\t%s\t%s\t%s\t%s\t%s\
t%s\n','Cell Number','T entry','T in','T middle','T exit','Z baseline@800k','Z peak@800k','Theta
baseline@800k','Theta peak@800k','Z baseline@100k','Z peak@100k','Theta
baseline@100k','Theta peak@100k','Z baseline@20k','Z peak@20k','Theta baseline@20k','Theta
peak@20k','Z baseline@10k','Z peak@10k','Theta baseline@10k','Theta peak@10k');
   fclose(f);
end
data=dlmread(in_path,'\t');
data1=dlmread(in_path1,'\t');
data2=dlmread(in_path2,'\t');
data3=dlmread(in_path3,'\t');
data4=dlmread(in_path4,'\t');
data5=dlmread(in_path5,'\t');
Z_mag=data(:,1);
Z_phase=data(:,2);
t=data(:,6);
Z_mag1=data1(:,1);
Z_phase1=data1(:,2);
t1=data1(:,6);
Z_mag2=data2(:,1);
Z_phase2=data2(:,2);
t2=data2(:,6);
```

```
Z_mag3=data3(:,1);
Z_phase3=data3(:,2);
t3=data3(:,6);
Z_mag4=data4(:,1);
Z_phase4=data4(:,2);
t4=data4(:,6);
Z_mag5=data5(:,1);
Z_phase5=data5(:,2);
t5=data5(:,6);
figure(1);
plot(t,Z_mag);
disp('Please select lower left and upper right corners of boxes (in that order)');
disp('for all cells you wish to analyze and then press enter');
[x,y]=ginput;
for i=1:2:numel(x)
   clc;
   if(i>1)
      clear X;
      clear Y;
   end
   figure(2);
   h1=subplot(2,6,1);
   plot(t,Z_mag);
   set(h1,'XLim',[x(i) x(i+1)]);
   h2=subplot(2,6,7);
   plot(t,Z_phase);
   set(h2,'XLim',[x(i) x(i+1)]);
   h3=subplot(2,6,2);
   plot(t1,Z_mag1);
   set(h3,'XLim',[x(i) x(i+1)]);
   h4=subplot(2,6,8);
   plot(t1,Z_phase1);
   set(h4,'XLim',[x(i) x(i+1)]);
   h5=subplot(2,6,3);
   plot(t2,Z_mag2);
   set(h5,'XLim',[x(i) x(i+1)]);
   h6=subplot(2,6,9);
   plot(t2,Z_phase2);
   set(h6,'XLim',[x(i) x(i+1)]);
   h7=subplot(2,6,4);
```

```
    plot(t3,Z_mag3);
    set(h7,'XLim',[x(i) x(i+1)]);
    h8=subplot(2,6,10);
    plot(t3,Z_phase3);
    set(h8,'XLim',[x(i) x(i+1)]);
    h9=subplot(2,6,5);
    plot(t4,Z_mag4);
    set(h9,'XLim',[x(i) x(i+1)]);
    h10=subplot(2,6,11);
    plot(t4,Z_phase4);
    set(h10,'XLim',[x(i) x(i+1)]);
    h11=subplot(2,6,6);
    plot(t5,Z_mag5);
    set(h11,'XLim',[x(i) x(i+1)]);
    h12=subplot(2,6,12);
    plot(t5,Z_phase5);
    set(h12,'XLim',[x(i) x(i+1)]);
    clc;
    disp('Please select 5 points on Figure 2 (top left) corresponding to times where');
    disp('1. Cell starts deformation to enter channel');
    disp('2. Cell completely enters channel');
    disp('3. Cell is in middle of channel');
    disp('4. Cell completely exits channel');
    disp('5. No cell');
    disp('Next select two points corresponding to baseline and peak values in all other plots');
    disp('and then press enter');
    [X,Y]=ginput;
    f=fopen(char(out_path),'a+');
    fprintf(f,'%s\t',char(strcat('Cell',int2str(j))));

fprintf(f,'%6.4f\t%6.4f\t%6.4f\t%6.4f\t%10f\t%10f\t%2.2f\t%2.2f\t%10f\t%10f\t%2.2f\t%2.2f\t
%10f\t%10f\t%2.2f\t%2.2f\t%10f\t%10f\t%2.2f\t%2.2f\n',[X(1) X(2) X(3) X(4) Y(5) Y(3) Y(6)
Y(7) Y(8) Y(9) Y(10) Y(11) Y(12) Y(13) Y(14) Y(15) Y(16) Y(17) Y(18) Y(19)]);
    fclose(f);
    j=j+1;
end
```

Automated Curve Fitting (Microfludics)

```
% clear;
```

```
% clc;
% %Read Experimental Values
% fn1='D:\Vaishnavi\Journal
Papers\Journal6_LCC\6_26_Microfluidics\DataAnalysis_LCC9GX10nM.xls';
% rD=xlsread(fn1);
%OutputFile
out_path='D:\Vaishnavi\Journal
Papers\Journal6_LCC\6_26_Microfluidics\LCC9_GX10nM_Parameters_V2.xls';
file=fopen(char(out_path),'a+');
fprintf(file,'%s\t%s\t%s\t%s\t%s\t%s\t%s\t%s\t\t%s\t%s\t%s\t%s\t%s\n','Cell
Number','Qdl','ndl','Rsp','Qpar','npar','RsquareBaseline','Rint','Qm','nm','Rcyt','RsquarePeak');
fclose(file);
%List of frequencies used
freq=[1e6; 8e5; 1e5; 7.5e4; 5e4; 2.5e4; 1e4; 1e3];
%Extract baseline and peak values of impedance
k=1;
for i=1:1:size(rD,1)
   %for j=5:4:size(rD,2)
   for j=5:4:36
      Zb_mag(i,k)=rD(i,j);
      Zp_mag(i,k)=rD(i,j+1);
      k=k+1;
   end
   k=1;
end
%for i=1:1:size(rD,1)
for i=1:1:68
   Zb=transpose(Zb_mag(i,:));
   ftype_baseline=fittype('abs((((j*Cdl*2*pi*f)^-ndl+Rsp*1e12)^-1+(j*4.185e-
14*2*pi*f)^0.845)^-1)','independent', {'f'},'dependent',{'Zb'},'coefficients',{'Cdl','ndl','Rsp'});
   foptions_baseline=fitoptions('Method','NonlinearLeastSquares','Algorithm','Trust-
Region','DiffMaxChange', 1e-15,'DiffMinChange',1e-
15,'MaxFunEvals',2e3,'MaxIter',2e3,'TolX',1e-15,'TolFun',1e-15,'Lower',[1e-14,0.6,6e-
7],'Upper',[1e-13,1,5e-6],'Startpoint',[1e-14,0.1,1e-6]);
   [fobjb gofb]=fit(freq,Zb,ftype_baseline,foptions_baseline);
   Cdl(i)=fobjb.Cdl;
   ndl(i)=fobjb.ndl;
   Rsp(i)=fobjb.Rsp*1e12;
   Cpar(i)=4.185e-14;
   npar(i)=0.845;
```

```
   Rsquareb(i)=gofb.adjrsquare;
   Zp=transpose(Zp_mag(i,:));
   ftype_peak=fittype('abs((((j*Cdl*2*pi*f)^-ndl+0.7*Rsp+((Rint*1e12)^-1+((j*2*pi*f*Cm)^-
nm+Rcyt*1e12)^-1)^-1)^-1+(j*4.185e-14*2*pi*f)^0.845)^-
1)','problem',{'Cdl','ndl','Rsp'},'independent',
{'f'},'dependent',{'Zp'},'coefficients',{'Rint','Cm','nm','Rcyt'});
   foptions_peak=fitoptions('Method','NonlinearLeastSquares','Algorithm','Trust-
Region','DiffMaxChange', 1e-15,'DiffMinChange',1e-
15,'MaxFunEvals',2e3,'MaxIter',2e3,'TolX',1e-15,'TolFun',1e-15,'Lower',[9e-8,1e-14,0.7,2e-
8],'Upper',[3e-6,1e-13,1,2e-7],'Startpoint',[1e-6,1e-14,0.1,2e-7]);
   [fobjp gofp]=fit(freq,Zp,ftype_peak,foptions_peak,'problem',{Cdl(i), ndl(i), Rsp(i)});
   Rint(i)=fobjp.Rint*1e12;
   Cm(i)=fobjp.Cm;
   nm(i)=fobjp.nm;
   Rcyt(i)=fobjp.Rcyt*1e12;
   Rsquarep(i)=gofp.adjrsquare;
   %Print Values in Spreadsheet
   file=fopen(char(out_path),'a+');
   fprintf(file,'%u\t%e\t%e\t%e\t%e\t%e\t%e\t\t%e\t%e\t%e\t%e\t%e\n',[i Cdl(i) ndl(i) Rsp(i)
Cpar(i) npar(i) Rsquareb(i) Rint(i) Cm(i) nm(i) Rcyt(i) Rsquarep(i)]);
   fclose(file);
end
%Expression for curve fitting
%Baseline   abs((((j*Cdl*2*pi*f)^-ndl+Rsp)^-1+(j*3e-14*2*pi*f)^0.855)^-1)
%Peak   abs((((j*Cdl*2*pi*f)^-ndl+0.7*Rsp+(Rint^-1+((j*2*pi*f*Cm)^-nm+Rcyt)^-1)^-1)^-
1+(j*3e-14*2*pi*f)^0.855)^-1)
```